# Local Structural Aspects and Electron-Phonon Interaction in Halide Double Perovskites

**Ph.D. THESIS**

By

**BIKASH RANJAN SAHOO**

**DEPARTMENT OF PHYSICS**

**INDIAN INSTITUTE OF TECHNOLOGY INDORE**
**OCTOBER 2024**

# Local Structural Aspects and Electron-Phonon Interaction in Halide Double Perovskites

A THESIS

*Submitted in partial fulfillment of the*

*requirements for the award of the degree*

*of*

**DOCTOR OF PHILOSOPHY**

by

**BIKASH RANJAN SAHOO**

**DEPARTMENT OF PHYSICS**

**INDIAN INSTITUTE OF TECHNOLOGY INDORE**

**OCTOBER 2024**

# INDIAN INSTITUTE OF TECHNOLOGY INDORE

## CANDIDATE'S DECLARATION

I hereby certify that the work which is presented in the thesis entitled **LOCAL STRUCTURAL ASPECTS AND ELECTRON-PHONON INTERACTION IN HALIDE DOUBLE PEROVSKITES** in the partial fulfilment of the requirements for the award of the degree of **DOCTOR OF PHILOSOPHY** and submitted in the **DEPARTMENT OF PHYSICS, Indian Institute of Technology Indore**, is an authentic record of my own work carried out during the time period from July, 2019 to October, 2024 under the supervision of Prof. Preeti A. Bhobe, Professor, Department of Physics, Indian Institute of Technology Indore.

The matter presented in this thesis has not been submitted by me for the award of any other degree of this or any other institute.

Bikash Ranjan Sahoo
12/06/2025
Signature of student with date

**Bikash Ranjan Sahoo**

- - - - - - - - - - - - - - - - - - - - - - - - - - - - - - - - - - - - - - - - - - - - - - -

This is to certify that the above statement made by the candidate is correct to the best of my/our knowledge.

12/06/2025
Signature of Thesis Supervisor with date

**Prof. Preeti A. Bhobe**

- - - - - - - - - - - - - - - - - - - - - - - - - - - - - - - - - - - - - - - - - - - - - - - -

**Bikash Ranjan Sahoo**, has successfully given his Ph.D. Oral Examination held on 12th June 2025

Signature of Thesis Supervisor

Date: 12/06/2025

- - - - - - - - - - - - - - - - - - - - - - - - - - - - - - - - - - - - - - - - - - - - - - - -

# Acknowledgements

First and foremost, I would like to express my sincere gratitude to my thesis supervisor Prof. Preeti A. Bhobe for her inspiration and encouragement throughout my Ph.D. journey. Her constant guidance, meticulous suggestions and constructive efforts towards quality research helped me to achieve and shape my academic growth. It has always been an honour and a privilege to work with her and I am deeply grateful for believing in me.

I am also grateful to my doctoral committee members, Prof. Krushna R. Mavani and Prof. Eswara Prasad Korimilli, for their insightful suggestions, comments, and time spent reviewing my work, which greatly enhanced the quality of my work.

I am grateful to Prof. Kaustubh R. Priolkar, Dr. Venkatesha R. Hathwar, Dr. Bholanath Pahari from Goa University, Dr. Uday Deshpande from UGC-DAE CSR, Indore, Prof. Rupesh Devan, Prof. Anjan Chakraborty, IIT Indore for their help and support to carry out research experiments in their labs. I would like to acknowledge Dr. Edmund Welter for assistance at P65 beamline. Financial support by the Department of Science and Technology (Government of India) provided within the framework of the India@DESY collaboration is gratefully acknowledged.

I would also like to thank HoD, all the faculty members and staffs of Department of Physics, Indian Institute of Technology Indore for their help and support. I am also thankful to the Sophisticated Instrument Center (SIC) for providing me the required experimental facilities.

I am highly obliged to my M.Sc. supervisor Prof. S. Srinath from University of Hyderabad and my M.Phil. supervisor, Dr. Dibakar Sahoo from Sambalpur University for motivated me to pursue my career in research.

A special thanks to my senior lab mates: Dr. Mithun Majee, Dr. Sayan Choudhuri, Dr. Gowthamraju S., Dr. Tamalika Samanta; my lab members: Kulbhushan, Anlin, Aarti, Astha, Prathamesh, Ramavatar for their constant support and cheerful cooperation. I wish to extend my appreciation to all my colleagues and friends, Shomina, Smrutirekha, Alok, Papuni, Biru, Nihar, Tejas, Kishor, Arpit, Bishnupriya, Pranita, Tarik, Swapnesh, Kailash, Omkar, Dushmanta, Neel, Girija, Ashwani, Anuradha, Vivek, Abhishek, Sushmita who provided both intellectual and emotional support throughout this journey. Their discussions and collaboration enriched my academic experience.

Lastly, I owe my deepest gratitude to my parents Mr. Basanta Kumar Sahoo and Mrs. Bidyutprava Sahoo, my brother Bibek Ranjan Sahoo and my family members, whose love and support made this achievement possible.

This thesis would not have been possible without the support and guidance of many individuals, to whom I am deeply grateful. Thank you all for being part of this journey.

*Dedicated to*

*...my father!!!*
***Mr. Basanta Kumar Sahoo***
*&*
*...my mother!!!*
***Mrs. Bidyutprava Sahoo***

# Abstract

Perovskites are a diverse class of materials that have captured the attention of researchers for a variety of reasons, from advancing our fundamental understanding of solid-state physics to driving innovations in materials engineering for technological applications. Over the past decade, significant progress has been made in the study of Pb-based halide perovskites and organic-inorganic hybrid perovskites, particularly due to their potential for photovoltaic applications. While these materials exhibit excellent optoelectronic properties, they also present challenges such as the environmental toxicity of lead (Pb) and the instability of organic cations under ambient conditions, limiting their practical use in devices. An alternative to these issues is the inorganic Halide Double Perovskites (HDP), which are Pb-free, offer enhanced structural stability against heat, oxygen, and moisture, and retain strong optoelectronic properties.

This thesis aims to explore the optoelectronic properties of halide double perovskites (HDPs) by establishing a comprehensive structure-property correlation, thus emphasizing the pivotal role of structural aspects in governing the photophysical behavior. All inorganic HDPs have a general chemical formula $A_2B'B''X_6$, where A comprises of monovalent cation like Cesium ($Cs^+$) or Rubidium ($Rb^+$), B' is mainly a monovalent cation such as $Ag^+$, $Na^+$ or $Cu^+$ and B" is a trivalent cation like $Bi^{3+}$, $In^{3+}$, $Sb^{3+}$ and X is the halide ion ($Cl^-$, $Br^-$ or $I^-$). The overall unit cell is ordered with alternately arranged $B'X_6$ and $B''X_6$ octahedra. The band gap of HDPs can be tuned by appropriate substitution of elements at the B' and B" sites.

First, we investigate the enhanced photoluminescence observed in mixed compositions of $Cs_2Na_xAg_{1-x}BiCl_6$, where we observe that the intensity of trap-assisted photoluminescence (PL) emission increases with increasing Na concentration. The enhanced PL is attributed to a competitive interaction between radiative and non-radiative transitions, strongly influenced by electron-phonon coupling. Next, we examine Cr-, Mn-, and

Yb-substituted $Cs_2AgBiCl_6$ and $Cs_2AgInCl_6$, focusing on their optical and electrical properties to gain insight into their charge transport mechanisms, which is a less explored aspect of these materials. Lastly, we report an intense thermochromic behavior in single-crystalline $Cs_2NaFeCl_6$ and provide the mechanism for such an exotic property. We provide in-depth analysis of the local crystal structure of $Cs_2NaFeCl_6$ through X-ray absorption spectroscopy, where we observed the octahedral distortion of Fe atoms due to charge localization and strong electron-phonon coupling leading to a change in the electronic picture of the lattice that is responsible for this exotic thermochromic behavior. For the entire study, we have employed advanced characterization techniques like X-ray diffraction, thermogravimetry analysis, electron-spin resonance spectroscopy, UV-vis diffuse reflectance spectroscopy, photoluminescence spectroscopy, electrochemical impedance spectroscopy, Raman spectroscopy, and X-ray absorption spectroscopy (XAS) to explore the structural, optical and electrical properties of the HDPs.

The findings from the present thesis highlight the significant role of strong electron-phonon interactions in influencing the optoelectronic properties of halide double perovskites. A comprehensive understanding of the structural, optical, and electrical properties of these HDPs, thus widens the prospects of utilizing these materials for applications in optoelectronic technologies.

# LIST OF PUBLICATIONS

## From peer reviewed journals:

1. "Viability of $Cs_2AgBiCl_6$: $Cr^{3+}/Yb^{3+}$ and $Cs_2AgInCl_6$: $Cr^{3+}/Yb^{3+}$ as Efficient Photoluminescent Materials and Other Photo-physical Applications,"
   **B. R. Sahoo**, R. S. Devan, P. A. Bhobe,
   *ACS Appl. Opt. Mater.*, **2 (4)**, 617-623 (2024);

2. "Unveiling Electron-Phonon Interaction That Influences the Photoluminescence Properties of $Cs_2Na_xAg_{1-x}BiCl_6$ Mixed Halide Double Perovskites,"
   **B. R. Sahoo**, P. U. Joshi, R. S. Devan, P. A. Bhobe,
   *J. Phys. Chem. C*, **128 (26)**, 10915-10920 (2024);

3. "Local Structural Distortions and Thermochromic Properties of $Cs_2NaFeCl_6$ Halide Double Perovskite,"
   **B. R. Sahoo**, V. Hathwar, U. Deshpande, P. A. Bhobe,
   *J. Mater. Chem. A*, **12 (48)**, 33699-33706 (2024) ;

4. "Electrical Properties of Transition Metal Substituted $Cs_2AgMCl_6$ (M=Bi, In),"
   **B. R. Sahoo**, B. Pahari, P. A. Bhobe,
   (Under Review);

## Presentation at conferences/meetings:

1. Oral presentation on “Influence of electron-phonon interaction on optoelectronic properties of halide double perovskite” Bikash Sahoo, P.A. Bhobe, International Conference on Smart Materials and Surfaces, 2024, (October 23-25, 2024) (organized by SECTOR, Barcelona).

2. Poster presentation on “Trap state study in Na doped $Cs_2AgBiCl_6$ halide double perovskite” Bikash Sahoo, P.A. Bhobe, International Conference on Advanced Materials, 2023, (February 21-24, 2023) (organized by Goa University).

3. Poster presentation on “Temperature dependent Raman study of Cr doped $Cs_2AgBiCl_6$”, Bikash Sahoo, P. A. Bhobe, 9th International Conference on Perspectives in Vibrational Spectroscopy 2022. (December 13-17, 2022) (organized by UGC DAE-CSR Indore).

4. Poster presentation on “Temperature dependence Raman spectra of Halide perovskites: $Cs_2AgBiCl_6$ and $Cs_2AgInCl_6$” Bikash Sahoo, P. A. Bhobe, 65th DAE Solid State Physics Symposium, 2021, (December 15-19, 2021) (organized by BARC, Mumbai).

# Contents

# List of Figures

# List of Tables

# Chapter 1

# Introduction

## 1.1 General Aspects

Starting from the research in 1959 at Bell Labs, subsequent developments on photovoltaic cells have led to the emergence of various types of material designs for solar cell applications. Figure 1.1 describes the evolution of different kinds of solar cells along with their efficiencies (data taken from NREL website). First generation solar cells are the most commercially dominant semiconducting devices using single-crystalline Si (efficiency $\sim$ 27.6%), GaAs (efficiency $\sim$28.8%) and multi-junction solar cells (efficiency $\sim$43%). The second generation solar cells based on thin film technologies include the amorphous Si (efficiency $\sim$13%), CdTe (efficiency $\sim$22.1%) and CIGS (efficiency $\sim$22.6%) with a relatively larger absorption coefficient than Si [1]. However, to overcome the limitations of flexibility, large area production, and Cd toxicity, third generation solar cells have been introduced consisting of polymers, dye-sensitized solar cells (efficiency $\sim$11.9%) and quantum dot solar cells (efficiency $\sim$10%) [2], but their low efficiencies restrict the commercialization. Since the last decade, organic-inorganic hybrid perovskites have emerged as fourth generation solar cells and surprisingly the power conversion efficiency has been achieved to 22.1% [3] competing with the Si-based photovoltaic technology. From Figure 1.1, it is evident that the efficiency of perovskite solar cell is comparatively high, attracting the world-wide research community with diverse interests.

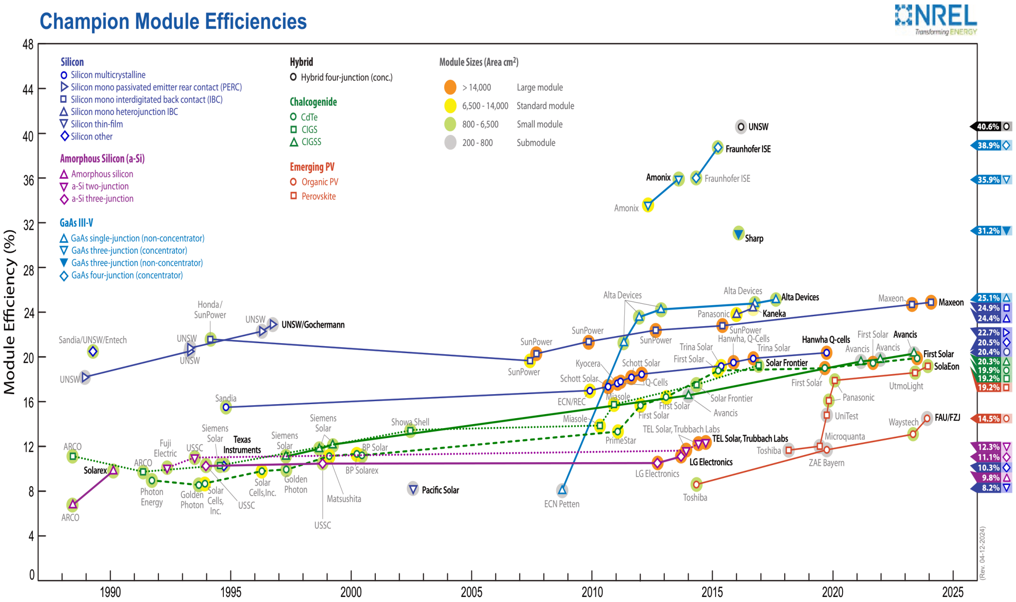

Figure 1.1: Timeline of evolution of photo-conversion efficiencies of different kinds of photovoltaic technologies (adapted from the Ref. 11 with permission).

## 1.2 Halide Perovskite

Perovskites are materials with the general chemical formula of $ABX_3$, where A and B are cations and X is the anion. Perovskites encompass a vast family of materials known for their fascinating and remarkable properties attributing to applications in various domains such as catalysis [4], ferroelectrics [5], piezoelectrics [6], spintronics [7] and optoelectronics [8]. On the basis of the X-site anion, perovskites are generally categorized into: (i) oxide perovskites with oxygen as X-site anion and (ii) halide perovskites which contain elements of the halogen group (Cl, Br, and I) as X-site anion. In this thesis, our primary focus is on the optoelectronic properties of halide perovskites.

### 1.2.1 Crystal structure of perovskite

The unit cell of a typical $ABX_3$ perovskite structure consists of $BX_6$ octahedra, where the central B-site cation is bonded with six X-site anions and the A-site cations occupy the corner position, as shown in Figure 1.2. Theoretical prediction for the formation of such a crystal structure depends upon the Goldschmidt tolerance factor (t) and octahedral factor ($\mu$) as given in the following expressions:

$$t = \frac{(R_A + R_B)}{\sqrt{2}(R_B + R_X)} \tag{1.1}$$

$$\mu = \frac{R_B}{R_X} \tag{1.2}$$

where, $R_A$, $R_B$ and $R_X$ represent the ionic radii of A-, B- and X-ions respectively. For a stable perovskite structure, the value of t should be in the range of 0.81-1.11 and the value of $\mu$ should be in between 0.41-0.90 [9]. Though both, tolerance factor and octahedral factor are necessary parameters for the prediction of perovskite structure, not all of the $ABX_3$ compositions are stable, and the stability depends on their formation energy.

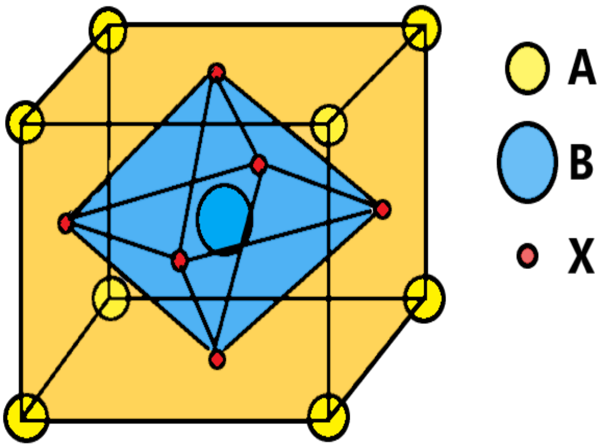

Figure 1.2: Crystal structure of a perovskite unit cell (image drawn by author).

### 1.2.2 Applications of halide perovskite

As a new class of semiconductors, lead halide perovskites have gained significant success in optoelectronic applications. Lead halide perovskites represented by the chemical formula $APbX_3$ consist of $Cs^+$, $Rb^+$, $MA^+$ (methylammonium), $FA^+$ (formamidinium) as A-site cations and $Cl^-$, $Br^-$, $I^-$ as X-site anions. A tremendous increase in photo-conversion efficiency has been achieved since the fabrication of first perovskite solar cell using $MAPbI_3$ by Miyasaka and the group in 2009 [10]. However, the efficiency of this first solar cell was quite limited ($\sim$3.8%), and only recently has the photoconversion efficiency of 25.5% been achieved surpassing the commercial polycrystalline silicon solar cell [11].

Since then, halide perovskites have evolved rapidly owing to their excellent optoelectronic properties and low cost fabrication methods. High charge carrier mobility, long carrier diffusion length [12], high absorption coefficient [13], high photoluminescence quantum yield (PLQY) [14, 15] and tunable direct band gap [16] make halide perovskite suitable for various applications such as solar cell [17], light emitting diode (LED) [18], photodetectors [19], lasers [20], thermoelectrics [21] etc.

### 1.2.3 Challenges of halide perovskite

Considering the application point of view, for any semiconducting device, optimization of stability and efficiency are two essential goals. Though improvement of the efficiency of halide perovskite based photovoltaic devices has been met with some success, stability of organic-inorganic hybrid perovskite continues to be poor hindering its large-scale practical application. Unfortunately, their chemical stability is sensitive to the exposure of light, oxygen, moisture and heat [22]. For example, the most common hybrid perovskite $MAPbI_3$ is easily decomposed to MAI and $PbI_2$ under humid condition. Also, the degradation of $MAPbI_3$ starts at 85 °C due to the volatile nature of organic cation [23]. The substitution of organic cation by inorganic cation such as Cs shows relatively higher tolerance to oxygen and heat. But, the perovskite phase of $CsPbI_3$ is easily transformed to the non-perovskite phase that is thermodynamically more stable at room temperature. Another issue regarding these halide perovskites is the phase segregation of halide ions during device operation causing the emission colour instability in LEDs [24].

Furthermore, the presence of toxic Pb in lead based perovskite is a serious concern for practical applications. Leakage of lead not only affect the environment, but has hazardous effect on human health [25]. Device encapsulation is considered to be an effective approach in such cases which can reduce the toxicity and instability issues of lead halide perovskites by isolating from oxygen and moisture. However, another straight-forward approach to tackle these challenges is to replace lead with other non-toxic elements. The isovalent cations $Sn^{2+}$ and $Ge^{2+}$ are the well deserved candidates to replace Pb due to their ability to form perovskite structures with properties comparable to lead-based counterparts, such as direct band gaps, high absorption coefficients, and tunable emissions. However, these materials suffer from instability due to the ease with which $Sn^{2+}$ and $Ge^{2+}$ oxidize to their tetravalent states ($Sn^{4+}$ and $Ge^{4+}$), causing structural degradation and diminished optoelectronic performance [26, 27]. A few attempts have been made with the substitution of heterovalent cations such as $Bi^{3+}$, $In^{3+}$, $Ti^{4+}$, $Pd^{4+}$, and so on, which are quite stable in ambient conditions. But, these substituents have indirect band gaps, poor carrier transport, and defects due to their reduced structural and electronic dimensionality [28–30].

## 1.3 Halide Double Perovskite

Considering the problems faced in halide perovskites, an effective approach is to replace two $B^{2+}$ cations with the combination of $B^{+}$ and $B^{3+}$ cations forming a 3D double perovskite. The general chemical formula of a halide double perovskite (HDP) is $A_2B'B''X_6$, where A-site cation is generally composed of monovalent cesium ($Cs^{+}$) or rubidium ($Rb^{+}$) ion, the B-site cations are mainly a mixture of monovalent ($Ag^{+}$, $Na^{+}$ or $Cu^{+}$) and trivalent ($Bi^{3+}$, $In^{3+}$ or $Sb^{3+}$) cations and the X-site is occupied by halide ions ($Cl^-$, $Br^-$ or $I^-$). The term "double perovskite" reflects the dual-cation framework that forms the interconnected octahedral network. Interestingly, this concept traces its roots back to the 19th century with the discovery of $K_2NaAlF_6$, known as "Elpasolite." The crystal structure of Elpasolite was first solved in 1932, and similar compounds with analogous structures were subsequently grouped under this name [31, 32]. Later, Elpasolites were renamed double perovskites, highlighting their structural resemblance and potential for advanced applications. This kind of stoichiometry opens up the path to discover new halide double perovskites which can contribute to the ongoing research on optoelectronic applications. Unlike the corner sharing octahedra in halide perovskite, the unit cell of a typical halide double perovskite consists of alternately arranged B'$X_6$ and B"$X_6$ octahedra leading to many engrossing properties. The A-site cation is situated in the octahedral voids as shown in Figure 1.3.

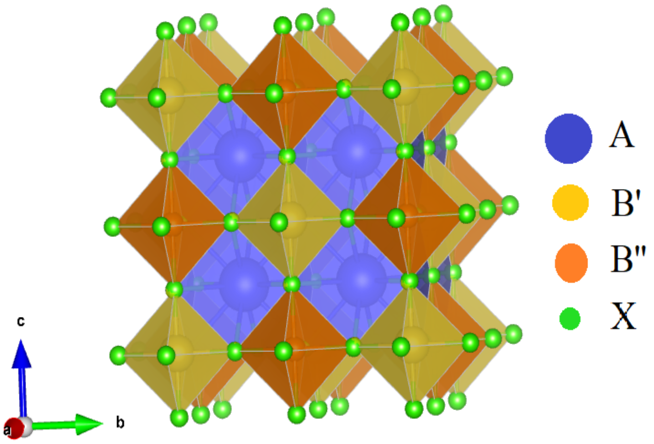

Figure 1.3: The schematic shows the structure of a typical cubic halide double perovskite compound (figure constructed using VESTA software).

Simply, by looking at the periodic table, the numbers of elements that can be occupied at A, B', B" and X-site, one can structure a halide perovskite compound and reports show that the possibility of such compounds can be counted to 9520 [33]. However, most of them are not formed practically owing to the unsuitable tolerance factor (t), or octahedral factor ($\mu$). The first reported halide double perovskite was $K_2NaAlF_6$, also known as elpasolite discovered in 1883. In 2016, some research groups reported a new halide double perovskite $Cs_2AgBiCl_6$ with exciting physical properties [34, 35]. Since then, a renewed research interest is invigorated to discover the diverse optoelectronic properties get unexplored in these compounds. The versatility of elpasolites is evident from their extensive combinatorial chemistry, with at least 350 halide perovskites synthesized to date. Even with conservative assumptions, more than 600 unexplored compounds could potentially be synthesized, offering a vast opportunity to discover new semiconductors. A possible compositional diversity based on the periodic table is given in Figure 1.4 [33]. Some of the widely studied HDPs include $Cs_2AgBiCl_6$, $Cs_2AgBiBr_6$ [34], $Cs_2AgInCl_6$ [36], $Cs_2AgSbCl_6$ [37] etc.

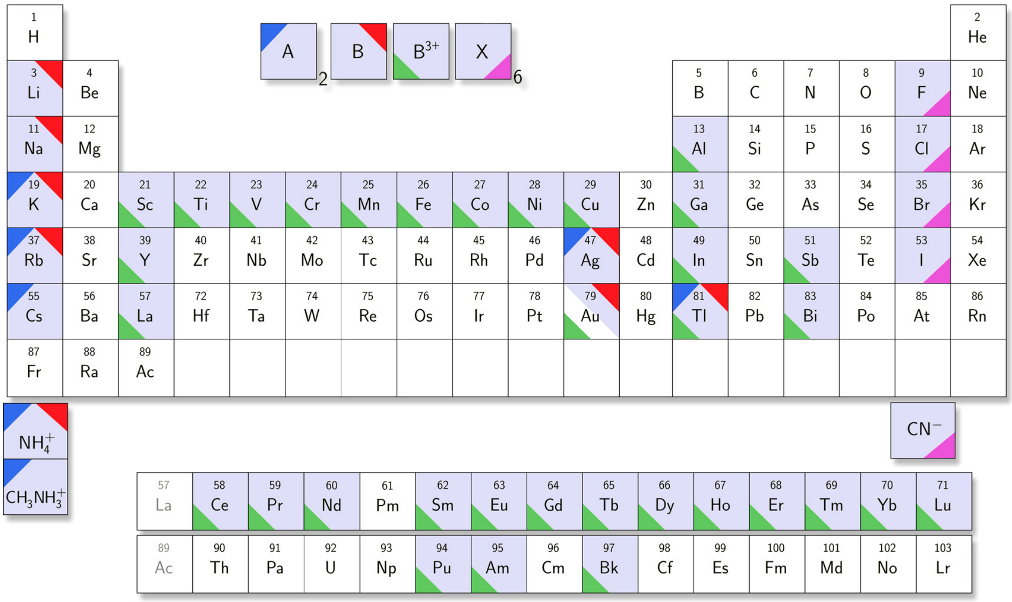

Figure 1.4: The schematic shows the possibility of elemental mapping to form halide double perovskite. The colour tag represents the site occupied by the element in $A_2BB^{3+}X_6$ (adapted from Ref. 33 with permission).

Contrasting with the hybrid perovskites, lead-free inorganic halide double perovskites show excellent stability upon exposure to moisture, light and temperature. For example, $Cs_2AgBiCl_6$ shows thermal stability up to 480 °C [38]. $Cs_2AgBiBr_6$ shows no degradation up to 500 °C [39], in contrast, hybrid perovskites easily degrade at a temperature of 100-150

°C. It is found that $Cs_2AgBiBr_6$ does not decompose even after storing under 55% humidity for 30 days or irradiating with white LED light for 1 month [35]. These excellent physical properties make HDPs as promising candidates for photovoltaic applications.

Various applications such as solar cell [40], light emitting diode (LED) [41], photodetector [42], lasers, X-ray detector [43], photocatalyst [20] etc. have already been demonstrated in HDPs as shown in Figure 1.5 [44]. Specifically, a sensitive, stable and fast UV photodetectors based on $Cs_2AgInCl_6$ single crystals with a detectivity of $10^{12}$ Jones has been reported [42]. Recently, $Cs_2AgBiBr_6$ single crystals were used to fabricate X-ray detector due to its low ionization energy and high resistivity. Moreover, $Cs_2AgBiBr_6$-based solar cells were developed with a photoconversion efficiency of 3.11% [45]. $Cs_2AgInCl_6$ has shown its potential application as light emitting diode, however, its photoluminescence quantum yield (PLQY) was extremely low (<0.1) due to the parity forbidden transition. The PLQY increased up to 86% by breaking the parity forbidden transition that takes place upon Na substitution in $Cs_2AgInCl_6$ [42]. Research has been carried out to achieve efficient NIR emission in cation doped $Cs_2AgInCl_6$. Many fluoride double perovskites have been applied as a host for $Ce^{3+}$-based laser materials [46, 47]. Recently, the photocatalytic activity (the photochemical conversion of $CO_2$ into solar fuels) of $Cs_2AgBiBr_6$ nanocrystals has been demonstrated, which holds a great potential in further photochemical applications [20].

Owing to its rich substitutional chemistry and diverse optical and electronic features, HDPs have surpassed the hybrid and lead-based perovskites. However, there are still some challenges with respect to its applicability in device fabrication. Thin films of most of the HDPs synthesized in 3D bulk form restrict their utilities in device fabrication due to anti-site disorder. Besides, the indirect band gap nature and the wide direct band gap nature of HDPs like $Cs_2AgBiCl_6$, $Cs_2AgInCl_6$, $Cs_2AgSbCl_6$, $Cs_2NaInCl_6$ etc, are not suitable for solar cell applications. These HDPs do not show any photoluminescence properties and the nature of band gap and

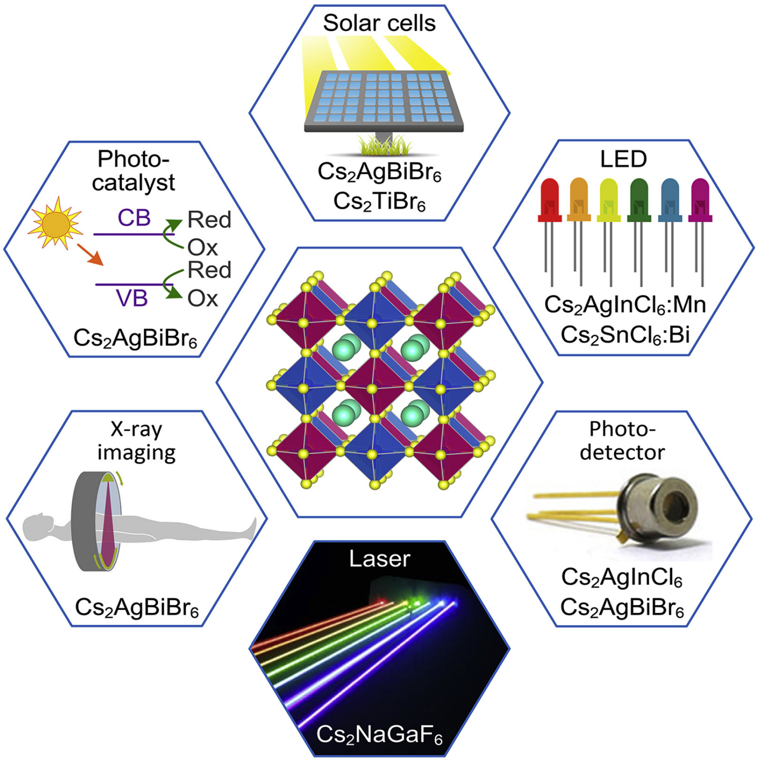

Figure 1.5: The schematic shows various applications of halide double perovskites (adapted from Ref. 44 with permission).

the bonding environment deplete the carrier mobility in these materials via parity forbidden transitions. Therefore, greater efforts need to be directed towards altering the band structure of double perovskites and/or investigating other novel double perovskite candidates for enhanced photovoltaic efficiency.

## 1.4 Band gap engineering in halide double perovskites

The physical properties of any material directly relates to its band structure, which in turn is highly influenced by the atoms present in a compound and their positions in the lattice. Halide double perovskites usually show relatively large band gap compared to the hybrid perovskites. In halide perovskites, the A-site cation typically does not have any major influence to the valence band (VB) and conduction band (CB) states. The direct impact on the electronic structure comes from the combination of $[B'X_6]^{5-}$ and $[B''X_6]^{3-}$ octahedra. One simplest and effective way to manipulate the band gap of perovskite is to change the halide ions as VBM of these materials is mainly comprised of halogen orbitals. A decreasing order of band gap is estimated for Cl, Br and I-based perovskites. However, I-based HDPs are very rare given the larger ionic radius of $I^-$ ion. Till now, the only reported I-based HDP is $Cs_2AgBiI_6$ nanocrystals synthesized by anion exchange method [48].

Several research groups have tried to fit the B'-site with Ag, Na and Cu and B"-site with Bi, In, Sb and Fe. The complex relation between band gap (electronic properties) and lattice constant (structural properties) strongly depends on the type and arrangement of atoms in the crystal lattice. In bismuth-based halide double perovskites (HDPs), the $Bi^{3+}$ ion, with its $6s^26p^0$ electronic configuration similar to $Pb^{2+}$, contributes to strong light absorption and extended carrier lifetimes. Among these materials, $Cs_2AgBiBr_6$ is considered a benchmark due to its cubic crystal structure and an optical band gap of $\sim$2 eV [49]. The absorption spectrum of $Cs_2AgBiBr_6$ has a significant peak at 438 nm attributed to $Bi^{3+}$ electronic transitions. While its photoluminescence (PL) behavior remains debated, with possible origins linked to localized states or band-to-band transitions. Despite a low PL quantum yield ($\sim$0.08%), $Cs_2AgBiBr_6$ exhibits long carrier lifetimes ($\sim$1.4 $\mu$s) and diffusion lengths ($\sim$1 $\mu$m in single crystals), indicating efficient charge transport [34, 50]. Additionally, it demonstrates remarkable environmental stability, resisting degradation under humidity, light exposure, and high temperatures. While hybrid $MA_2AgBiBr_6$ has been synthesized as an alternative with an indirect bandgap of 2.02 eV, iodine-based variants like $Cs_2AgBiI_6$ remain challenging to fabricate due to their tendency to decompose into $Cs_3Bi_2I_9$. In contrast, chlorine-based perovskites such as $Cs_2AgBiCl_6$ and $Cs_2NaBiCl_6$ exhibit larger bandgaps [51], require further modifications to enhance their photovoltaic potential.

Antimony-based halide double perovskites (HDPs), such as $Cs_2AgSbBr_6$, $Cs_2AgSbCl_6$, and $Cs_2NaSbCl_6$, have garnered interest for photovoltaic applications due to the isoelectronic nature of $Sb^{3+}$ and $Bi^{3+}$ ions. $Cs_2AgSbBr_6$, first synthesized via a hydrothermal method, crystallizes in the cubic crystal symmetry, similar to $Cs_2AgBiBr_6$. However, its synthesis often results in secondary phases, including $Cs_3Sb_2Br_9$, $Cs_2AgBr_3$, and unreacted AgBr [52]. The band structure analysis reveals that its conduction band minimum (CBM) arises from Sb 5p–Br 4p antibonding states, while the valence band maximum (VBM) is primarily influenced by Ag 4d and Br 4p orbitals. Compared to $Cs_2AgBiBr_6$, $Cs_2AgSbBr_6$ exhibits a reduced CBM energy, leading to a lower bandgap with a weak absorption edge at 1.64 eV and a sharp absorption onset at 2.49 eV [52]. Density functional theory (DFT) calculations indicate a smaller effective mass for $Cs_2AgSbBr_6$, suggesting enhanced charge carrier mobility. Solution-processed $Cs_2AgSbBr_6$ thin films, annealed at 150 °C, also contain impurity phases; however, phase-pure films were obtained with lower-temperature (135 °C) and shorter-duration (5 min) annealing, yielding an optical bandgap of 2.18 eV [53]. The carrier transport properties of these thin films remain largely unexplored.

Substituting $Br^-$ with $Cl^-$ results in a more stable $Cs_2AgSbCl_6$ phase, which retains the cubic crystal symmetry. The material exhibits an absorption onset at $\sim$2.54 eV, followed by a sharp increase at 2.79 eV, yet appears black despite its large band gap [37]. Notably, the color of $Cs_2AgSbCl_6$ powders can be tuned from yellow to near-black by varying precursor concentrations during hydrothermal synthesis. This color variation has been attributed to oxidation-induced structural modifications, specifically the conversion of $Sb^{3+}$ to $Sb^{5+}$, which is accompanied by oxygen incorporation or metal vacancy formation to maintain charge neutrality. Supporting this hypothesis, similar color transitions were observed in Sb-alloyed $Cs_2NaBiCl_6$ crystals upon the introduction of oxidizing agents such as diluted $HNO_3$ or $H_2O_2$, further suggesting that charge transfer from $Sb^{3+}$ to $Sb^{5+}$ may influence the optical absorption characteristics of these materials [54].

Indium-based halide double perovskites (HDPs), particularly

$Cs_2AgInCl_6$ and $Cs_2NaInCl_6$, have attracted significant interest due to their direct bandgap nature, a crucial feature for optoelectronic applications. However, stable iodide-based counterparts remain elusive due to unfavorable octahedral factors ($\mu < 0.41$) and inherent thermodynamic instability. The pioneering study on $Cs_2AgInCl_6$ revealed its cubic crystal structure, with both the conduction band minimum (CBM) and valence band maximum (VBM) positioned at the $\Gamma$ point, confirming its direct bandgap character. The CBM is primarily composed of delocalized In 5s states, while the VBM originates from Ag 4d and Cl 3p orbitals [36, 55]. However, due to parity-forbidden transitions at $\Gamma$, optical transitions become more allowed as the momentum shifts towards the L point, as evidenced by dipole transition matrix calculations. The UV–Vis spectrum of its single crystals displays a sharp absorption edge near 384 nm (3.2 eV). The weak PL spectrum is dominated by a broad peak at 595 nm, attributed to free-exciton emission [56]. Beyond optical performance, $Cs_2AgInCl_6$ demonstrates exceptional stability, maintaining its integrity under ambient humidity (55% RH) for 300 days and withstanding prolonged LED irradiation at 50 °C without degradation. Its thermal robustness extends beyond 500 °C, making it a resilient candidate for optoelectronic applications. Another promising In-based HDP, $Cs_2NaInCl_6$, features an even wider direct bandgap of 3.7 eV [56]. Interestingly, the mixed Ag/Na compositions exhibit intense and tunable photoluminescence from self-trapped excitons (STEs), making them highly attractive for phosphor and LED technologies, potentially revolutionizing next-generation luminescent materials [57].

Iron-based halide double perovskites, particularly $Cs_2AgFeCl_6$ and $Cs_2NaFeCl_6$, have recently gained attention due to their remarkable optical absorption properties. $Cs_2AgFeCl_6$, which crystallizes in the cubic crystal symmetry, exhibits a broad absorption edge near 800 nm, corresponding to an optical bandgap of approximately 1.62 eV—one of the lowest reported for Cl-based HDPs [58]. Despite its strong absorption, no detectable photoluminescence (PL) has been observed, even at low temperatures. Charge transport analysis via the space charge limited current (SCLC) model reveals trap state densities of $2.92 \times 10^{10}$ $cm^{-3}$ for electrons and $1.02 \times 10^{10}$ $cm^{-3}$ for holes, with corresponding mobilities of 15.3 $cm^2$ $V^{-1}$ $s^{-1}$ and 64.6 $cm^2$ $V^{-1}$ $s^{-1}$. Notably, the carrier diffusion length reaches approximately 311 nm [59]. Additionally, $Cs_2AgFeCl_6$ demonstrates excellent environmental stability, maintaining structural integrity after 63 days in humid air (RH = 50%) and 72 hours under light exposure (RH = 30%, LED intensity of 100 mW $cm^{-2}$). Similarly, $Cs_2NaFeCl_6$ single crystals have been synthesized, exhibiting a larger bandgap of around 2.1 eV. Its absorption spectrum features a sharp edge near 600 nm along with a weak broadband absorption at 750 nm, which is attributed to trapped exciton formation. Like $Cs_2AgFeCl_6$, this compound also lacks detectable PL. The estimated trap state densities are $8.35 \times 10^{10}$ $cm^{-3}$ for electrons and $1.77 \times 10^{10}$ $cm^{-3}$ for holes. However, charge transport in $Cs_2NaFeCl_6$ is notably lower, with electron and hole mobilities of 1.06 $cm^2$ $V^{-1}$ $s^{-1}$ and 2.11 $cm^2$ $V^{-1}$ $s^{-1}$, respectively. Furthermore, its carrier diffusion length is significantly shorter, measuring only around 3.7 nm. [59]

In contradiction to the single perovskite, the B-site symmetry breaking can also change the band-edge optical transition in HDPs. Further, the choice to accommodate the B' and B"-sites largely depends on the tolerance factor, octahedral factor and its formation energy. Along with the compositional mapping, external parameters like temperature and pressure significantly affects the band gap of a material. In this regard, grasping the structure-property correlation is vital for developing and engineering materials with tailored electronic and optical properties.

## 1.5 Objective of the thesis

The aim of this thesis is to understand the optoelectronic properties of HDPs that are influenced by its structural aspects. As stated earlier, the band gap of these compounds can be tuned by suitable substitution of elements at B' and B" sites. With the aim to understand the intriguing fundamental photophysical properties, we have synthesized the following compounds for the present study:

- $Cs_2Na_xAg_{1-x}BiCl_6$ (0<x<1)

  Motivation: Lead-free inorganic halide double perovskites typically suffer from low photoluminescence efficiency, limiting their performance in light-emitting and photovoltaic applications. The indirect band gap nature of such double perovskites, which leads to inefficient recombination through self-trapped excitons, further restricts their optoelectronic potential. Hence, substitution at specific atomic sites (e.g., Ag or Bi) in $Cs_2AgBiCl_6$ is crucial to tune its lattice parameters and optical band gap, potentially improving its performance. The indirect recombination mechanism through the trap states is a bottleneck that needs further study to unlock the enhanced photoluminescent behaviour. With this, we begin with our investigation into understanding the reason for the enhanced photoluminescence observed in the mixed $Cs_2Na_xAg_{1-x}BiCl_6$ compositions. A comprehensive study using UV-vis absorption, Raman spectroscopy, and time-resolved photoluminescence will help uncover the influence of substitution on the electron-phonon coupling and the dynamics of self-trapped excitons.

- $Cs_2AgBi_{0.9}M_{0.1}Cl_6$ and $Cs_2AgIn_{0.9}M_{0.1}Cl_6$ (M = Cr, Mn and Yb)

  Motivation: Next, we looked into the Cr, Mn and Yb substituted $Cs_2AgBiCl_6$ and $Cs_2AgInCl_6$ that show good PL properties. Here, we investigate their charge transport properties that are hitherto not well understood. This study aims to explore the impact of substitution on the structural, optical, and photophysical properties of $Cs_2AgBiCl_6$ and $Cs_2AgInCl_6$.

- $Cs_2NaFeCl_6$

  Motivation: Further, we observe intense thermochromicity in single crystalline $Cs_2NaFeCl_6$ composition. However, the detailed mechanisms governing thermochromism and the structure-property relationship in such lead-free perovskite remains poorly understood. With the motive to understand this phenomenon we have employed temperature dependent Raman, and X-ray absorption spectroscopy (XAS) to probe the local structure of these compounds.

## 1.6 Organisation of thesis

- **Chapter 1:** The first chapter provides a brief overview of the recently studied halide perovskite on the basis of its structural aspects and applications in various fields. A comparative study on the organic-inorganic hybrid perovskite and thermodynamically stable halide double perovskite is included to gain a fundamental perspective on these compounds. It also defines the broad objective and structure of this thesis work.
- **Chapter 2:** The second chapter presents a short description of various experimental techniques used to characterize the synthesized samples. The different characterization techniques employed in the present study for structural analysis include X-ray diffraction (XRD), single crystal X-ray diffraction (SCXRD), energy dispersive X-ray spectroscopy (EDX), thermogravimetry analysis (TGA), Raman spectroscopy, electron paramagnetic resonance (EPR), and X-ray absorption fine structure spectroscopy (XAFS). For optical characterization, we used UV-vis diffuse reflectance spectroscopy, photoluminescence (PL) spectroscopy and time resolved photoluminescence (TRPL) spectroscopy. Besides, dielectric and impedance analyzer and I-V measurement was carried out to study the electronic properties of the samples.
- **Chapter 3:** This chapter explains the effect of Na substitution on the optical properties of $Cs_2AgBiCl_6$ halide double perovskite. The successful incorporation of Na at Ag-site enhance the cationic ordering of the compounds. Further, we observed that the trap-assisted PL emission intensity increases with increase in Na concentration of the

mixed compositions. The origin for enhanced PL in these mixed compositions is speculated to be the competitive interaction of both radiative and non-radiative transitions, influenced by electron-phonon coupling. A quantitative analysis of Raman spectra along with the composition dependent Urbach tail states and Fano broadening reveal a better understanding of trap state stabilization via strong electron-phonon interaction.

- **Chapter 4:** In this chapter, we have explored the optoelectronic properties of $Cs_2AgBiCl_6$ and $Cs_2AgInCl_6$ introducing Cr, Mn and Yb at Bi/In sites. Here, we report the impact of d- and f- elements in HDP on its structural and optoelectronic properties. The structural changes induced by the incorporation of transition metal and rare earth metal was investigated by XRD, TGA and EPR study, whereas, a detailed optical analysis was performed by UV-vis DRS and PL spectroscopy measurement. However, a copious amount of elemental doping (10%) did not turn out to be fruitful in PL measurement due to concentration quenching effect. Further, we have analyzed the electronic properties with a thorough investigation of frequency and temperature dependent dielectric and impedance study. In the temperature dependent impedance spectra, two distinct temperature dependent regions were observed consisting positive temperature coefficient of resistance (PTCR) and negative temperature coefficient of resistance (NTCR) type behaviour for all the studied compositions. Interestingly, the transition temperature also reflected in thermally activated relaxation process. We further explored the relaxation and charge conduction mechanism by analysing the electric modulus and AC conductivity of the systems. Moreover, a giant superlinear power dependence of photo-current was observed in these in these HDPs enabling their broad application in photo-physics.
- **Chapter 5:** In this chapter, we explored the temperature dependent band gap engineering leading to reversible thermochromism in lead free HDP of $Cs_2NaFeCl_6$. The single crystal exhibits a dramatic

colour change from yellow at low temperature to brown at high temperature. To explore the reason behind such optical property, we employed a comprehensive temperature dependent XRD, Raman and XAFS study. Though no structural phase transition was seen in this direct band gap material, octahedral distortion of Fe atom due to charge localization and strong electron-phonon coupling was observed leading to change in the electronic picture of the lattice which is responsible for this exotic thermochromic behaviour.

- **Chapter 6:** The last chapter of the thesis includes the major findings of our experimental results and the possible future scope of the current research work.

# Chapter 2

# Experimental Techniques

## 2.1 Overview

The first and foremost aspect before proceeding to any characterization of a compound, is the need for a single phase sample for an unambiguous analysis of its physical properties. In this regard, using a proper sample preparation method becomes very important. The complete characterization of materials include its structural, optical and electrical properties that help in understanding the fundamental aspects of the materials under study and their uses in different application. In this chapter, we describe the methods that we employ for the synthesis of halide double perovskites and present a concise theoretical background of different experimental techniques used to characterize these compounds.

## 2.2 Synthesis method

For the synthesis of HDPs, we used a simple and cost-effective solution based synthesis method. Our aim is to synthesize four compositions as follows;

- $Cs_2Na_xAg_{1-x}BiCl_6$ (0<x<1)
- $Cs_2AgBi_{0.9}M_{0.1}Cl_6$ (M = Cr, Mn and Yb)

- $Cs_2AgIn_{0.9}M_{0.1}Cl_6$ (M = Cr, Mn and Yb)
- $Cs_2NaFeCl_6$ single crystal

For the synthesis of these compositions $Cs_2CO_3$ (Alfa Aesar, 99.99%), AgCl (Sigma-Aldrich, 99%), NaCl (Alfa Aesar, 99.999%), $Bi_2O_3$ (Alfa Aesar, 99%), $In_2O_3$ (Alfa Aesar, 99.99%), $Cr_2O_3$ (Alfa Aesar, 99.999%), $MnCl_2$ (Alfa Aesar, 99.99%), $Yb_2O_3$ (Alfa Aesar, 99.99%), HCl (Merck, 37%) were used as precursor materials, without any further purification process. The precursors were taken in proper stoichiometric ratios, weighed using high precision electronic weighing balance (make: Mettler Toledo), and were added to 25 ml of concentrated HCl in a round bottom flask maintained at 80 °C with continuous stirring. $Cs_2CO_3$ was added in the final step to trigger precipitation of the desired HDPs. After washing with ethanol and drying through a vacuum filtration process, the obtained powder was annealed at 210 °C for 10 h in order to get a homogeneous phase pure product.

The single crystal of $Cs_2NaFeCl_6$ was obtained by using a solvothermal synthesis method. Millimeter-sized single crystals were obtained by dissolving the solid precursors CsCl (1 mmol), NaCl (0.5 mmol) and $FeCl_3$ (0.5 mmol) in 10 ml concentrated HCl (37% w/v) in a beaker with continuous stirring to get a homogeneous mixture. The solution was transferred into a Teflon lined autoclave. The properly sealed autoclave was heated at 180 °C for 12 h. Red colour $Cs_2NaFeCl_6$ single crystals were formed by slowly cooling down to room temperature at a rate of 5 °C/h. The crystals were filtered and washed several times with ethanol before proceeding to further characterization.

## 2.3 Structural characterization

### 2.3.1 X-ray diffraction (XRD)

X-ray diffraction (XRD) is one of the most accessible technique for determining the crystal structure, phase identification, strain, crystallite size etc. of a material. A monochromatic X-ray is directed towards a crystalline sample and a constructive interference between the incident beam and reflected beam takes place. This inference is governed by the Bragg's law, $2d_{hkl}sin\theta = n\lambda$; where, d$_{hkl}$ is the interplanar distance, $\theta$ is the incidence angle, $\lambda$ is the wavelength of X-ray and n is the order of reflection (Figure 2.1). Practically, the XRD data obtained is in the form of integrated intensity as a function of $2\theta$.

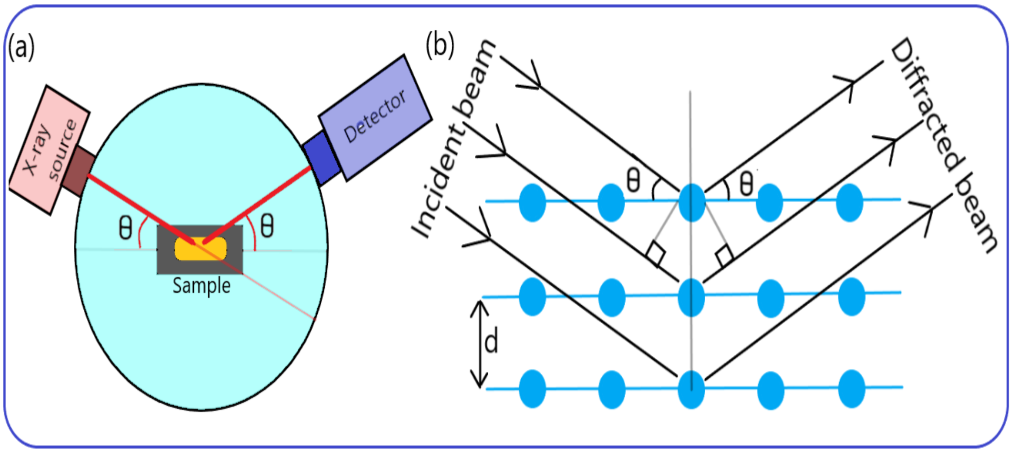

Figure 2.1: Figure shows the schematic diagram of Bragg's law for X-ray diffraction measurement (image drawn by author).

In this work, the obtained XRD patterns were further analysed using Rietveld refinement method [60], which involves a least square fit to refine the structural parameters of a sample. The best fit of the simulated pattern to the experimental pattern provides the structural information about the sample. The quality of Rietveld refinement fitting is measured in terms of $R$-factors. The weighted profile R-factor ($R_{wp}$) can be defined as,

$$R_{wp} = \sqrt{\frac{\sum_i w_i|(y_i)_{obs} - (y_i)_{cal}|^2}{\sum_i w_i|(y_i)_{obs}|^2}} \tag{2.1}$$

where, (y$_i$)$_{obs}$ and (y$_i$)$_{cal}$ represents the observed and calculated intensities at $i^{th}$ step respectively and $w_i$ is the weighting factor. Another R-factor that statistically represent the quality of fit is $R_{exp}$ and can be expressed as,

$$R_{exp} = \sqrt{\frac{(N-P)^2}{\sum_i^n w_i|(y_i)_{obs}|^2}} \tag{2.2}$$

where, N is the number of observations and P is the number of refined parameters. The ratio of $R_{wp}$ and $R_{exp}$ gives the goodness of fit ($\chi^2$), where $\chi = \frac{R_{wp}}{R_{exp}}$. The most important R-factor considered for the structural studies is the Bragg R-factor and is defined as,

$$R_{Bragg} = \frac{\sum_{hkl} |(I_{hkl})_{obs} - (I_{hkl})_{cal}|}{\sum_{hkl} |(I_{hkl})_{obs}|} \tag{2.3}$$

The smaller Bragg R-factor indicates the better fitting of the observed data. In this work, the Rietveld refinement of XRD pattern was performed by using FULLPROF SUITE software.

The synthesized samples were characterized using a PANanalytical X'PertPro X-ray diffractometer. The X-ray source was equipped with a monochromatic Cu $K_\alpha$ ($\lambda$=1.5406 Å) rotating anode source operating at 40 KV and 30 mA with a scanned $2\theta$ range from 10° to 80°. For the single crystals, the Bruker AXS D8 QUEST ECO Single crystal XRD system equipped with Mo monochromator ($\lambda$=0.71073 Å) and PHOTON 50 CMOS Detector, was employed.

### 2.3.2 Thermogravimetry analysis

Thermogravimetry analysis (TGA) is a powerful technique which can detect the structural stability and molecular degradation with temperature. By using high precision balance and carefully controlling the temperature, one can analyse the mass loss of a material as a function of temperature as shown in Figure 2.2. It has been widely used to study the thermal decomposition, moisture content or phase evolution of a compound.

To know the thermodynamic stability of the halide double perovskites in our studies, thermogravimetry analysis (TGA) was carried out using the Mettler Toledo TGA/DSC-1 instrument from room temperature to 800 °C.

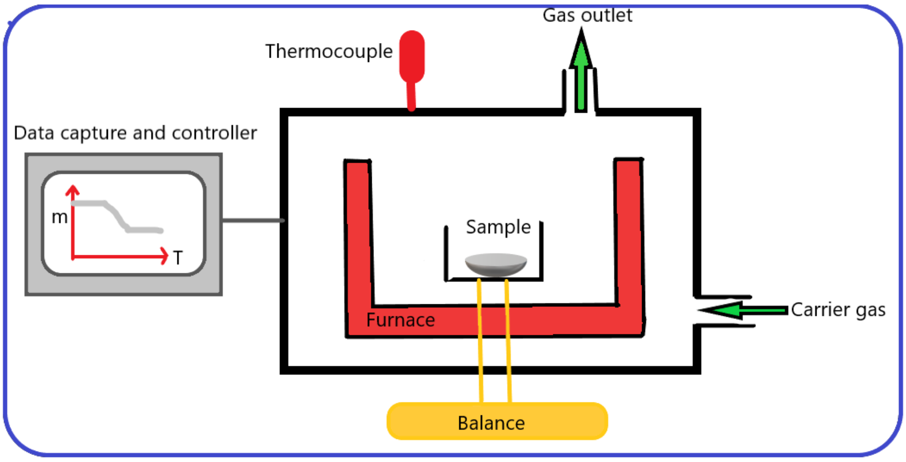

Figure 2.2: Figure depicts the working principle of thermogravimetry analysis (image drawn by author).

### 2.3.3 X-ray Absorption Fine Structure Spectroscopy (XAFS)

X-ray absorption fine structure (XAFS) spectroscopy is a unique instrumental technique to probe the local structure at atomic scale around a specific element in a unit cell. It is based on the principle of measuring the absorption coefficient ($\mu$(E)) as a function of incident X-ray energy. The experiment can be carried out in both transmission and fluorescence mode. Based on Beer-Lambert's principle, for transmission mode,

$$\mu(E)x = log(\frac{I_0}{I_T}) \tag{2.4}$$

and for fluorescence mode,

$$\mu(E)x \propto (\frac{I_F}{I_0}) \tag{2.5}$$

where, $I_T$ and $I_0$ represent the transmitted radiation and incident radiations respectively, $I_F$ is the measured intensity of the fluorescence line associated with the absorption process and $x$ is the thickness of the sample.

The basic principle of XAFS is an intrinsic quantum mechanical phenomenon, in which a notable increase in the absorption coefficient is seen as the energy of incident X-rays equals to the binding energy of a core-level electron. This is known as the threshold energy or absorption edge.

With further increase in incident energy, the atom absorbs it and emits a photoelectron to vacant state or continuum level with an energy (E-$E_0$) (where, the incident energy E is greater than the binding energy of photoelectron $E_0$) (Figure 2.3) [61]. Accordingly, the de-Broglie wavelength of the photoelectron is,

$$\lambda = \frac{h}{\sqrt{2m_e(E - E_0)}} \tag{2.6}$$

Here, $m_e$ is the mass of photoelectron and h is the Planck's constant.

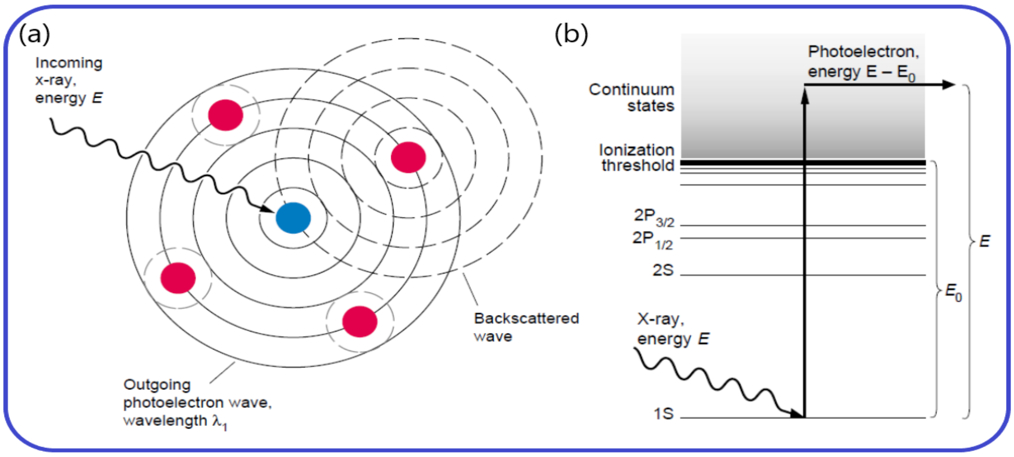

Figure 2.3: The schematics show the fundamental principle of of X-ray absorption process (adapted from Ref. 61 with permission).

The photoelectron emits spherical wave around the absorbing atom and create quantum interference between outgoing and back-scattered waveform from the nearby atoms. The modulation of this wave gives information regarding the local structure such as bond distance, co-ordination number, structural disorder, thermal vibration etc. The modulation of the absorption coefficient as a function of X-ray excitation energy is known as X-ray absorption fine structure. Generally, XAFS is further categorized into two distinct regions such that X-ray absorption near edge structure (XANES) falls within 50 eV of main absorption edge followed by the extended X-ray absorption fine structure (EXAFS) (50-1000 eV) above the absorption edge (Figure 2.4) [61].

The EXAFS fine structure can be defined as a function of energy,

$$\chi(E) = \frac{\mu(E) - \mu_0(E)}{\Delta\mu_0(E)} \tag{2.7}$$

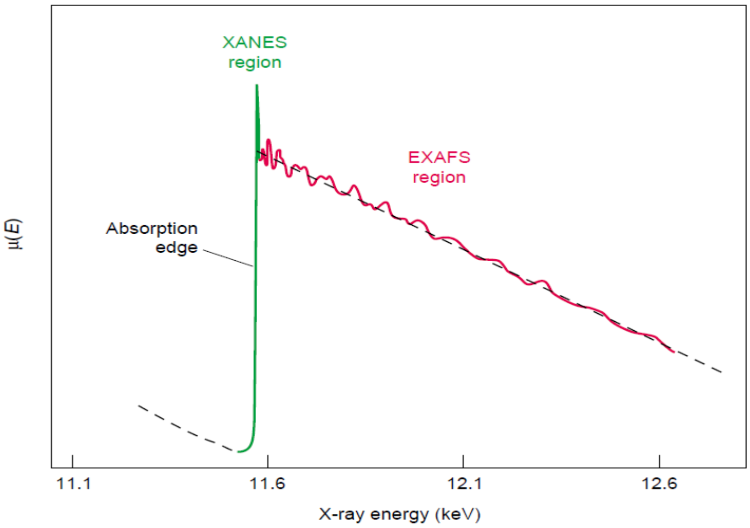

Figure 2.4: Schematic shows a typical X-ray absorption spectra having XANES and EXAFS region (adapted from Ref. 61 with permission).

where, $\mu(E)$ is the measured absorption coefficient, $\mu_0(E)$ is a smooth background function representing the absorption of an isolated atom and $\Delta\mu_0(E)$ is the jump at absorption edge, or, we can express the fine structure as a function of wave number $(k)$ as,

$$\chi(k) = \frac{\mu(k) - \mu_0(k)}{\Delta\mu_0(k)} \tag{2.8}$$

Considering all the approximation being applicable here, the above equation can be represented as,

$$\chi(k) = \sum_j \frac{N_j S_0^2 e^{-2k^2\sigma_j^2} e^{-2R_j/\lambda(k)} f_j(k)}{kR_j^2} sin[2kR_j + \delta_j(k)] \tag{2.9}$$

where, $N_j$ is co-ordination number of absorbing atom and $R_j$ is the distance to the neighbouring atom and $\sigma_j^2$ is the thermal mean square displacement, also known as Debye-Waller factor in the $j^{th}$ shell. $f_j(k)$ and $\delta_j(k)$ are the scattering parameters and $\lambda$ is the mean free path of the photoelectron. Further the Fourier transform of $\chi(k)$ into a radial structure function, $\chi(R)$ helps to visualize the major contribution of the EXAFS spectrum for the local structure.

After data collection, extraction of all the parameters in the EXAFS equation with proper analysis of the spectrum is the most crucial part for further structural studies. Preliminary data processing such as background subtraction of the pre-edge, post-edge of the $\mu(E)$ and normalization is carried out using ATHENA software. In the present work, we use ARTEMIS program which runs on the FEFF code to calculate the scattering amplitude and phase shifts through *ab-initio* self-consistence real space multiple scattering.

Using the crystallographic information file (CIF), a FEFF calculation is performed which generates all single and multiple scattering paths at a distance up to a certain cluster size. The program allows to refine the parameters like amplitude, co-ordination number, bond distance and thermal parameter to fit the experimental data, thus providing the requisite structural information.

The EXAFS spectra of Fe K-edge (7112 eV) were recorded in transmission mode at the P65 beamline, PETRA III, DESY, Hamburg. The incident and transmitted intensities were measured using gas-filled ionization chamber detectors. The spectra were recorded at 6K, 75K, 150K and 295K. The experimental data were analyzed using the Demeter software package [62].

### 2.3.4 Raman spectroscopy

Raman spectroscopy is based on the inelastic scattering of monochromatic light caused by the vibration of atomic bond known as phonons and discovered by Sir C. V. Raman in 1928. The change in molecular polarizability with the incident electromagnetic radiation produces an induced dipole moment which emits the scattered radiation elastically (Rayleigh scattering) or inelastically (Raman scattering). A decrease or increase in the inelastic energy of the scattered photons is known as Stoke's or anti-Stoke's line respectively. Raman spectrum is a plot between the intensity of scattered radiation as a function of wave number consisting different vibrational modes according to the selection rule $\Delta l = \pm 1$. Based on the group theory, each crystal symmetry shows different Raman active modes.

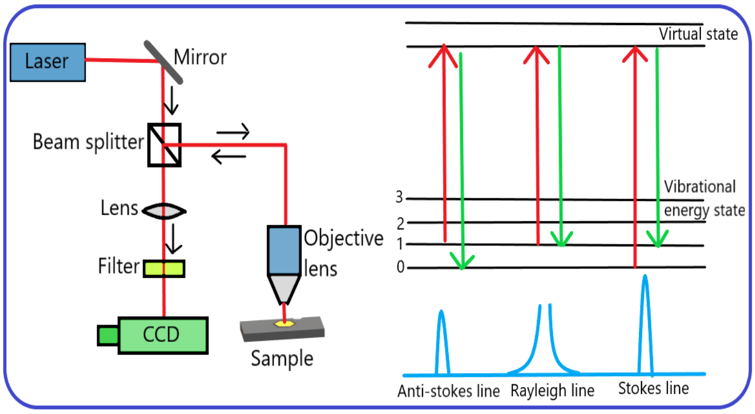

Figure 2.5: Working principle of Raman spectroscopy and the energy states related to the Raman scattering process (image drawn by author).

Raman spectra of the samples were measured within a frequency range of 20 $cm^{-1}$ to 450 $cm^{-1}$ by using the Horiba Labram HR Evolution Raman spectrometer fitted with an He-Ne laser source of wavelength 633 nm with a charge-coupled device detector in back-scattered mode. Temperature dependent spectra were recorded using the Linkam THMS600 stage controller. The laser was focused on the sample with the help of 50X magnified objective lens.

### 2.3.5 EPR spectroscopy

Electron paramagnetic resonance (EPR), also known as electron spin resonance (ESR) is a technique to detect the atoms and molecules containing unpaired electrons. It gives an insight into the identification of free radicals, structural geometry and molecular dynamics. In this process, the sample is placed inside a cavity or resonator which is kept in between the electromagnet. When a sample absorbs microwaves under the application of an appropriate microwave frequency and magnetic field, the microwaves are reflected back from the cavity, resulting in the detection of EPR signal as shown in Figure 2.6 [63]. Each electron has a magnetic moment with spin quantum number s=$\frac{1}{2}$. With the application of magnetic field B, each electron with spin magnetic moment ($m_s$=$\pm\frac{1}{2}$) has specific energy according to Zeeman effect, $E = m_s g_e \mu_B B$. Therefore, the Zeeman splitting gives an energy separation between the lower and upper state of an unpaired free electron as $\Delta E = g_e \mu_B B$, which is the basic principle of EPR spectroscopy. However, the interaction of the magnetic fields of the nuclei of the atom in a molecule can affect the unpaired electrons. This kind of coupling between the perturbed nuclei and unpaired electron is known as hyperfine interaction and introduces additional energy states as reflected in the multi-lined spectra in EPR measurement. Mathematically, the number of lines raised from the hyperfine interaction is 2nI+1, where n is the number of equivalent nuclei and I is the spin of the electron. The magnetic resonance spectra were recorded with the Bruker BioSpin EPR spectrometer. The solid sample was placed at the centre of the resonant cavity placed between the two poles of an electromagnet having the X-band resonance frequency of 9.42 GHz and the data were recorded at room temperature (300 K).

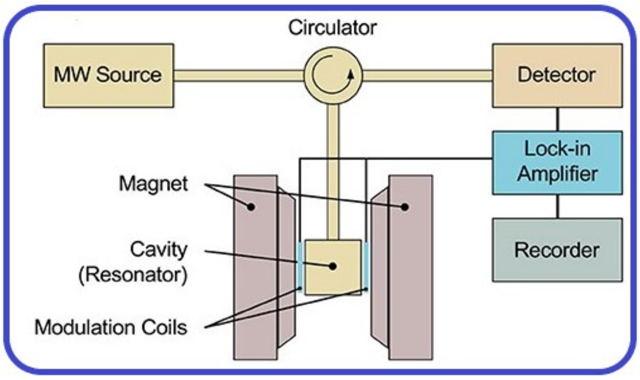

Figure 2.6: Schematic diagram of an electron paramagnetic resonance spectrometer (adapted from Ref. 63 with permission).

## 2.4 Elemental characterization: EDX Spectroscopy

Energy dispersive x-ray spectroscopy (EDX) is a commonly used technique for the identification of elemental composition of an unknown sample and is an integrated feature of field emission scanning electron microscopy (FE-

SEM) system. The working principle of EDX is based on the process where the bombardment of electron beam on the sample surface leads to the knocking off the electrons from inner shell followed by the occupation of an outer shell electron in the vacant inner shell as shown in Figure 2.7. The energy loss in this process is emitted in the form of X-rays with unique wavelength for different atoms and the intensity of the peak depends on the concentration of that element in the sample.

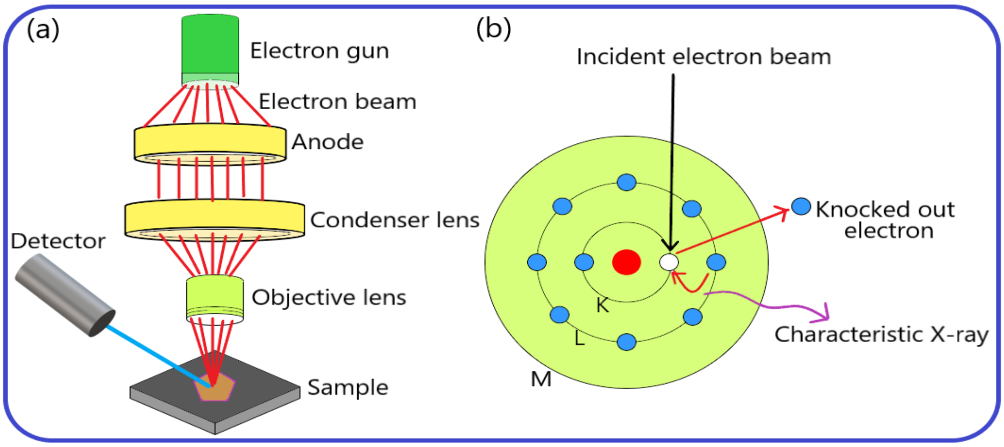

Figure 2.7: Figure depicts the working principle of Energy dispersive X-ray spectroscopy measurement (image drawn by author).

The stoichiometry of the compositions was confirmed from energy dispersive X-ray analysis (EDX) using SUPRA 55 Zeiss field emission scanning electron microscope equipped with Oxford Instruments AZtec energy dispersive microanalysis system.

## 2.5 Optical characterization

### 2.5.1 UV-visible spectroscopy

UV-visible spectroscopy is an excellent technique to obtain the optical properties of a material and can be measured in terms of absorption spectra or reflectance spectra. Generally, in reflectance mode, data is collected from the reflection of incident light energy off a solid surface, while in absorption mode, one has to measure the light intensity before and after passing through the sample. This is an excellent technique to calculate the band gap of a material using the Kubelka-Munk function, which is related to the reflectance of the material as;

$$F(R) = \frac{(1-R_\infty)^2}{2R_\infty} \tag{2.10}$$

Where, $R_\infty = R_{sample}/R_{standard}$ is the reflectance of an infinitely thick material and termed as diffuse reflectance. Again, the band gap and the absorption coefficient are related through the well-known Tauc relation;

$$\alpha h\nu = A(h\nu - E_g)^n \tag{2.11}$$

where, $\alpha$ is the linear absorption coefficient, $\nu$ is the light frequency, $E_g$ is the band gap of the material and A is the proportionality constant. The power n is equal to 1/2 for direct band gap and 2 for indirect band gap. When the incident radiation scatters in a perfectly diffuse manner, the Kubelka-Munk function is proportional to the absorption coefficient and we get the relation for a direct band gap material;

$$(F(R)h\nu)^2 = A(h\nu - E_g) \tag{2.12}$$

and, for an indirect band gap material;

$$(F(R)h\nu)^{1/2} = A(h\nu - E_g) \tag{2.13}$$

The UV-Visible diffuse reflectance spectra were measured using Shimadzu UV-3600i UV-Vis-NIR spectrometer over a spectral range of 300-800 nm calibrated with a barium sulfite sample as reference. For temperature dependence band gap study, we use Perkin Elmer Lambda 950 UV/VIS Spectrometer having a resolution of 0.05 nm equipped with HARRICK ATC automatic temperature controller.

### 2.5.2 Photoluminescence spectroscopy

Photoluminescence (PL) spectroscopy is one of the widely used technique to measure the light emission from the material after photo-excitation. When a light is absorbed by a material, the electrons get excited to a higher energy level and decay to the conduction band minimum (CBM) through internal conversion process by losing vibrational energy, which is a non-radiative process. The combination of electron and hole pair is known as exciton. The decay of exciton i.e., when the electrons return back to the ground state by releasing energy in terms of photons facilitates the emission process.

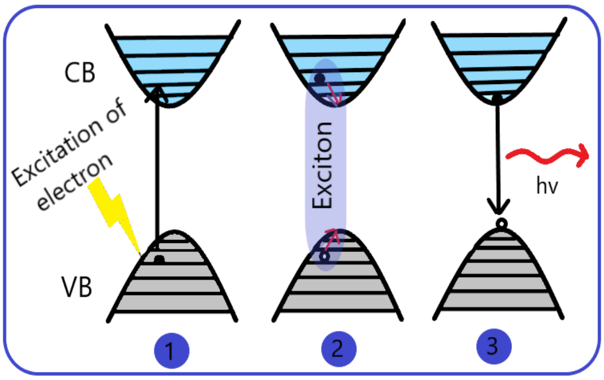

Figure 2.8: Figure depicts the fundamental principle of a photoluminescence process (image drawn by author).

Further, time-resolved photoluminescence (TRPL) spectroscopy gives an insight into both spectral as well as temporal evolution of the emission of a sample. In general, it measures the decay of electron-hole pairs (exciton) to the lower energy level. However, the decay of exciton is not a linear process, rather it involves a multi-exponential decay process. Mathematically, the decay life time can be expressed as, $I = \sum_i I_i e^{-t/\tau_i}$. According to the nature of excited state i.e., singlet or triplet state, the life time of the exciton can vary from ps to ms. Further, the decay process can be radiative (emits light) or non-radiative (does not emit light) and both of them affect the life time of the fluorophore.

Photoluminescence spectra were measured at room temperature (300 K) using the Cary Eclipse Fluorescence Spectrophotometer (Agilent Technologies) having a 2.5 nm entrance slit width and 5 nm exit slit width equipped with a solid state sample holder.

## 2.6 Electrical characterization

### 2.6.1 Electrochemical impedance spectroscopy

Electrochemical impedance spectroscopy (EIS) is a commonly used technology to measure various electrochemical properties of a compound. This technique gives the frequency response of a system including the ability to store and dissipate energy in terms of dielectric properties of the medium and impedance of the system. The data obtained in EIS can be expressed in the form of Nyquist plot which gives the information regarding the real and imaginary part of impedance. The dielectric property of a material depends on the various kinds of polarization process occurred in a certain frequency range. The dielectric polarization is a sum total of electronic, vibrational (atomic), orientational (dipolar), ionic and interfacial polarization as shown in Figure 2.9.

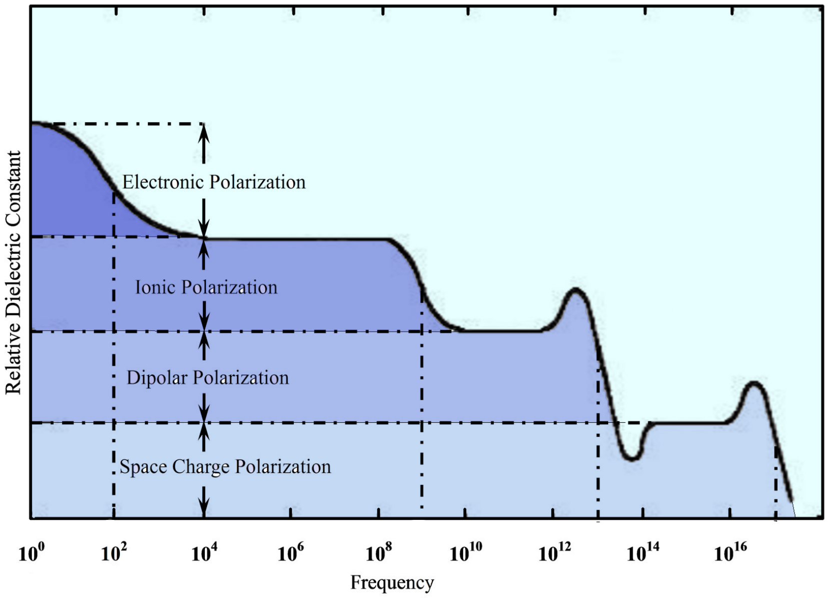

Figure 2.9: Figure depicts the frequency dependence of various polarization process involved in a dielectric material (image drawn by author).

In order to measure the dielectric properties of the materials, a device was configured by electroding the top and bottom surfaces of the pellet with silver paste. Temperature dependent dielectric and impedance measurement were carried out using an LCR spectrometer (HIKOI, MODEL:

IM 3536) from room temperature to 250 °C.

### 2.6.2 Photoconductivity

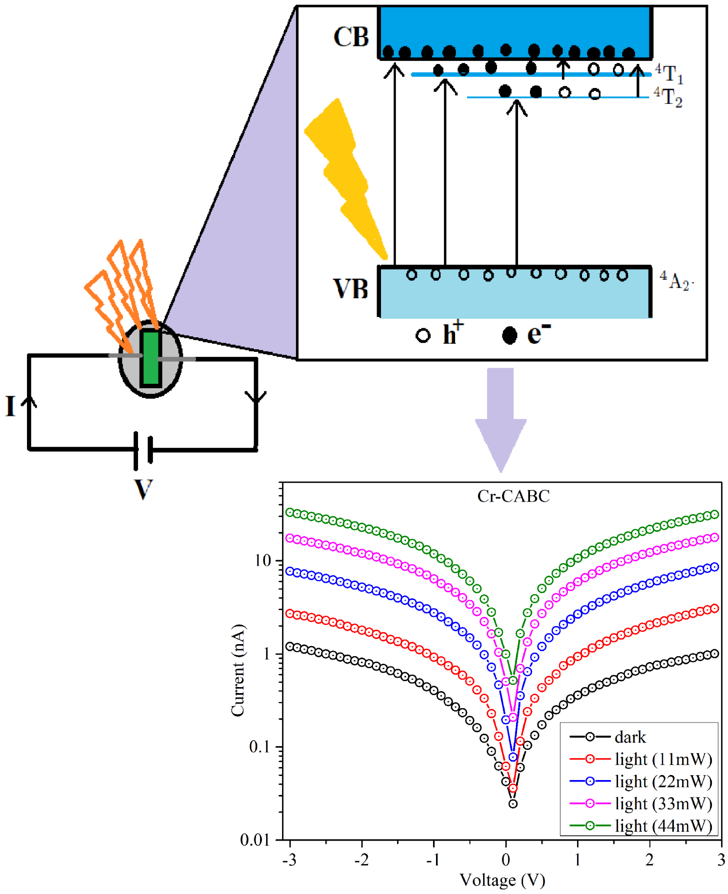

Figure 2.10: Figure depicts the fundamental principle of photoconductivity (adapted from own article Ref. 64).

Photoconductivity is a process where the absorption of incident light induces conduction of electrons. When light is absorbed by a material, the number of charge carriers increases resulting in the enhancement of conductivity as shown in Figure 2.10 [64]. It helps in various applications like phtodetector, photodiode, phototransistor and so on.

The photoresponse characterization was carried out using Keithley 6517B electrometer and a 450 nm light source.

# Chapter 3

# Study of Na substituted $Cs_2AgBiCl_6$ halide double perovskite

## 3.1 Overview

$Cs_2AgBiCl_6$ is one of the most stable halide double perovskite whose optoelectronic properties can be enhanced by incorporating various elements at Ag or Bi site. Here, the optical gap of the compound is manipulated by Na substitution at Ag site to understand the structural and optical effect of the compounds. Further, we explain the trap carrier dynamic process by probing time resolved photoluminescence (TRPL) technique in Na substituted $Cs_2AgBiCl_6$ compounds. TRPL spectroscopy is a powerful technique that has been employed to study the charge carrier recombination kinetics of photoluminescent materials. The competitive radiative and non-radiative recombination processes happening in these materials affect the TRPL decay and is therefore useful for extracting information related to these processes. However, understanding the origin and stability of trap states is essential, as the underlying mechanism of the radiative and non-radiative transitions are highly influenced by electron-phonon coupling. A comprehensive understanding of the electron-phonon coupling phenomenon in such halide double perovskites remains elusive. With the intention of understanding the photophysics via the electron-phonon coupling, we have synthesized phase pure $Cs_2Na_xAg_{1-x}BiCl_6$ ($0 \leq x \leq 1$) compounds and conducted an extensive investigation of the local crystal structure using an in-depth analysis of the UV-vis absorption and Raman spectroscopy.

## 3.2 Stability and composition

One of the advantages of inorganic double perovskites is their structural stability over a wide temperature range. The thermogravimetric measurements carried out in the temperature range of 30°C to 800°C for the present set of compositions bring out this aspect. The plots (see Figure 3.1) demonstrate no significant weight loss up to 465°C for $Cs_2AgBiCl_6$, whereas, for $Cs_2NaBiCl_6$, the stability extends to 575°C. The temperature range of stability for the mixed compositions with varying Ag/Na ratios lies between the limits set by the end members of the series. With increase in Na concentration the stability of the compound increases gradually which is a good sign from application point of view.

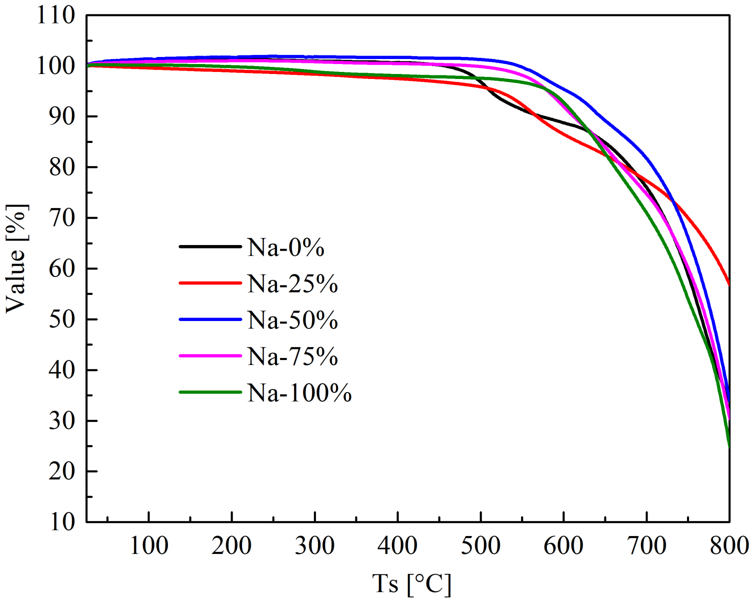

Figure 3.1: Thermogravimetry analysis spectra of Na substituted $Cs_2AgBiCl_6$ compounds.

Besides, the energy dispersive X-ray spectroscopy (EDS) employed to analyze the elemental composition of the synthesized compounds indicates that the desired proportion of Cs, Ag, Na, Bi and Cl concentration is present in the samples, matching its chemical stoichiometry and is presented in Table 3.1.

| Compound | Cs | Ag | Na | Bi | Cl |
|---|---|---|---|---|---|
| $Cs_2AgBiCl_6$ | 22.0 | 10.7 | - | 10.8 | 56.5 |
| $Cs_2Ag_{0.75}Na_{0.25}BiCl_6$ | 21.3 | 8.5 | 2.4 | 10.5 | 57.3 |
| $Cs_2Ag_{0.5}Na_{0.5}BiCl_6$ | 21.7 | 5.6 | 5.7 | 10.8 | 56.2 |
| $Cs_2Ag_{0.25}Na_{0.75}BiCl_6$ | 22.6 | 2.8 | 7.1 | 10.9 | 56.6 |
| $Cs_2NaBiCl_6$ | 23.3 | - | 10.2 | 10.3 | 56.2 |

Table 3.1: Elemental compositions (in atomic %) for each perovskite compound.

## 3.3 Structural properties

Room temperature powder X-ray diffraction (XRD) profiles of $Cs_2Na_xAg_{1-x}BiCl_6$ compositions presented in Figure 3.2 belong to a cubic structure having $Fm\bar{3}m$ space group symmetry. The absence of any unaccounted peak confirms the phase purity of all the compositions. Structural refinement of the XRD profiles using the Rietveld method [60] yields the parameters such as unit cell dimensions and atomic site occupancy. Despite the ionic radius of $Na^+$ (1.02 Å) being smaller than that of $Ag^+$ (1.15 Å), the lattice constant increases linearly with the $Na^+$ content following Vegard's law. Replacing a transition metal ion ($Ag^+$) with a highly electropositive alkali metal ion ($Na^+$) brings in a higher cationic order in the rock-salt unit cell, as reflected by the relative increase in the intensity of the (111) superlattice reflection with respect to the (220) main peak and introduces a robust ionic character to the bonds. While the long-range lattice symmetry is maintained, the diffraction peaks of the mixed Ag/Na compositions tend to be asymmetric with slightly broader peak widths, implying the manifestation of local lattice relaxation effects.

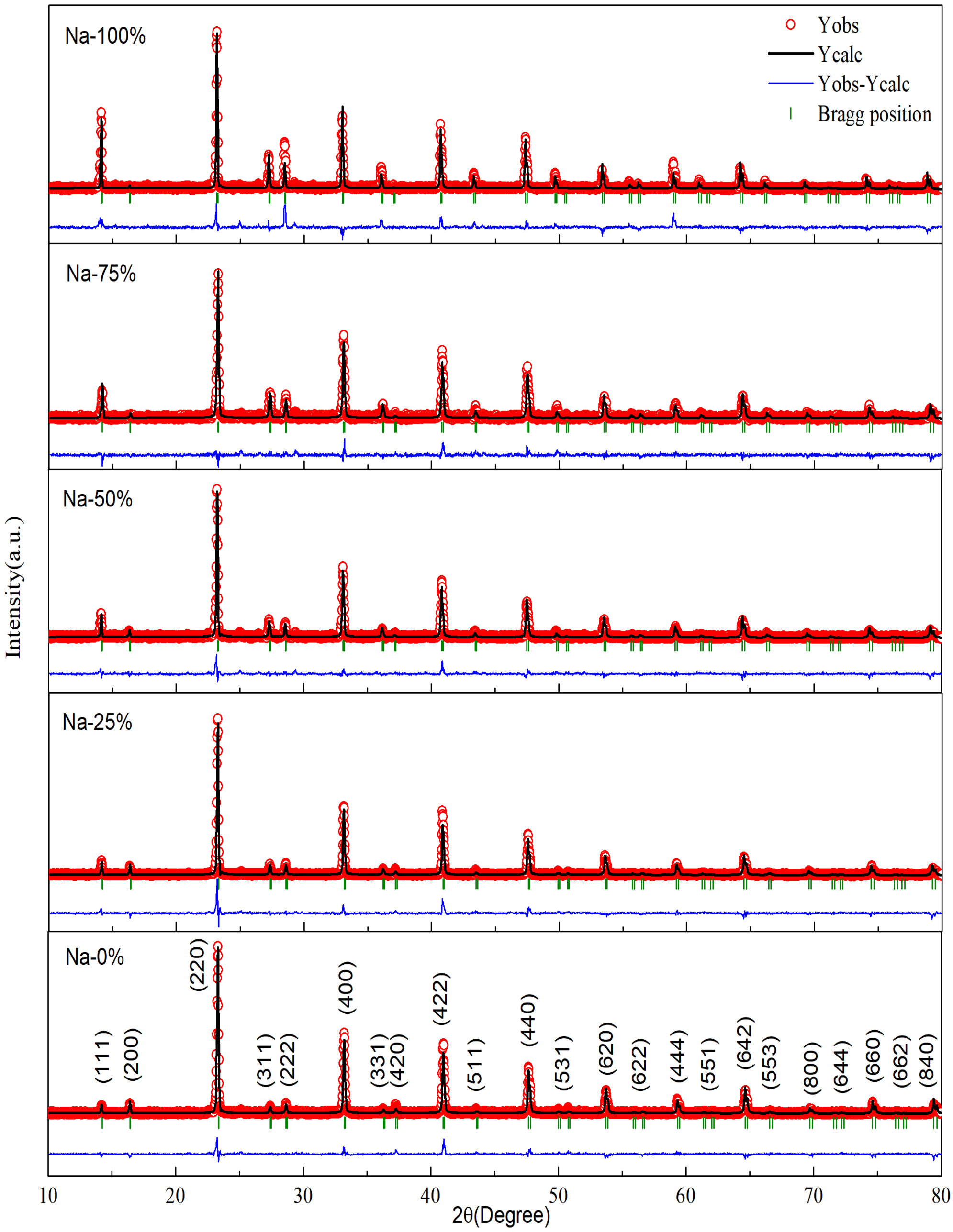

Figure 3.2: Rietveld refinement of room temperature X-ray diffraction spectra of Na substituted $Cs_2AgBiCl_6$ compounds.

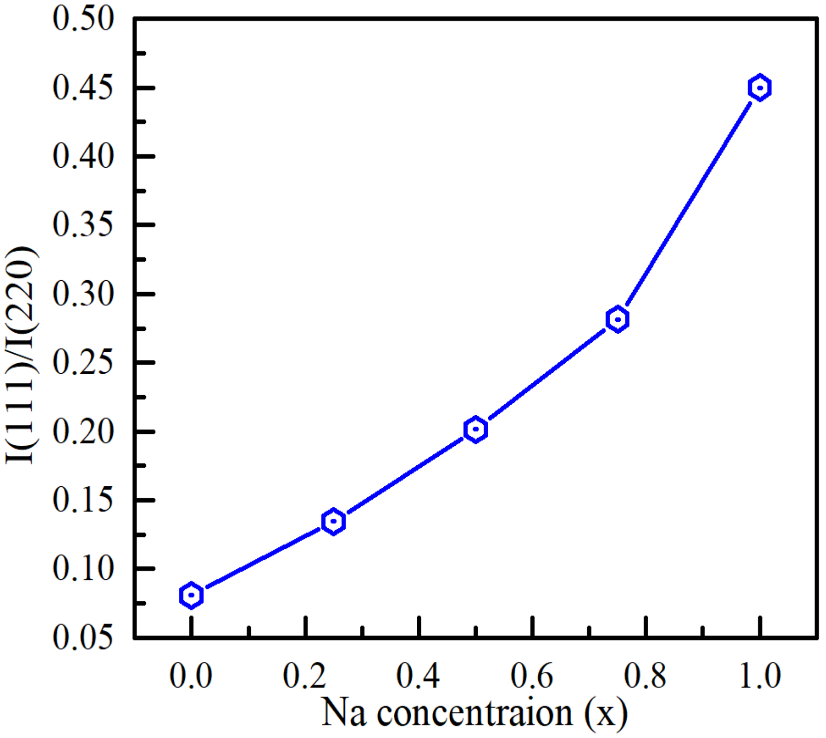

Figure 3.3: Variation of intensity ratio of I(111)/I(220) with Na content.

The dynamic stereo-active $5s^2$ lone pairs on $Bi^{3+}$ ions of $Cs_2Na_xAg_{1-x}BiCl_6$ contribute to the local lattice distortion and low-frequency vibrational modes. Raman spectroscopy is a suitable probe for investigating such local crystal symmetry distortions. Figure 3.4 presents the room temperature Raman spectra obtained for all compositions using a 633 nm laser excitation source within a frequency range of 20 cm$^{-1}$ to

| Atom | Wyckoff position | x | y | z |
|---|---|---|---|---|
| Cs | 8c | 0.25 | 0.25 | 0.25 |
| Na | 4a | 0 | 0 | 0 |
| Ag | 4a | 0 | 0 | 0 |
| Bi | 4b | 0.5 | 0.5 | 0.5 |
| Cl | 24e | 0.25116 | 0 | 0 |

Table 3.2: Refined structural parameters for $Cs_2Ag_{0.25}Na_{0.75}BiCl_6$ compound.

| Compound | Na-0% | Na-25% | Na-50% | Na-75% | Na-100% |
|---|---|---|---|---|---|
| a=b=c (Å) | 10.78(6) | 10.79(6) | 10.81(2) | 10.82(5) | 10.84(1) |
| $\alpha = \beta = \gamma$ | 90° | 90° | 90° | 90° | 90° |
| V (Å$^3$) | 1255.12(3) | 1258.41(2) | 1264.00(2) | 1268.59(2) | 1273.97(1) |
| $\chi^2$ | 17.7 | 12.1 | 6.84 | 7.42 | 9.58 |
| $R_p$ | 29.3 | 24.4 | 20.2 | 20.2 | 21.3 |
| $R_{wp}$ | 31.2 | 25.2 | 20.8 | 20.9 | 22.9 |
| $R_{exp}$ | 7.43 | 7.31 | 7.96 | 7.67 | 7.41 |

Table 3.3: Table shows the lattice parameter, cell volume and Rietveld refinement fitting parameters for all 5 compositions.

400 cm$^{-1}$. The vibrational properties of $Cs_2Na_xAg_{1-x}BiCl_6$ attune to its $Fm\bar{3}m$ symmetry, exhibits four distinct Raman active modes, at ~46 cm$^{-1}$ ($T^1_{2g}$), ~114 cm$^{-1}$ ($T^2_{2g}$), ~215 cm$^{-1}$ ($E_g$) and ~283 cm$^{-1}$ ($A_{1g}$). These Raman modes are also consistent with the other reported results [67].

The local environment of the constituted atoms can be well analysed from the vibrational spectra of different bonds. The weak mode at 46 cm$^{-1}$ that results from the translational motion of Cs atoms gain in strength upon Na-substitution, a direct consequence of the growing ionic character of the bonds. The $E_g$ mode associated with the asymmetric stretching of [Bi-$Cl_6$] octahedra shifts towards higher frequency with simultaneous suppression of its intensity, which is a direct consequence of increased unit cell volume with increasing Na content. Signatures of local lattice distortion come from the $T^2_{2g}$ mode, associated with the breathing vibration of Ag/Na-Cl bond and the $A_{1g}$ mode, associated with the symmetric stretching of both Bi-$Cl_6$ and [(Ag/Na)-$Cl_6$] octahedral cages. Both these modes are asymmetric in the direction of increasing wave number for pure $Cs_2AgBiCl_6$ composition. As Na systematically replaces the Ag atoms, a sharp increase in peak intensity is observed along with a concomitant decrease in the peak width.

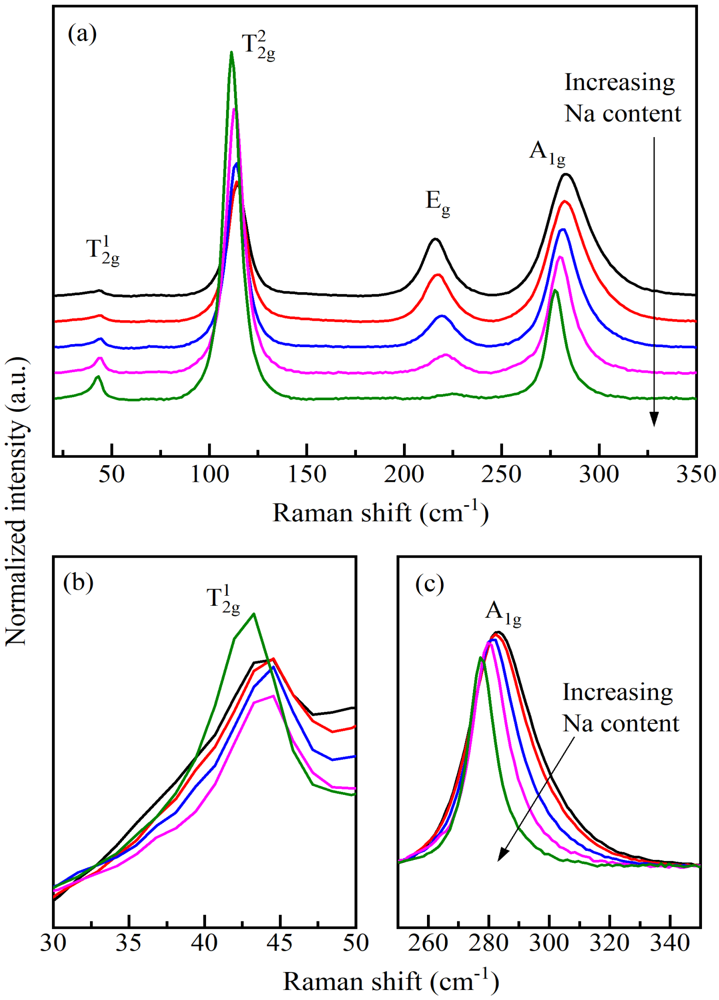

Figure 3.4: (a) Room temperature Raman spectra of Na doped $Cs_2AgBiCl_6$ compounds. Variation of (b) $T^1_{2g}$ mode and (c) $A_{1g}$ mode showing Raman shift and peak broadening with different Na concentration.

## 3.4 UV-vis spectroscopy

UV-vis diffuse reflectance data were collected over a spectral range of 300-800 nm to determine the optical band gap of the compositions using the well established Kubelka-Munk function, which expresses the absorbance as a function of diffused reflectance as given in the following equation;

$$F(R) = \frac{(1 - R_\infty)^2}{2R_\infty} \tag{3.1}$$

where, $R_\infty = R_{sample}/R_{standard}$ and is known as the reflectance of an infinitely thick material. The band gap of a material is calculated by using

Tauc plot between [F(R)h$\nu$]$^n$ and h$\nu$, where n is 1/2 for indirect transitions and 2 for direct transitions.

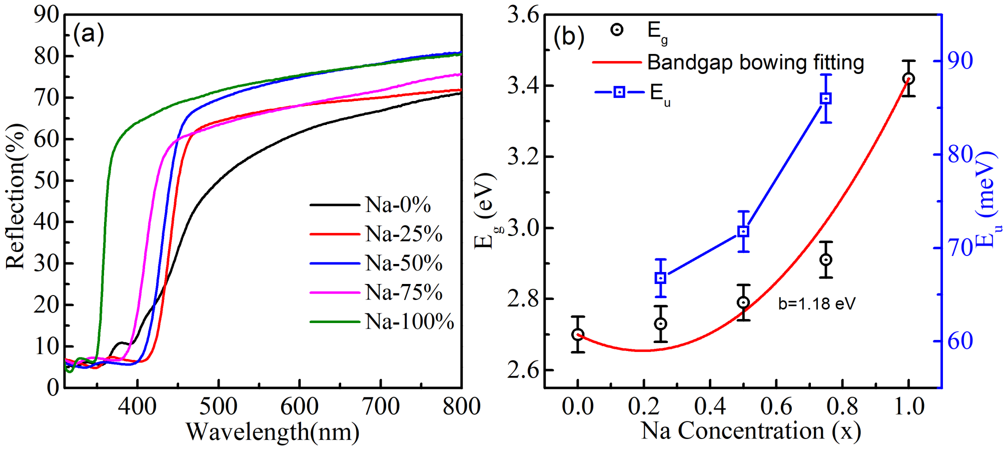

Figure 3.5: (a) Reflectance spectra of $Cs_2Ag_{1-x}Na_xBiCl_6$ compounds, (b) Variation of band gap energy and Urbach energy with different Na concentration.

Indeed, the optical band gaps ($E_g$) seem to increase systematically with rising Na-content. Figure 3.5(a) displays the diffuse reflectance spectra of the $Cs_2Na_xAg_{1-x}BiCl_6$ compositions. The trend of a systematic increase in the $E_g$ value from 2.7 eV in $Cs_2AgBiCl_6$ to 3.42 eV in $Cs_2NaBiCl_6$ is consistent with the electronic structure calculations reported in the literature [68]. Also, the Tauc plots presented in Figure 3.6, reveal the indirect nature of the gap. As per the theoretical calculations, the contribution of $4d^{10}$ orbital of Ag atoms to the valence band appears at -8.76 eV ($d_{5/2}$) and -9.32 eV ($d_{3/2}$), whereas for the $Cs_2NaBiCl_6$ compound, the Na $p_{3/2}$ level is at -29.63 eV and $p_{1/2}$ is at -29.81 eV. Thus, the sequential replacement of Ag with Na leads to the downward shift of the valance band maximum and upward shift of conduction band minimum and consequently results in increasing of $E_g$. It is worth noting that the variation of $E_g$ as a function of Na-ion concentration is not a straight line. Rather the data fits the relationship, $E_g(x) = (1-x)E_g(0) + xE_g(1) - bx(1-x)$, where $E_g(0)$ and $E_g(1)$ represent the end members of the compositions and $b$ is the bowing parameter of the band gap. The fitting shown in Figure 3.5(b) yields a considerably large value of $b = 1.18$ eV, in agreement with the theoretically predicted value of 1.03 eV [68]. Thus, in the mixed Ag/Na compositions the electrons and holes localize within the intermediate states and give rise to a considerable band gap bowing factor.

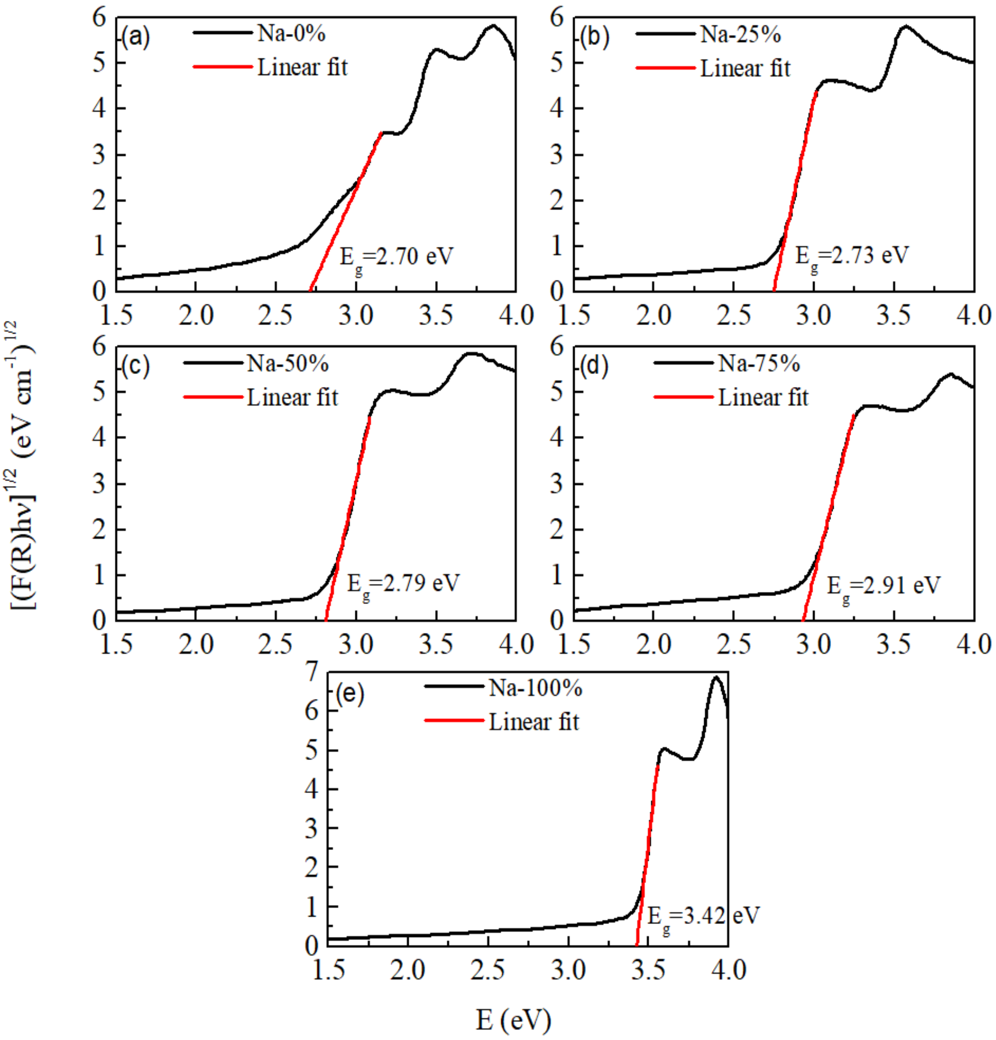

Figure 3.6: Tauc plot of $Cs_2Ag_{1-x}Na_xBiCl_6$ compounds.

## 3.5 Photoluminescence spectroscopy

Photoluminescence (PL) spectroscopy reveals intriguing aspects of the band structure and resulting optical properties of $Cs_2Na_xAg_{1-x}BiCl_6$ compositions. Figure 3.7(a) represents the steady-state emission spectra recorded on solid circular pellets using the excitation wavelength of 365 nm equipped with 2.5 nm entrance slit width and 5 nm exit slit width. The

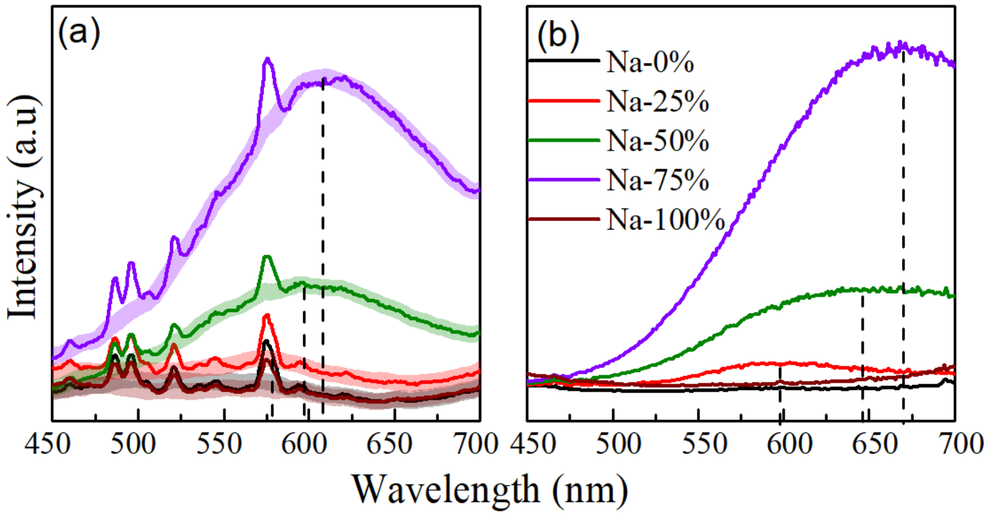

Figure 3.7: (a) Photoluminescence spectra of all the solid compositions and (b) compositions dissolved in ethanol solvent.

overall emission intensity of the spectra intensifies with the rising Na concentration, with a smooth, broad Gaussian-shaped curve that peaks around the orange-red emission (∼ 600 nm) of the visible light spectrum. Interestingly, the emission spectra also contain sharp spike-like features that peak at 486 nm and 496 nm (blue emission), 521 nm (green emission) and 576 nm (yellow-orange emission). In contrast to the broad emission peak, these abrupt spikes appear with the same intensity in all the compositions. Also, the wavelength at which they appear seems to remain unchanged, hinting that their origin lies in the surface defect states formed during the pelletization of the powder samples. To verify this, we recorded the emission spectra in liquid form by dissolving the sample powders in ethanol. As expected, the spike-like features disappear (Figure 3.7(b)) due to the solvent relaxation effect. The main emission peak in $Cs_2Na_{0.75}Ag_{0.25}BiCl_6$ results from the $6s^16p^1 \longrightarrow 6s^2$ allowed transitions with the highest intensity observed for 75% Na composition. The blue shift in the PL spectra of the mixed compositions is due to the solvent relaxation effect. In this case the solvent molecules assist in stabilizing and lowering of the excited state energy level by reorienting around the excited fluorophore results in the shifting of the emission peak. Besides, the sharp abrupt peaks which were earlier present in the PL spectra of solid samples got disappeared because the trap states produced by confinement get neutralized due to solvation of solute molecules in the relaxed phase.

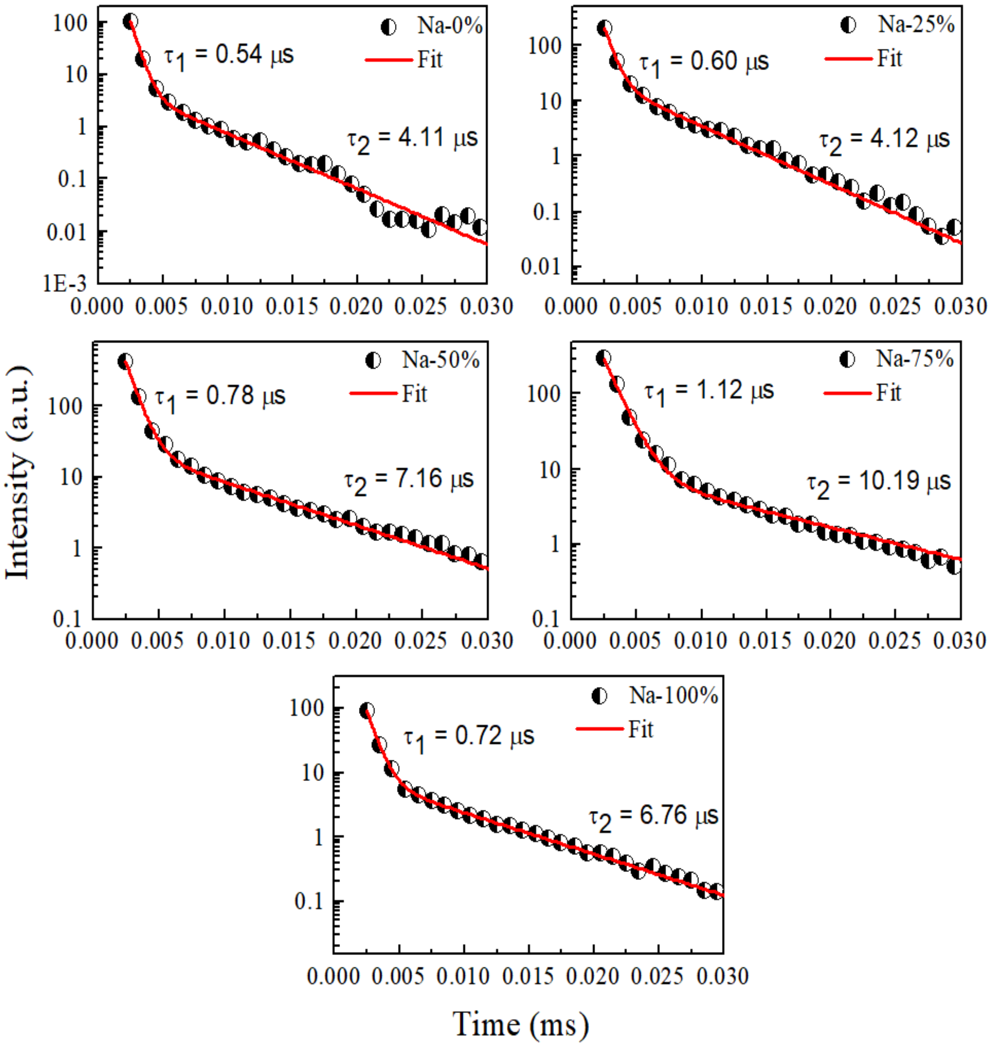

Figure 3.8: Photoluminescence decay profile of $Cs_2Ag_{1-x}Na_xBiCl_6$ compounds. The circles represent the experimental data of TRPL spectra and the red line represents the biexponential fitting of the data.

To establish the applicability of such luminescent material, estimating its charge transfer rate across the band gap is essential. Time-resolved photoluminescence (TR-PL) is an apt method to access such information. The intensity decay profiles of the $Cs_2Na_xAg_{1-x}BiCl_6$ compositions show that the de-excitation is not a simple one-step radiative decay process. It is easy to notice from Figure 3.8 that an additional timescale(s) consisting of fast and slow time components is needed to describe the TR-PL decay. For the sake of simplicity, we sum up this process to a bi-exponential function, $I(t) = I_1 e^{-t/\tau_1} + I_2 e^{-t/\tau_2}$, where $\tau_1$ and $\tau_2$ are the decay timescales and $I_1$, $I_2$ are the corresponding amplitudes. The decay life time increases with increase in Na concentration and the composition with 75% Na displays the most extended lifetime. However, for pure Na based composition the life time decreases.

Generally, in luminescent materials the charge carriers that are excited from the valence band maximum to the conduction band minimum de-excite through the near-band-edge emission process characterized by the lifetime $\tau_1$. A relatively shorter lifetime, $\tau_2$, characterizes the de-excitation process from an intermediate state between the band edges. In contradiction to this general observation, the $Cs_2Na_xAg_{1-x}BiCl_6$ compositions display a longer $\tau_2$, implying the presence of trap-states between the band edges [69]. These trap states can be explored by tuning the emission to higher wavelengths (lower energies) and observing its impact on decay lifetimes. Hence, we record TR-PL at three different values of emission wavelengths, one matching with the optical band gap energy, $E_1$ (near band-edge emission), and the other two energies, $< E_1$ (increasing wavelengths). Increasing the emission wavelength leads to a systematic increase in the decay lifetimes such that the process can be characterized as emerging from shallow and deep trap states. Further, the presence of deep trap states in 75% Na substituted compound results in the highest PL among the studied compositions. Extending the same argument to the end-members, $Cs_2AgBiCl_6$ and $Cs_2NaBiCl_6$, quenching of lifetime at higher wavelengths occurs in these compositions due to the absence of trap states which can be inferred from Figure 3.9.

At this point, it becomes imperative to explore the origin and stability of the trap states. Despite the large difference in the cationic radii of $Ag^+$ and $Na^+$, the XRD results suggest no change in crystal symmetry with systematic replacement of Ag with Na in the $Cs_2AgBiCl_6$ composition. Though the long-range structural order remains unchanged, the likely factor to affect the electronic properties of these compositions remains to be

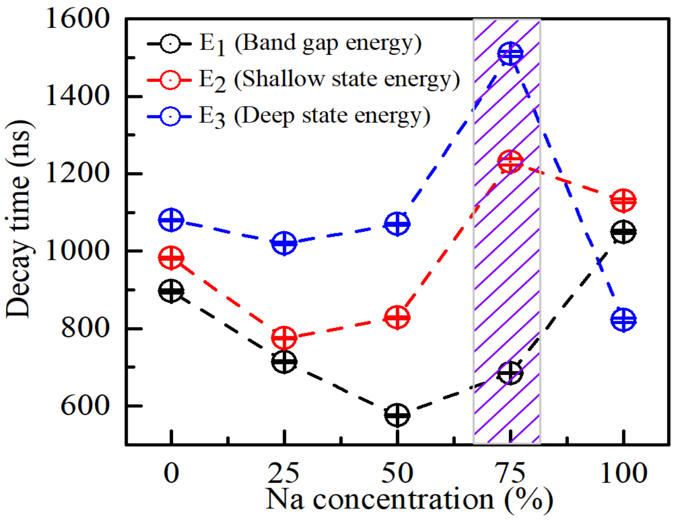

Figure 3.9: Variation of decay time profile at different emission energy $E_1$, $E_2$ and $E_3$ with increase in Na concentration in $Cs_2Ag_{1-x}Na_xBiCl_6$ compositions.

the local lattice distortion, taking place to accommodate the substitution of a transition metal ion with a strong alkali cation. Moreover, the band alignment in transitioning from $Cs_2AgBiCl_6$ to $Cs_2NaBiCl_6$ leads to a scenario where the valence band edge shifts downward, and the conduction band edge shifts upward. In the mixed Ag/Na compositions, the electrons and holes localize within the intermediate states formed by lattice distortions, giving rise to a considerably high band gap bowing parameter.

## 3.6 Electron-phonon interaction

In semiconductors, charge carriers primarily occupy within a narrow energy band near the edges, where electron-lattice interactions are mainly governed by long-wavelength phonons. Various factors, including the random distribution of crystallographic defects, impurities, doping, and external influences such as temperature and pressure, can introduce potential fluctuations in the electronic structure of the semiconductor. These fluctuations can create energy levels within the forbidden energy gap [70]. Such broadening of energy levels can intensify the electron-lattice scattering, especially in the doped semiconductors. By analyzing the Raman line shape and dispersion in the tail states of UV-vis spectra of mixed $Cs_2Na_xAg_{1-x}BiCl_6$ compositions, we aim to uncover the electron-phonon coupling strength and its role in stabilizing the populated trap states, which ultimately enhances photo-luminescence.

It is well known that the radiative and non-radiative recombination of carriers, in general, varies due to the exponential trap states near the band edges. Hence, we further analyze the band-edge broadening of the UV-vis spectra in terms of the Urbach tail states [71, 72], which can be potentially influenced by the chemical composition of the compounds. Quantitatively, the band edge broadening known as Urbach energy ($E_u$) can be derived from the slope of the linear exponential regime, [71, 73]

$$\alpha = \alpha_0 exp(\frac{h\nu - E_g}{E_u}) \tag{3.2}$$

where, $\alpha$ is the absorption coefficient, $\alpha_0$ is a constant, $E_g$ is the optical band gap, and $h\nu$ is the incident photon energy. We extract the Urbach energy, $E_u$, for each of the mixed Ag/Na compositions by plotting the graph between $\ln\alpha$ and $h\nu$, where the reciprocal of the slope gives the value of $E_u$. Figure 3.5(b) also represents the variation of $E_u$ with changing Ag/Na concentrations, which is an indication of rising disorder of phonon states in these mixed compounds. Further, an estimate of the electron-phonon interaction strength ($E_{e-p}$) comes from $E_u$ using the relation [74], $E_{e-p} = \frac{2E_u}{3K_BT}$. Thus, a higher Urbach energy implies stronger electron-phonon interaction and hence, should contribute heavily towards the formation of deep trap states, which in turn would result in enhanced PL properties. A greater understanding can be developed by focusing the stability of these trap states through electron-phonon interaction probing Raman spectroscopy.

The fundamental understanding of Raman spectroscopy is the inelastic scattering interaction of the incident photons with the material, giving rise to the phonon modes. These phonons are positioned at zone centre of the reciprocal lattice and give rise to a symmetric Raman profile, thereby conserving the momentum. However, relaxation process can occur in the

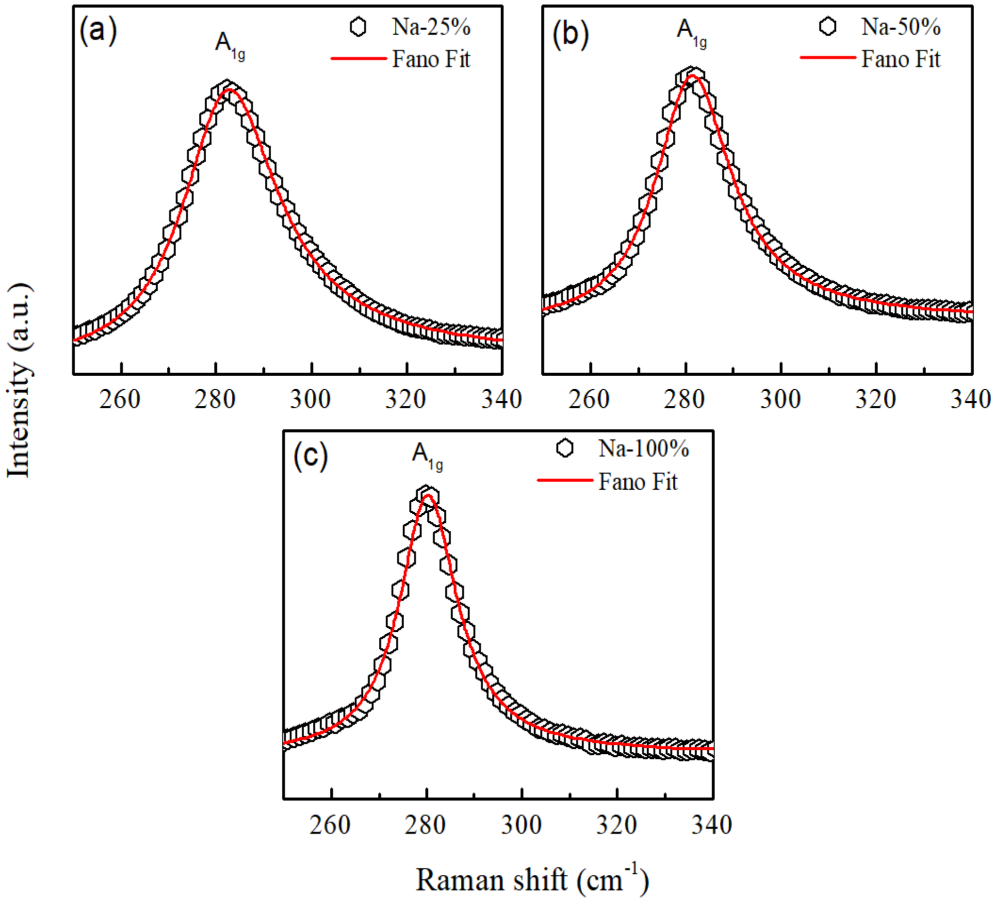

Figure 3.10: Fano fitting of $A_{1g}$ mode of the mixed Na/Ag compositions.

doped semiconductors wherein the phonons in proximity to zone centre contribute to the scattering process, leading to an asymmetric broadening of Raman profile. Such asymmetry in Raman profile, also known as the Fano resonance effect, is a characteristic feature of the material under study. In crystalline semiconductors the Fano resonance is known to originate either from heavy doping or from photo-excitation leading to phonon interference with the continuum electronic states and has an impact on the asymmetry broadening of Raman mode. Generally, the ions or atoms exhibiting longitudinal vibrations having their vibrational amplitudes are along the electric field and phonon propagation vector, also known as LO phonons may get affected to a greater extent than the other phonons. Realising this phenomena, here we considered the Raman line-shape of LO mode ($A_{1g}$) of these compounds to bring in the Fano effect into the picture. The asymmetric Raman peak can be expressed by the Breit-Wiger-Fano function [75, 76],

$$I(\omega) = I_0 \frac{|q + S(\omega)|^2}{1 + S(\omega)^2} + I_b(\omega) \tag{3.3}$$

where, $S(\omega) = \frac{2(\omega-\omega_p)}{\Gamma}$ is the reduced energy variable, $\omega_p$ is the phonon frequency, and $\Gamma$ is the linewidth. Here, $q$ is the asymmetry parameter that characterizes the interference between the discrete phonon and continuum spectra. A lower $q$ value is an indicator of stronger interference. Conversely, the inverse of $q$ signifies the electron-phonon coupling strength [74], $E_{e-p} \propto 1/|q|$. As depicted in Figure 3.11(a), $1/|q|$ increases with increase in Na concentration, reaching a maximum for 75% Na composition. We have previously obtained the estimate of $E_{e-p}$ from the Urbach energy analysis of the UV-vis spectra. Figure 3.11(a) also depicts that the compositional variation of $E_{e-p}$ extracted from UV-vis data and $1/|q|$ obtained from Raman analysis, follow the same trend.

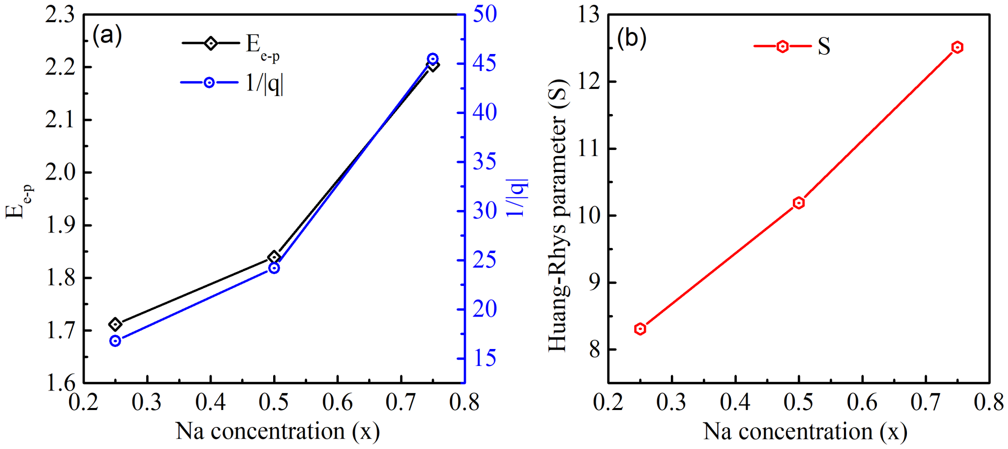

Figure 3.11: (a) Correlation of EPC strength ($E_{e-p}$ in terms of Urbach energy and $1/|q|$ from Fano effect) and (b) variation of Huang-Rhys parameter (S) with different Na concentration in the mixed compositions.

In polar semiconductors, scattering mechanisms are generally induced by Fröhlich interactions between electrons and optical (LO) phonons. An alternate estimate of the strength of such electron-phonon coupling [77] in the form of Huang-Rhys parameter ($S$), can be obtained using the relation, $E_{Stokes}=2S\hbar\omega_{LO}$. Taking the LO phonon mode ($A_{1g}$) energy and the Stokes shift energy, which is the difference between absorption and emission energies of the PL spectra, the value of $S$ is extracted for all the compositions.

In line with the inference drawn so far from other spectroscopic analysis, $S$ increases with increasing Na content ultimately indicating stronger electron-phonon coupling as shown in Figure 3.11(b).

A weak electron-phonon coupling in $Cs_2AgBiCl_6$ along with the indirect nature of its band gap favours a non-radiative recombination mechanism, where the incident photon with an excitation wavelength of 365 nm is unable to change the crystal momentum to favour the radiative recombination of free excitons. With the incorporation of $Na^+$ into the lattice, trap states are produced in between the forbidden energy region which can easily absorb the difference in crystal momentum between the free excitons forming the self trapped excitons (STE). An electron which gets excited to higher levels first moves to the bottom of the conduction band via vibrational relaxation and internal conversion decay mechanisms. The electrons get trapped in these intermediate states (trap states) before recombination with the holes. With further increase in $Na^+$ concentration, the trap states are produced much deeper into the forbidden region as supported by the red shift of the maxima of the PL emission spectra. Also, the full-width-half-maximum (FWHM) of the PL spectra can be utilized to infer the lattice relaxation energy ($E_{LR}$) through the equation [78], $FWHM \propto \sqrt{2E_{LR}K_BT}$. As the FWHM is smallest for 75% Na composition, its $E_{LR}$ which enhances the stable STE states in between the band edges, is also the least in the series. On the other hand, both the end members of this series display a much higher $E_{LR}$, implying metastable trap state with negligible luminescence. As discussed earlier, widening of the band-gap takes place with increasing Na content in the $Cs_2Ag_{1-x}Na_xBiCl_6$ compositions. Formation of stable STE states within this gap increases the possibility of intra-band photoexcitation, leading to long lasting luminescence.

## 3.7 Summary

In summary, the optical properties of Na-substituted $Cs_2AgBiCl_6$ have been explored to find a long-lasting luminescent composition in the lead-free double perovskite family. Time-resolved photoluminescent studies on the trap-correlative carrier dynamics indicate the long-lived emission component increase upon Na substitution. Composition with 75% Na ion replacing the Ag ions in $Cs_2AgBiCl_6$ shows the longest-lived decay process. The substitution of a strongly electropositive ion in $Cs_2AgBiCl_6$ composition leads enhancement of self-trapped exciton states. Such trap-assisted de-excitation mechanism slows down the electron-hole recombination process. The origin of the trap states lies in the local lattice distortion, brought to the fore through various crystal structure and electronic properties investigations. Combining the Urbach tail state analysis and Fano effect in Raman spectra laid out the interaction of strong electron-phonon coupling in the mixed composition that stabilizes the self-trapped exciton states resulting enhanced luminescence. This study achieves a better understanding of decay lifetime, charge transfer mechanism and optical properties for the Na-substituted $Cs_2AgBiCl_6$ compounds.

# Chapter 4

# Study of Cr, Mn and Yb substituted $Cs_2AgMCl_6$ (M=Bi and In) halide double perovskite

## 4.1 Overview

The two widely studied HDPs, $Cs_2AgBiCl_6$ (CABC) and $Cs_2AgInCl_6$ (CAIC) compositions show excellent thermal and air stability [79], but pose a challenge in its immediate integration into the optoelectronic sector. $Cs_2AgBiCl_6$ is reported to have an indirect bandgap of ∼2.5 eV resulting in a weak optical absorption and emission response, while $Cs_2AgInCl_6$ shows a wide direct bandgap of ∼3.5 eV which is incompatible with the generation of solar energy. Numerous endeavors have been undertaken to enhance the photoluminescence quantum yield (PLQY) of these halide double perovskites, with one such method being elemental substitution [80, 81]. A substantial improvement in the PLQY was recently reported upon a large percentage of transition metal substitution in CABC and CAIC. M. Jeevaraj *et al.* [82, 83] demonstrated significant NIR emission in up to 68% Cr-doped CABC and high luminescence in the visible spectrum for 68%

Mn-doped CAIC. Conversely, Zhao *et. al.* [84], stated that their attempt to incorporate 10% Cr into CAIC via a solid-state process resulted in the precipitation of $CrCl_3$ on the sample's surface, leading to the integration of a much smaller percentage of $Cr^{3+}$ in the final composition. Despite this, the substituted composition exhibited high emission in both visible and NIR regions due to the spin-allowed $d-d$ transitions of the transition metal ions. It is, however, surprising that the substantial amount of $Cr^{3+}$ or $Mn^{3+}$ ions reported in Ref. [82] did not lead to self-quenching, which would negatively impact the PLQY properties. Instead, a notable improvement in the PL properties of CABC was claimed.

For potential applications as photodetectors, LEDs and solar cells, apart from optical properties it is essential to elucidate the underlying charge transport properties of these materials. Dielectric spectroscopy offers a profound insight into these challenges by employing a range of parametric tools, such as dielectric permittivity, AC conductivity, complex impedance, and electric modulus. Recent progress in understanding dielectric behavior is showcased through the qualitative analysis of imaginary modulus plots, characterized by the presence or absence of relaxation peaks, which reveal localized or non-localized conduction phenomena. Additionally, a quantitative grasp of transport mechanisms can be achieved by analyzing the material's relaxation time and activation energy. With the keen interest to explore the optoelectronic properties of halide double perovskites, we have synthesized Cr, Mn and Yb substituted $Cs_2AgBiCl_6$ and $Cs_2AgInCl_6$ with 10% doping concentration at Bi and In sites respectively. We have used the notations for all the studied compositions, $Cs_2AgBi_{0.9}Cr_{0.1}Cl_6$ (Cr-CABC), $Cs_2AgIn_{0.9}Cr_{0.1}Cl_6$ (Cr-CAIC), $Cs_2AgBi_{0.9}Mn_{0.1}Cl_6$ (Mn-CABC), $Cs_2AgIn_{0.9}Mn_{0.1}Cl_6$ (Mn-CAIC), $Cs_2AgBi_{0.9}Yb_{0.1}Cl_6$ (Yb-CABC), and $Cs_2AgIn_{0.9}Yb_{0.1}Cl_6$ (Yb-CAIC) for reference in this chapter.

## 4.2 Stability and compositions

The thermal stability of all the prepared samples was investigated using TGA measurement (Figure 4.1). Both $Cs_2AgBiCl_6$ and $Cs_2AgInCl_6$ show higher thermal stability as compared to the conventional hybrid perovskites. Besides, the substituted compounds show further enhanced thermal stability over 500 °C.

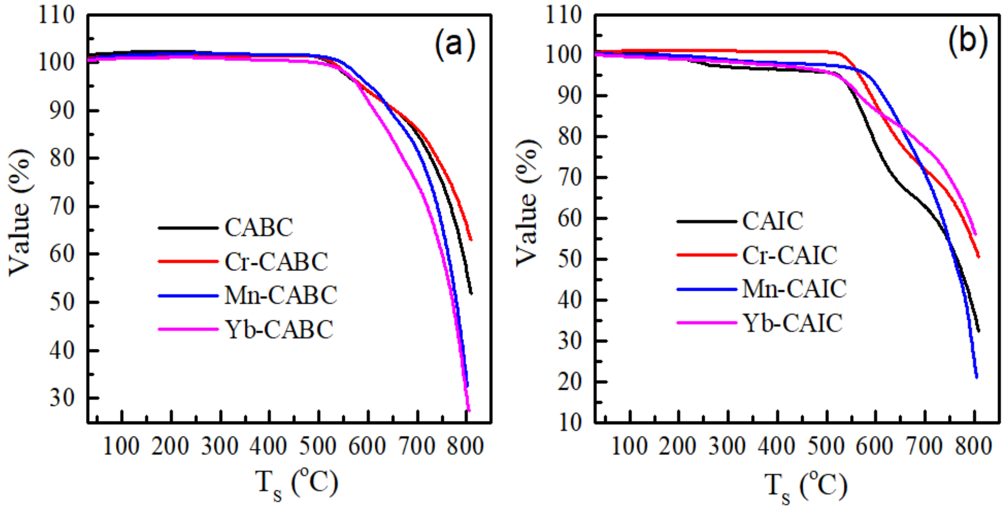

Figure 4.1: TGA spectra of (a) Bi based HDPs and (b) In based HDPs.

| Compound | Cs | Ag | Bi | In | Cr | Mn | Yb | Cl |
|---|---|---|---|---|---|---|---|---|
| CABC | 22.0 | 10.7 | 10.8 | - | - | - | - | 56.5 |
| Cr-CABC | 21.6 | 11.0 | 10.6 | - | 1.1 | - | - | 55.7 |
| Mn-CABC | 22.2 | 10.7 | 10.4 | - | - | 0.5 | - | 56.2 |
| Yb-CABC | 23.8 | 8.8 | 10.4 | - | - | - | 1.0 | 56.0 |
| CAIC | 21.2 | 9.9 | - | 9.9 | - | - | - | 59.0 |
| Cr-CAIC | 20.7 | 11.6 | - | 9.3 | 2.7 | - | - | 55.7 |
| Mn-CAIC | 22.3 | 11.4 | - | 10.2 | - | 0.7 | - | 55.4 |
| Yb-CAIC | 21.3 | 10.5 | - | 9.5 | - | - | 0.5 | 58.3 |

Table 4.1: Elemental compositions (in atomic %) for each perovskite compound.

Energy dispersive X-ray spectroscopy (EDS) measurement indicates the stoichiometry of the synthesized HDPs as provided in Table 4.1. The measured dopant to Bi/In ratio are found to be approximately 9:1 implying both $Cr^{3+}$ and $Yb^{3+}$ ion occupy the desired lattice site by replacing $Bi^{3+}$ and $In^{3+}$ in $Cs_2AgBiCl_6$ and $Cs_2AgInCl_6$ respectively.

## 4.3 Structural properties

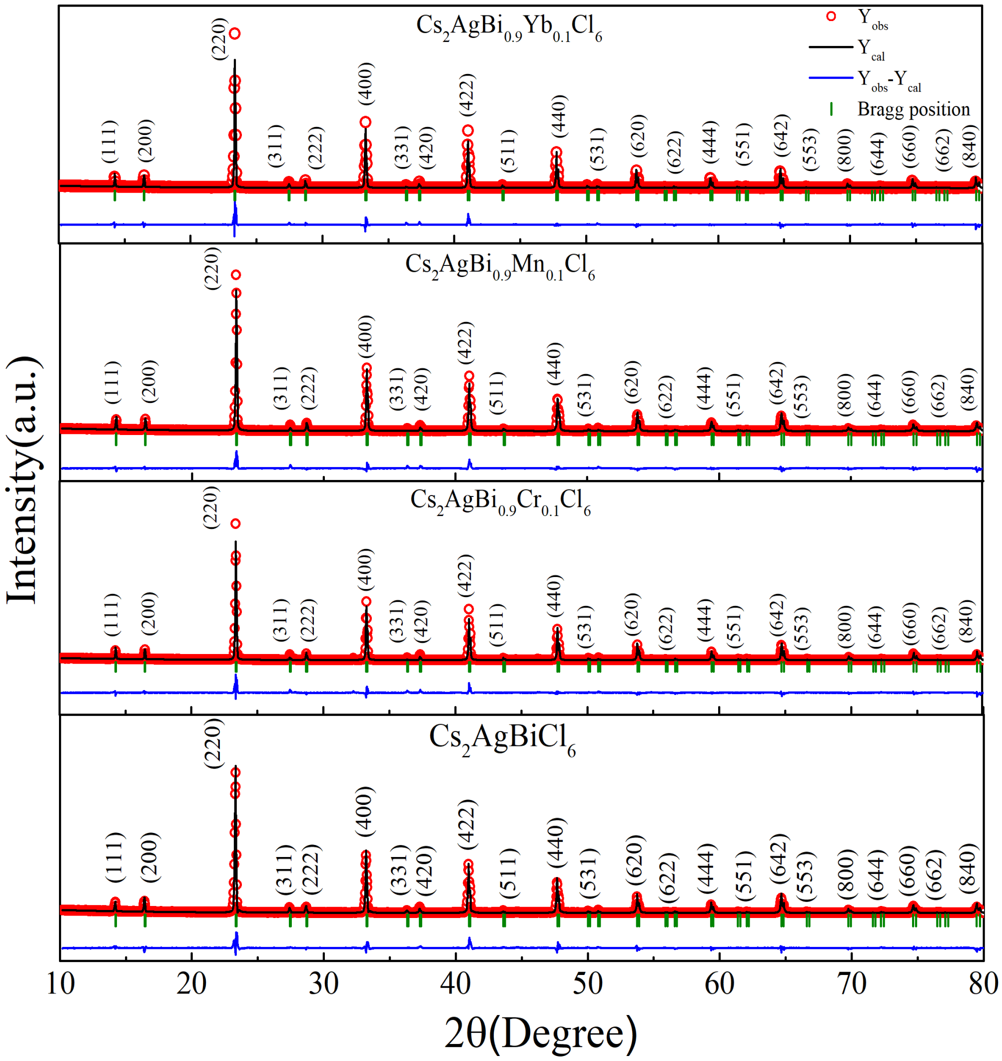

Figure 4.2: Rietveld refinement of Bi based HDPs displaying cubic symmetry.

Figure 4.2 and Figure 4.3 represent the Rietveld refinement of X-ray diffraction (XRD) spectra of the synthesized HDPs. Crystallographic analysis reveals the formation of single phase cubic crystal structure with a centrosymmetric $Fm\bar{3}m$ space group. Structural refinements of all the

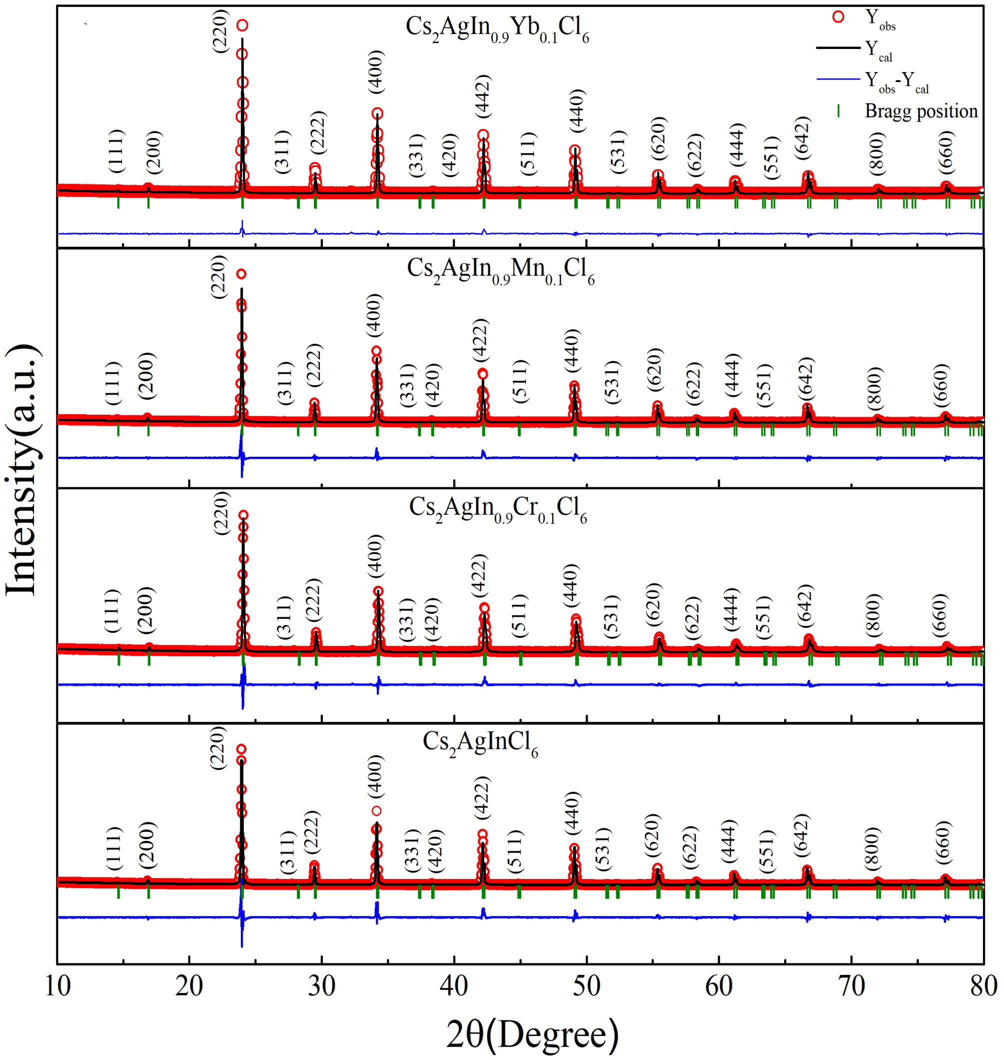

Figure 4.3: Rietveld refinement of In based HDPs displaying cubic symmetry.

compounds carried out by Rietveld method [60] yields the lattice parameter to be 10.78 Å for $Cs_2AgBiCl_6$ and 10.49 Å for $Cs_2AgInCl_6$. High quality crystalline phase is reflected in sharp and well-defined XRD peaks. The crystal structure of $Cs_2AgBiCl_6$ and $Cs_2AgInCl_6$ forms the rock-salt type ordered structure consisting of alternately arranged $[AgCl_6]^{5-}$ and $[BiCl_6]^{3-}/[InCl_6]^{3-}$ octahedra with $Cs^+$ ion occupies the centre of the cubic octahedral cavity. Partial substitution of $Bi^{3+}$ and $In^{3+}$ with cations like Cr, Mn or Yb which have smaller ionic radii, leads to a slight decrease of the lattice constants and no change in the symmetry of the unit cell. The lattice constants are listed in Table 4.2. Importantly, we do not observe any extra peaks in the XRD profile that could be attributed to precipitation of secondary phases, thus confirming that substitutions as high as 10% of Cr or Yb do form single phase compositions of CABC and CAIC.

| Temperature (K) | Lattice constant (Å) | Volume (Å$^3$) | $\chi^2$ | R$_p$ | R$_{wp}$ | R$_{exp}$ |
|---|---|---|---|---|---|---|
| CABC | 10.78(6) | 1255.12(3) | 17.7 | 29.3 | 31.2 | 7.43 |
| Cr-CABC | 10.76(9) | 1249.11(2) | 11.5 | 23.6 | 24.6 | 7.25 |
| Mn-CABC | 10.76(8) | 1249.12(2) | 11.4 | 23.5 | 24.6 | 7.25 |
| Yb-CABC | 10.76(9) | 1249.07(2) | 11.1 | 23.1 | 23.8 | 7.15 |
| CAIC | 10.49(1) | 1154.45(0) | 25.9 | 28.8 | 29.9 | 5.87 |
| Cr-CAIC | 10.46(7) | 1146.74(0) | 8.81 | 24.3 | 24.1 | 8.12 |
| Mn-CAIC | 10.48(8) | 1153.87(1) | 14.7 | 21.6 | 22.1 | 5.75 |
| Yb-CAIC | 10.47(7) | 1150.16(1) | 4.11 | 16.6 | 16.2 | 7.97 |

Table 4.2: Table shows the lattice parameter, cell volume and Rietveld refinement fitting parameters of all compositions.

## 4.4 EPR spectroscopy

The fact that Cr, Mn and Yb ions indeed occupy the octahedral lattice sites by partially replacing Bi and In in $Cs_2AgBiCl_6$ and $Cs_2AgInCl_6$, respectively, is further confirmed from the electron paramagnetic resonance (EPR) spectra of all the compositions recorded at room temperature. The representative g-factor can be calculated from the first-derivative of magnetic resonance absorption signal using the formula; $g = \frac{h\nu}{\mu_B B_0}$, where h is Planck's constant, $\mu_B$ is Bohr magneton, $\nu$ is the resonance frequency of sample cavity and $B_0$ is the centre of the resonance signal. Pure $Cs_2AgBiCl_6$ compound shows an intense paramagnetic signal with an effective g-value at 2.01 due to the presence of lone pair electrons of $Bi^{3+}$ octahedral species in the compound at room temperature. (Figure 4.4) A clear signal associated with Kramer's doublet for octahedrally coordinated $Cr^{3+}$ ions with an effective $g$-value of 1.99 is seen from the EPR spectra of Cr-CAIC and Cr-CABC in Figure 4.4. The EPR spectrum of Cr-CABC shows six equally spaced hyperfine structure. The $3d^3$ electronic configuration of $Cr^{3+}$ has an electron spin of $s = \frac{3}{2}$ and the ground state is $^4F_{3/2}$. The four-fold spin degeneracy of $Cr^{3+}$ ion results in a zero field splitting of Kramer's doublet $|\pm\frac{3e}{2}>$ and $|\pm\frac{1}{2}>$. The application of a microwave frequency field further splits the doublet giving rise to another transition of $|\pm 1>$ state in the EPR spectra showing the sextet hyperfine lines. In contradiction to CABC, pure CAIC exhibits no EPR spectra due to the absence of any unpaired electron. However, for Cr-CAIC compound, two EPR signals arise owing to the the Kramer's doublet of $Cr^{3+}$ ion with an effective g-value of 1.99. Again, the substitution of Mn in the compound also verified from the the presence of hyperfine lines in case of Mn-CABC and Mn-CAIC compounds. Similarly, both the Yb contained compounds show weak hyperfine line splitting corresponding to $Yb^{3+}$ ion with an effective g-value of 2.01. For the present discussion, it suffices to know that the 10% Cr, Mn or Yb substitution at Bi site in CABC and In site in CAIC has indeed taken place.

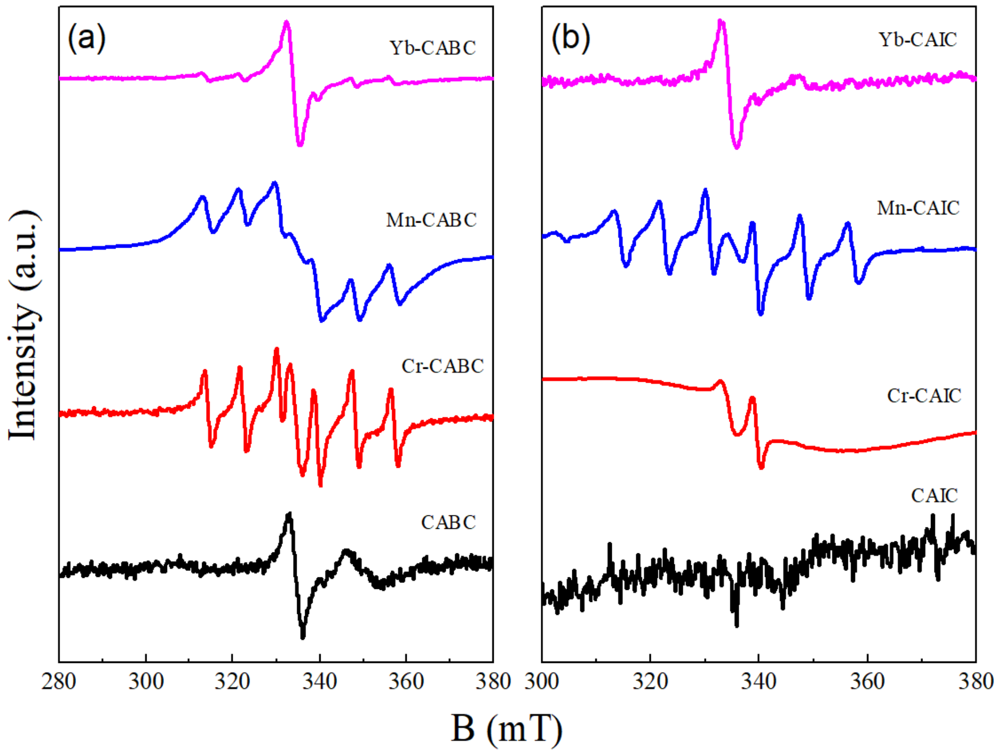

Figure 4.4: EPR spectra of (a) Bi based HDPs and (b) In based HDPs.

## 4.5 Optical properties

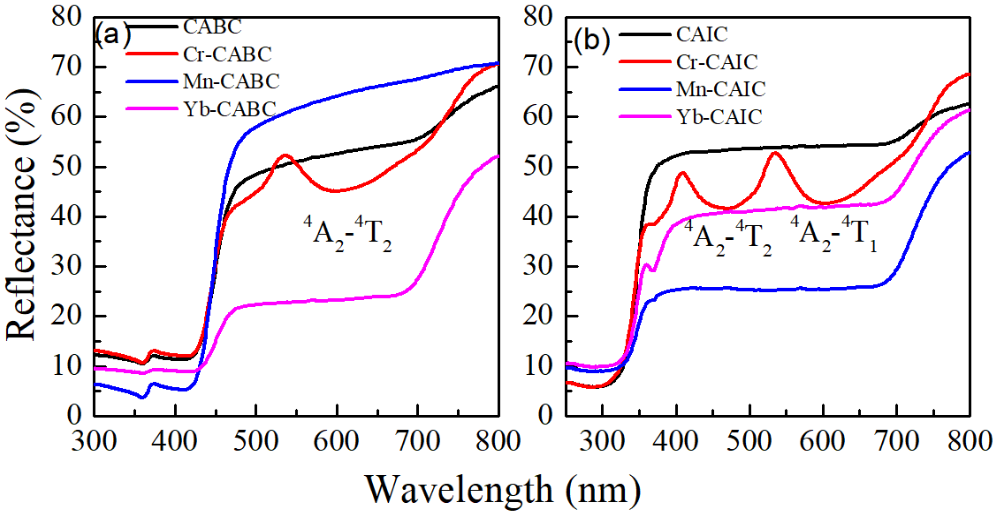

Figure 4.5: Diffuse reflectance spectra of (a) Bi based HDPs and (b) In based HDPs.

The impact of elemental substitution on the electronic structure of the HDPs can be deduced from the UV-vis diffuse reflectance spectra as shown in Figure 4.5. The Tauc plot using Kubelka-Munk function reveals an indirect band gap nature of Bi-based HDPs and direct band gap nature of In-based HDPs. The band gap of each composition is provided in table 4.3. Additionally, the spectra for Cr-substituted compounds show some peculiar features that reflect the inherent nature of the 3*d*-level. Firstly, a sharp decline in the reflectance spectra is observed in Cr-CABC (∼2.75 eV) and in Cr-CAIC (∼3.5 eV), ascribed to the electron transition between valence band and conduction band. Following the Tanabe-Sugano [85] energy level diagram for the crystal field splitting of $3d^3$ energy levels of $Cr^{3+}$ in $[CrCl_6]^{3-}$ octahedral symmetry, the peak centred at 2 eV in Cr-CABC is attributed to the $d-d$ transition of $^4A_2 \longrightarrow {}^4T_2$ and the peaks centred at 2.65 eV and 2 eV in Cr-CAIC are due to the $^4A_2 \longrightarrow {}^4T_1$ and $^4A_2 \longrightarrow {}^4T_2$. Using these peak frequencies we extract the Racah parameter (B) representing the repulsive strength between the states of same multiplicity to be 553 $cm^{-1}$. The octahedral crystal field splitting energy (Δ) turns out to be 16590 $cm^{-1}$. For an isolated free radical of $Cr^{3+}$, B has a value of 965 cm$^{-1}$, hence, its decreased value in Cr-substituted halide perovskites observed here, imply a delocalization of Cr$^{3+}$ electrons within the octahedral complex, and should impact the charge transport of these compositions.

| Compound | Band gap (eV) | Compound | Band gap (eV) |
|---|---|---|---|
| CABC | 2.60 | CAIC | 3.66 |
| Cr-CABC | 2.62 | Cr-CAIC | 3.69 |
| Mn-CABC | 2.70 | Mn-CAIC | 3.52 |
| Yb-CABC | 2.43 | Yb-CAIC | 3.56 |

Table 4.3: Band gap of each perovskite compound.

While both the Mn-substituted compounds, no d-d transition feature is found. This ambiguity can be understood from the chemical hybridization model, where Cr based compound has smaller octahedral splitting energy ($\Delta_0$) attributed to the reduced electronic repulsion between $t_{2g}$ and $e_g$ level that facilitates the d-d electronic transition. Adversely, Mn based compound has a larger $\Delta_0$ due to the strong electronic repulsion between $t_{2g}$ and $e_g$ level for which no d-d transitional peak is seen in diffuse reflectance spectra.

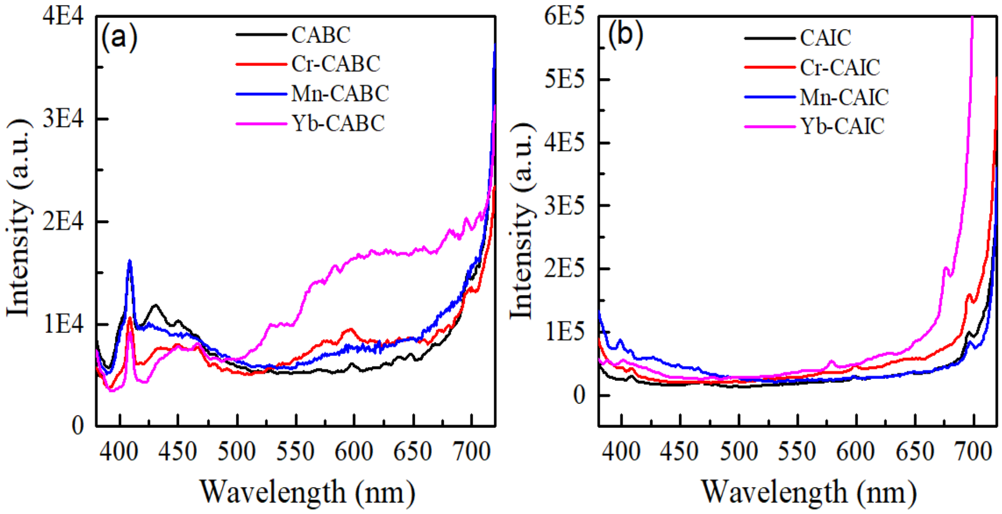

Figure 4.6: Photoluminescence spectra of (a) Bi based HDPs and (b) In based HDPs.

The optical behaviour of such halide double perovskites can be determined from the photoluminescence property of the material. Figure 4.6 shows the steady state PL spectra of solid samples of all the compositions which show no photoluminescence behaviour. Indeed, compounds with such high concentration of substituent ions should not exhibit emission features as the electron-hole pairs formed during excitation are readily allowed to quench through the formation of intermediate in-gap states. High doping also increases the probability of charge carrier population in the conduction band affecting the charge-transport properties and conduction processes in such halide perovskites. The present PL results seemingly contrast the previous reports by Ref. [82] which claimed high PLQY in 68% Cr substituted CABC. On the other hand, Ref. [84] claims that they could not achieve 10% Cr substitution in CAIC as Cr precipitates out in the form of $CrCl_3$ secondary phase, leaving very small amount of Cr (In/Cr ratio of 23:1) in the CAIC halide perovskite matrix and the high PLQY could be due to the formation of stable trap states in between the band edges. Further, to explore the charge conduction process and transport mechanism in these halide double perovskites, a systematic investigation on electronic property was carried out.

## 4.6 Electronic properties

### 4.6.1 Frequency dependent dielectric and impedance studies

Complex Impedance Spectroscopy (CIS) has been emphasized as an inevitable experimental technique to get a deeper insight into the charge carrier transport properties and relaxation process of a dielectric material. A quantitative analysis of dielectric permittivity and impedance measurement was carried out to explore many electrical properties such as dynamics of charge carriers, energy storage and dissipation over a wide range of frequency and temperature. A direct implication of the band gap is reflected in the impedance characteristics of these HDPs. Among the Bi-

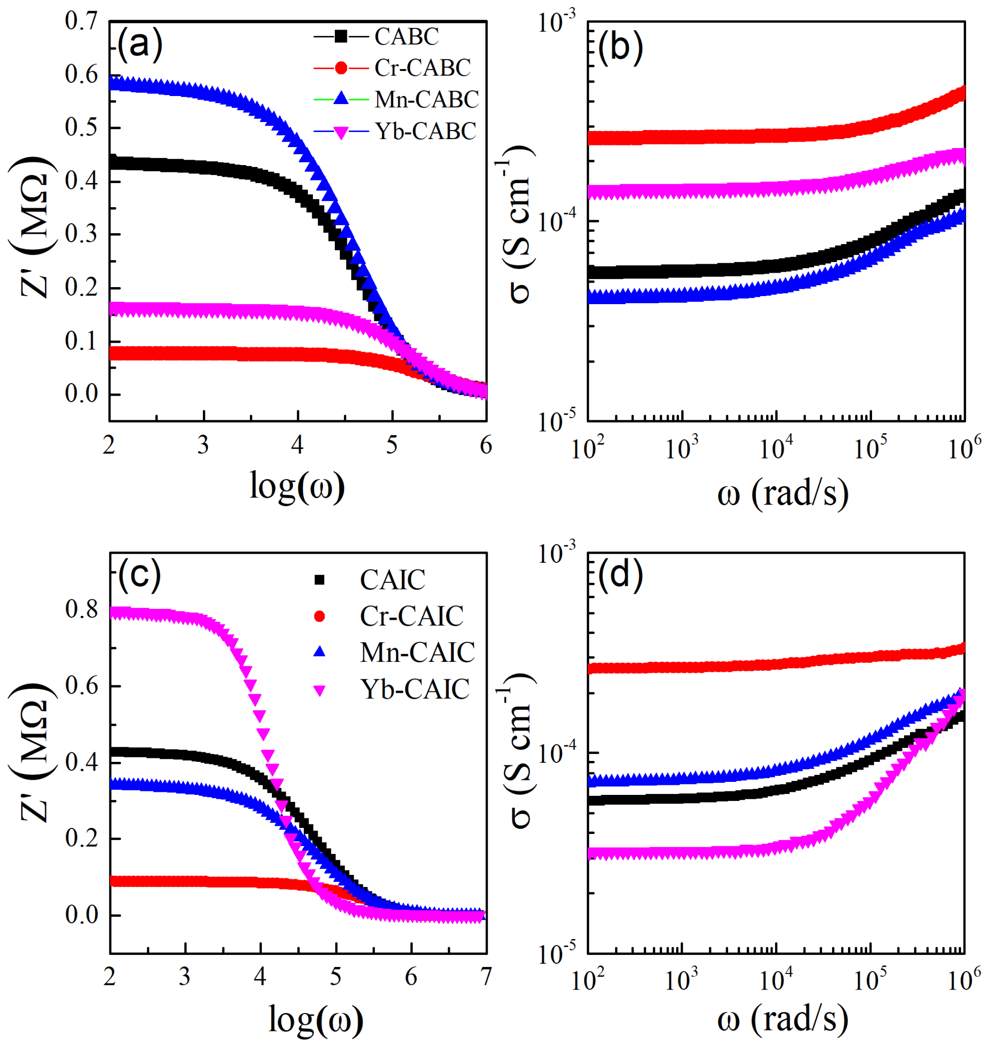

Figure 4.7: (a) Frequency dependent real impedance (Z'), (b) ac conductivity of Bi based HDPs and (c) frequency dependent real impedance (Z'), (d) ac conductivity of In based HDPs.

based HDPs, Mn-CABC shows higher impedance (Z') owing to the higher gap energy between VB and CB. The hybridized Mn orbital makes the charge carriers more localized hindering the electron transport between the band edges. In other hand, impedance of Cr-CABC decreases compared to pure CABC due to the availability of more mobile charge carriers with the incorporation of $Cr^{3+}$ ions where the empty $e_g$ orbital is readily available for electron transport. Further, the lower gap energy of Yb-CABC implies the more conducting nature resulting a lower value of Z'. Again, the peak broadening in the imaginary part of impedance indicates the enhancement of relaxation process. Figure 4.7 shows the impedance curve of all the perovskite compounds. Considering the In-based HDPs, Yb-CAIC shows higher Z' compared to pure CAIC due to the presence of highly localized Yb-4f orbital and In-4d orbital where it is quite difficult to withdraw electrons for transport. However, Cr and Mn substitution provides availability of charge carriers that assists in the reduction of impedance value and the conductivity increases. In both Cr-based halide perovskites, conductivity increases showing their potency towards semiconductors, batteries and detector applications.

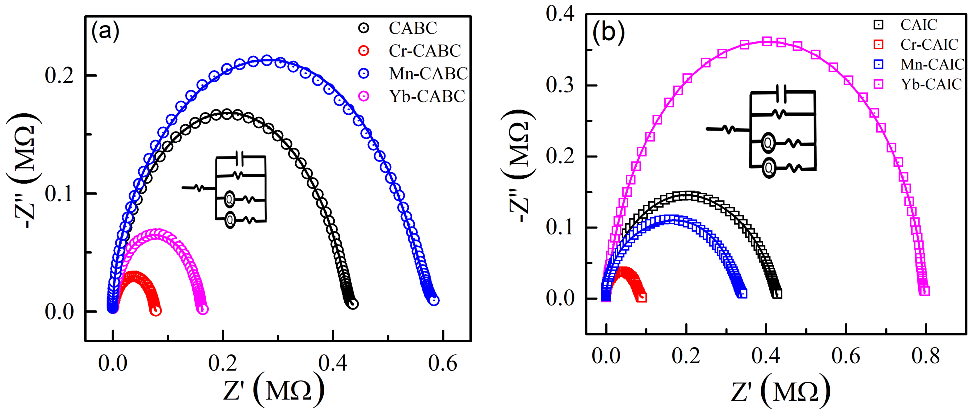

Figure 4.8: The Nyquist plot of (a) Bi based HDPs and (b) In based HDPs and the equivalent circuit model used to fit the data.

| Compound | R(Ω) | C(F) | R(Ω) | A(S.sec$^n$) | n | R(Ω) | A(S.sec$^n$) | n | R(Ω) |
|---|---|---|---|---|---|---|---|---|---|
| CABC | 4.1E5 | 9.7E-7 | 3.2E5 | 1.2E-6 | 0.99 | 3.4E5 | 1.3E-6 | 0.65 | 3.6E5 |
| Cr-CABC | 7.4E4 | 9.9E-6 | 7.6E4 | 1.1E-5 | 0.83 | 7.8E4 | 1.1E-5 | 0.86 | 7.8E4 |
| Mn-CABC | 5.4E5 | 1.1E-6 | 4.0E5 | 1.2E-6 | 0.72 | 3.9E5 | 1.1E-6 | 0.76 | 4.1E5 |
| Yb-CABC | 1.5E5 | 2.5E-6 | 1.6E5 | 1.0E-6 | 0.93 | 3.2E5 | 1.4E-6 | 0.98 | 3.1E5 |
| CAIC | 3.9E5 | 1.1E-6 | 2.9E5 | 1.2E-6 | 0.71 | 2.8E5 | 1.1E-6 | 0.76 | 2.9E5 |
| Cr-CAIC | 8.5E4 | 1.0E-5 | 8.4E4 | 1.1E-5 | 0.76 | 8.7E4 | 1.1E-5 | 0.82 | 8.8E4 |
| Mn-CAIC | 3.1E5 | 1.1E-6 | 2.3E5 | 1.2E-6 | 0.71 | 2.2E5 | 1.1E-6 | 0.76 | 2.4E5 |
| Yb-CAIC | 7.7E5 | 7.5E-7 | 1.6E5 | 1.6E-6 | 0.58 | 1.4E5 | 6.4E-7 | 0.57 | 1.7E5 |

Table 4.4: Various parameters derived from Nyquist plot fitting of Cr, Mn and Yb doped $Cs_2AgBiCl_6$ and $Cs_2AgInCl_6$ compounds.

Further, the increase in conducting nature of the compounds reflects in squeezing of Nyquist plot or Cole-Cole plot, which is defined as the plot between real part $Z'(\omega)$ and imaginary part $Z''(\omega)$ of complex impedance $Z^*(\omega) = Z'(\omega) - jZ''(\omega)$ as shown in Figure 4.8. The inset figure shows the equivalent circuit model consisting of various resistors and capacitors used to fit the Cole-Cole plot. The perfect semicircle in a Niquist plot of any dielectric material corresponds to the effect of grain, grain boundary and electrode-sample interface varying with high to low frequency. However, the combined contribution of all these effects along with the addition of constant phase elements (Q) is seen in the deformed Niquist plot fitted using ZSimWin software in our case of studies. The constant phase element impedance is defined as, $Z_Q = 1/A(j\omega)^n$. The constant phase element varies from an ideal resistance to an ideal capacitance as the value of n increases from 0 to 1. All the parameters obtained from the fitting of Niquist plot is provided in Table 4.4.

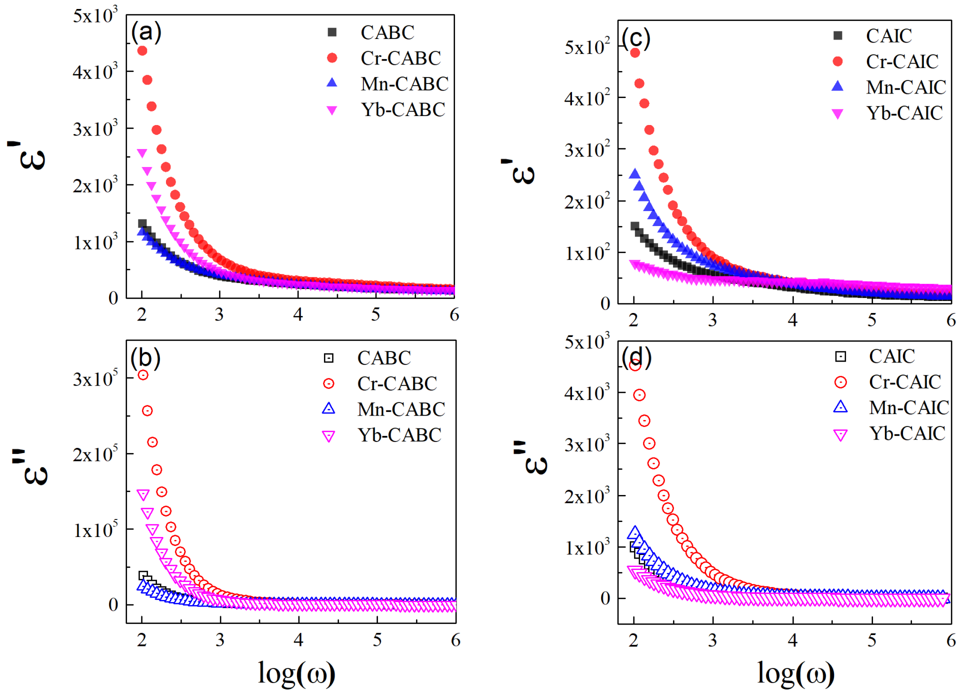

Figure 4.9: (a) Dielectric constant and (b) dielectric loss of Bi based HDPs and (c) dielectric constant and (d) dielectric loss of In based HDPs with varying frequency.

The dielectric characteristics of a material is a complex quantity involving the real part ($\epsilon'$) known as dielectric constant and an imaginary part ($\epsilon''$) known as dielectric loss as given in the following equation;

$$\epsilon^* = \epsilon' - j\epsilon'' \tag{4.1}$$

The higher value of dielectric constant at low frequency as shown in Figure 4.9 can be attributed to the inherent polar nature of the molecule. The polarity of the studied compositions is highly influenced by the electronegativity difference between the metal-halide bonds in the alternately arranged octahedra. This leads to the dynamical disorder in the lattice with the application of external field, which breaks the inversion symmetry causing the polarization in these compounds. In general, the low frequency region of dielectric part consists of all types of polarization with the dominated relaxation component (orientational and interfacial polarization), while the deformation component of polarizibility is governed by the ionic and electronic polarizations at higher frequency range [86]. Syndicating with Koop's theory, the high dielectric constant at low frequency is attributed to the Maxwell-Wagner interfacial polarization which elucidate the dielectric materials comprising conducting grains separated by highly resistive grain boundaries [87].

Initially the presence of space charge polarization at the grain boundaries generates a potential barrier that leads to the accumulation of charge carriers at the grain boundaries resulting in high dielectric constant. Further, with increase in frequency, dielectric constant gradually decreases due to the decrease in space charge polarization effect in the compounds. Interestingly, the high conductivity shown by Cr-CABC and Cr-CAIC compositions among the studied perovskites, also shows higher dielectric constant indicating their potential application as energy storage devices. With the high electronegativity Cr substitution, the ionic character increases which can easily polarize the electric field inducing high dielectric constant. While Mn substituted compounds do not show any significant effect on the dielectric properties compared to their parent compositions. Further, the dielectric characteristic of a material is purely capacitive in nature and a clear interpretation of the variation of dielectric constant of these perovskites can be revealed from the capacitance value obtained from Nyquist plot fitting. Additionally, as electrical conductivity improves, charge carriers exhibit greater mobility, enabling more efficient dipole formation and orientation along the field direction and directly affect the polarization strength of the material. This leads to an increase in the dielectric constant compared to the parent compounds.

### 4.6.2 Temperature dependent dielectric and impedance studies

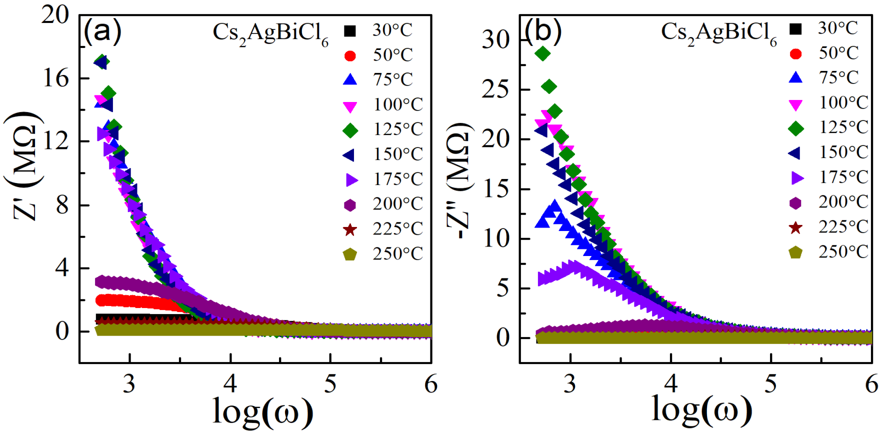

Figure 4.10: Frequency dependent (a) Z'($\omega$), and (b) Z"($\omega$) plot of $Cs_2AgBiCl_6$ HDP at different temperatures.

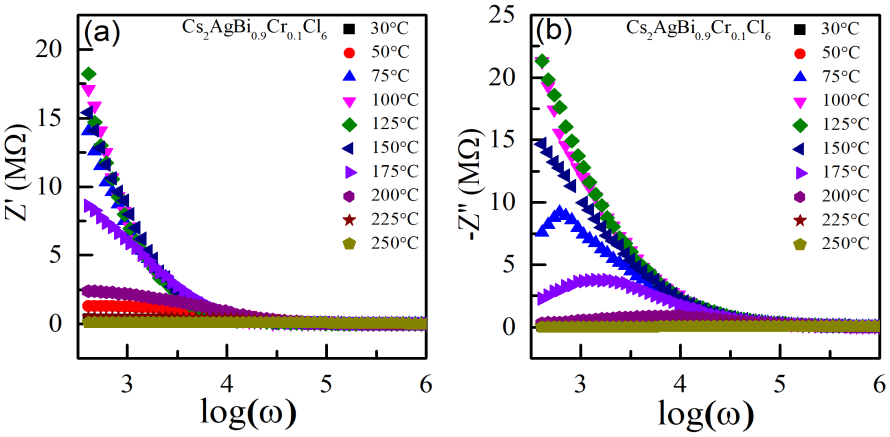

Figure 4.11: Frequency dependent (a) Z'($\omega$), and (b) Z"($\omega$) plot of Cr substituted $Cs_2AgBiCl_6$ HDP at different temperatures.

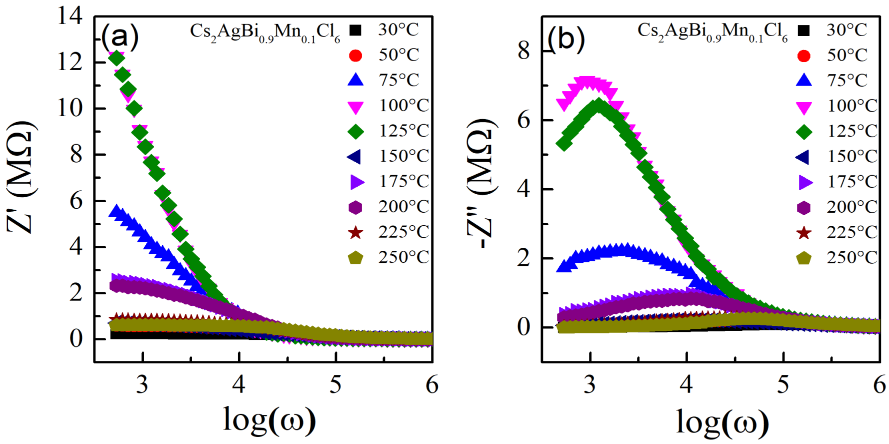

Figure 4.12: Frequency dependent (a) Z'($\omega$), and (b) Z"($\omega$) plot of Mn substituted $Cs_2AgBiCl_6$ HDP at different temperatures.

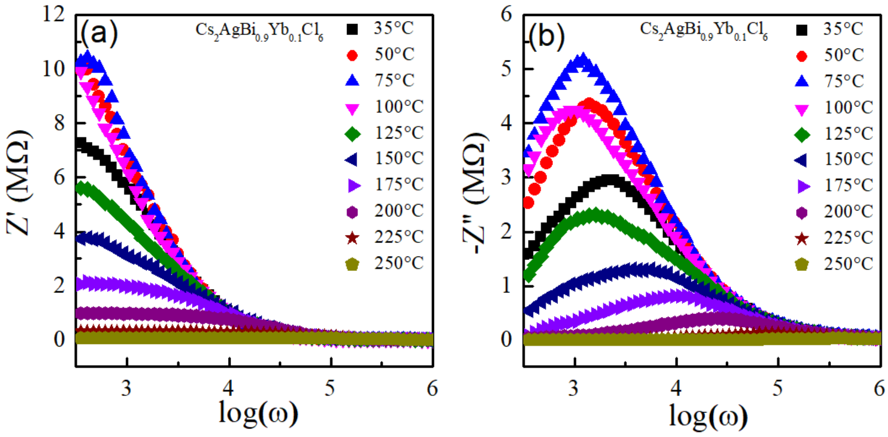

Figure 4.13: Frequency dependent (a) Z'($\omega$), and (b) Z"($\omega$) plot of Yb substituted $Cs_2AgBiCl_6$ HDP at different temperatures.

Understanding the charge conduction mechanism along with the relaxation process varying the temperature springs out interesting results in view of the broad applicability of halide double perovskites in optoelectronic devices. All the studied compositions in the form of circular pellet with silver coating were mounted inside a tightly closed furnace to investigate the effect of temperature on their electrical properties. Figure 4.10-4.17 show the variation of real and imaginary part of impedance as a function of frequency for all the compounds at different temperatures ranging from room temperature to 250 °C in steps of 25 °C. The higher values of real part of impedance (Z'($\omega$)) at lower frequency gradually decreases

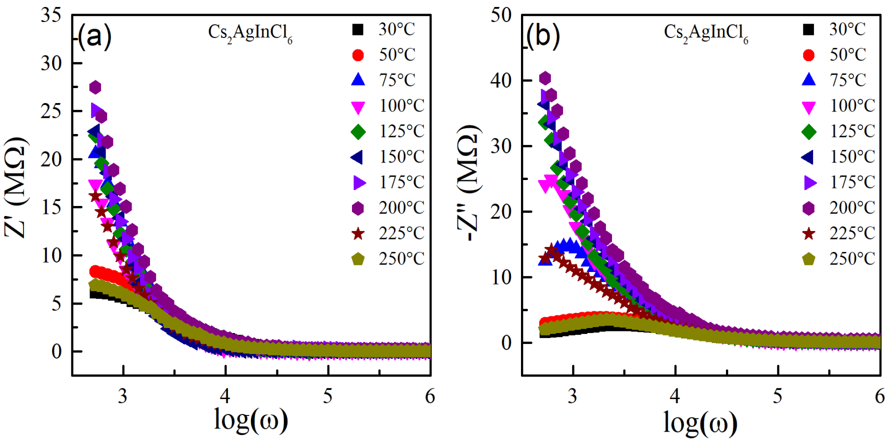

Figure 4.14: Frequency dependent (a) Z'($\omega$), and (b) Z"($\omega$) plot of $Cs_2AgInCl_6$ HDP at different temperatures.

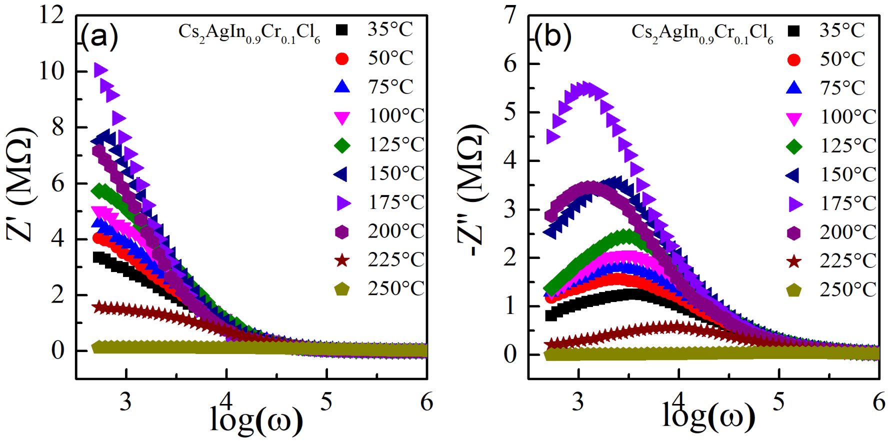

Figure 4.15: Frequency dependent (a) Z'($\omega$), and (b) Z"($\omega$) plot of Cr substituted $Cs_2AgInCl_6$ HDP at different temperatures.

with increase in frequency for all temperatures indicating the release of space charges as well as the decrease of grain boundary and electrode contribution to the total impedance in high frequency region. However, due to the weaker polarization, Z'($\omega$) first increases with increase in temperature showing positive temperature coefficient of resistance (PTCR) behaviour following the decrease in Z'($\omega$) shows the negative temperature coefficient of resistance (NTCR) behaviour which is mainly attributed to the reduction of trapped charge density and increase in charge carrier mobility. The imaginary part of impedance (Z"($\omega$)) also known as loss spectrum shows distinct relaxation peaks at various temperatures. The relaxation peak

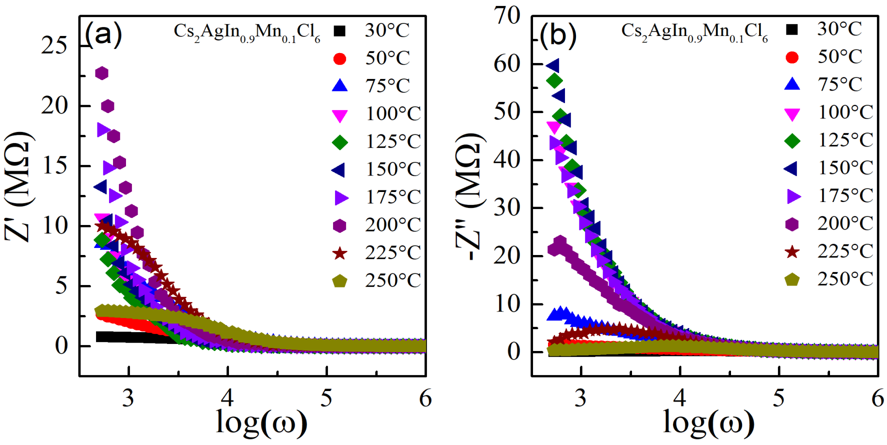

Figure 4.16: Frequency dependent (a) Z'($\omega$), and (b) Z"($\omega$) plot of Mn substituted $Cs_2AgInCl_6$ HDP at different temperatures.

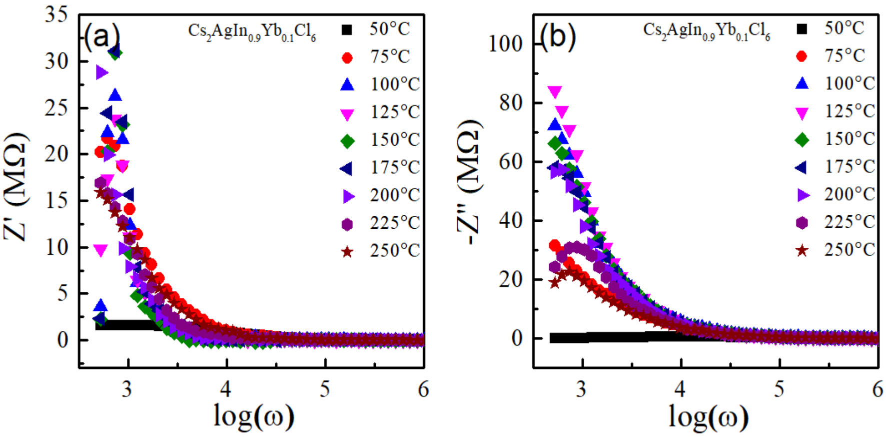

Figure 4.17: Frequency dependent (a) Z'($\omega$), and (b) Z"($\omega$) plot of Yb substituted $Cs_2AgInCl_6$ HDP at different temperatures.

shifting suggests the presence of thermally activated charge carriers in the compounds.

The frequency dependent AC conductivity of the prepared samples are extensively studied to understand the charge conduction mechanism. Generally, the charge carrier conduction is taking place through hopping mechanism where the long range dynamics is established at lower frequency across the grain boundaries and the short range dynamics occur at higher frequency within the local sites or grains [88]. Figure 4.18 and 4.19 represent the variation of AC conductivity as a function of frequency from room temperature to 250°C. The conductivity for all the compounds are calcu-

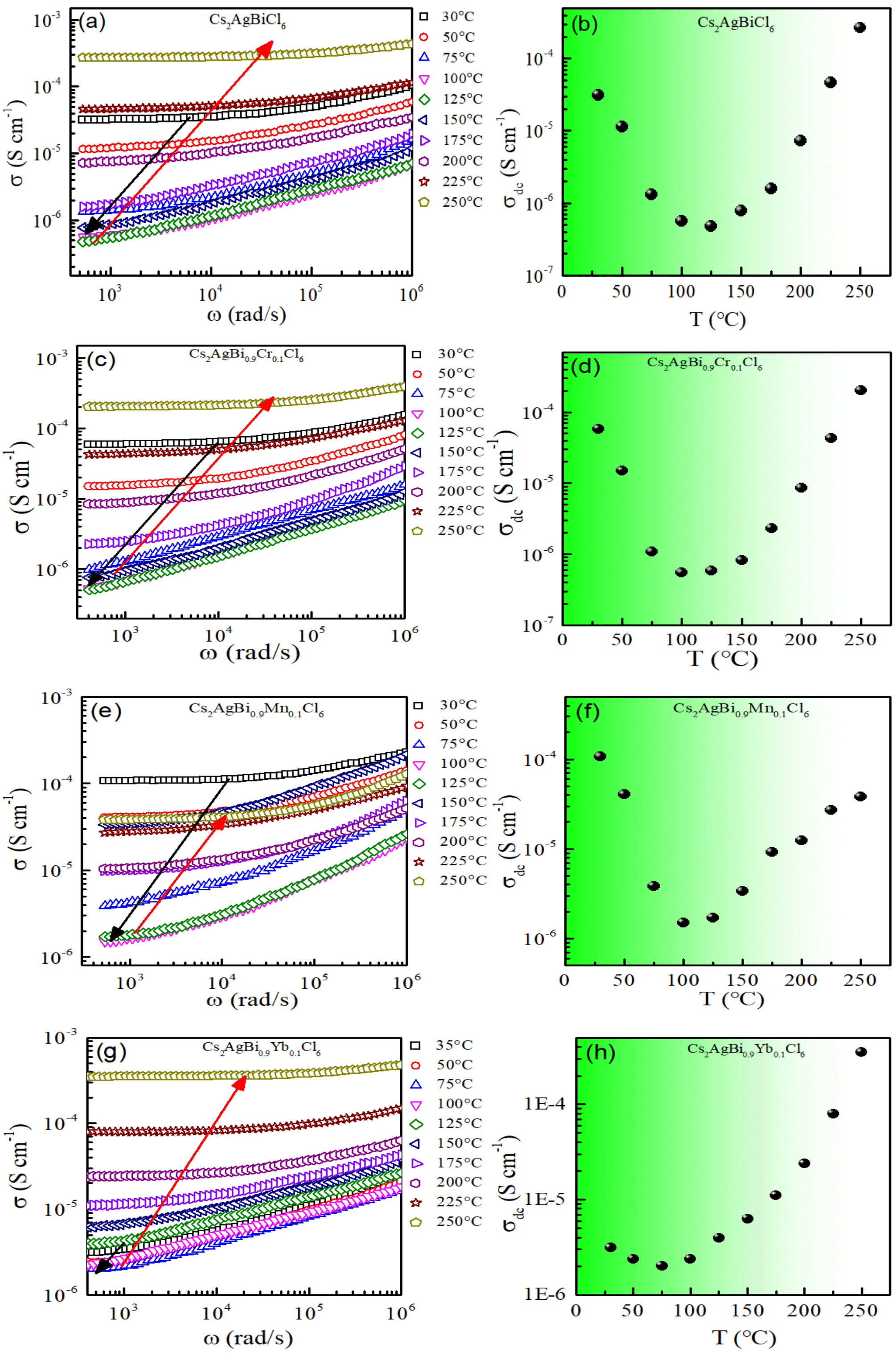

Figure 4.18: (a) Variation of AC conductivity and (b) DC conductivity with temperature for Bi-based compounds. (The black arrow shows the decrease in plateau like behaviour up to the transition temperature followed by the increase in plateau like behaviour with increase in temperature shown by the red arrow.)

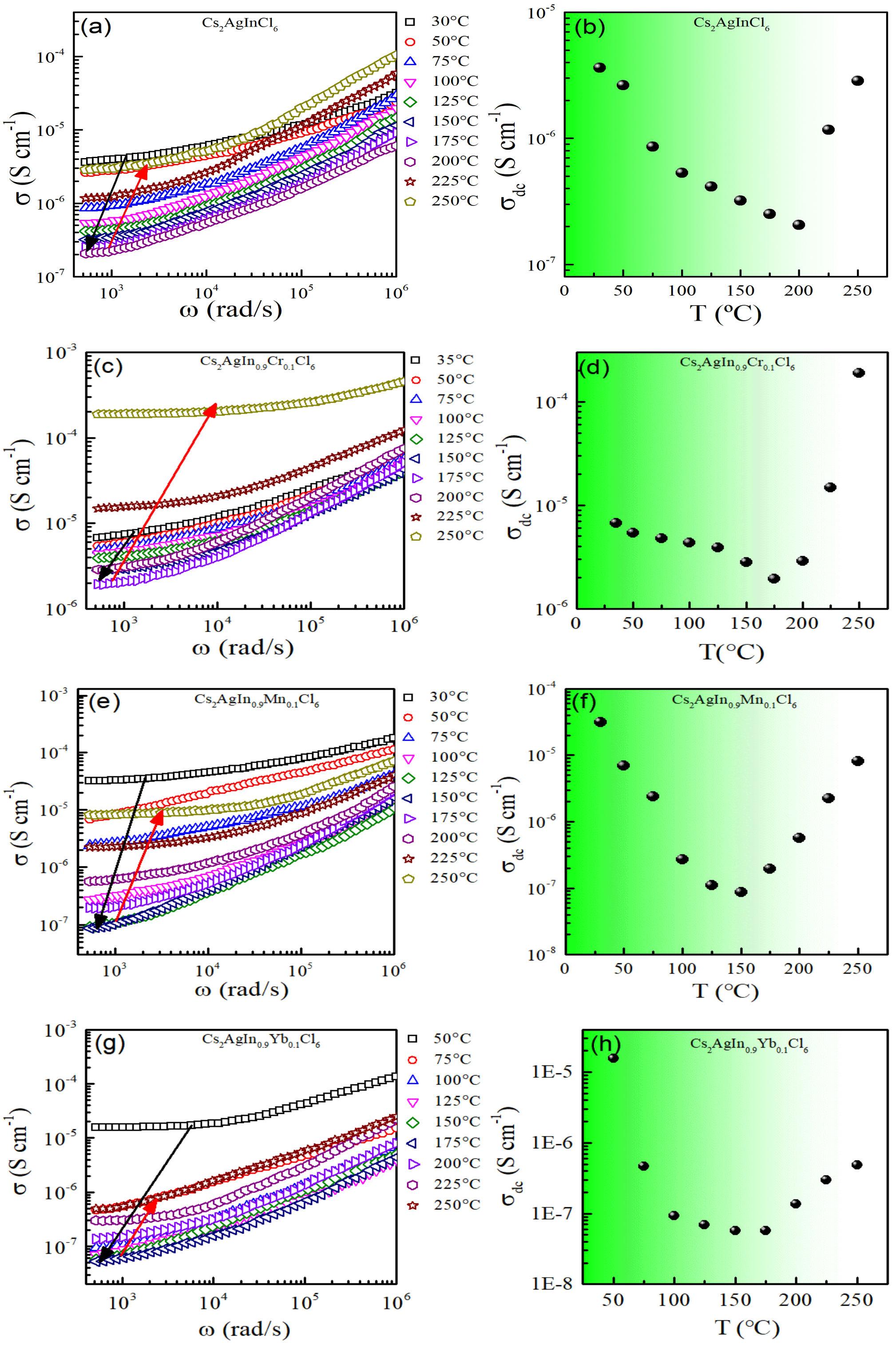

Figure 4.19: (a) Variation of AC conductivity and (b) DC conductivity with temperature for In-based compounds. (The black arrow shows the decrease in plateau like behaviour up to the transition temperature followed by the increase in plateau like behaviour with increase in temperature shown by the red arrow.)

lated from the impedance data at different temperature using the following equation,

$$\sigma(\omega) = \frac{t}{A}\frac{Z'}{(Z'^2 + Z''^2)} \tag{4.2}$$

where, t is the thickness and A is the area of the device.

The dynamics of AC conductivity with change in frequency and temperature can be explained by the Jump Relaxation Model (JRM) [89]. The room temperature AC conductivity showing a plateau-like behaviour can be categorized in two distinct regions; a frequency independent region at low frequency mainly attributed to DC conductivity and a frequency dependent region where the conductivity increases with increase in frequency. According to this model, the low frequency conductivity is mostly caused by successful hopping which suggests the rearrangement of neighbouring ions after an ion hops out of its local configuration to maintain equilibrium in the lattice. This is regulated by the long range translational motion of the ions. While the high frequency region is mostly dominated by forward-backward jumping or unsuccessful hopping where the initial hopping ion reverts to its original position to maintain equilibrium with neighbouring ions linked to short range dynamics. However, the plateau-like feature decreases with increase in temperature indicating the DC conductivity gradually decreases up to the transition temperature and after that at high temperature the plateau-like feature again arises suggesting the long range dynamics are found to be more prominent. Figure 4.18 and 4.19 also represent the variation of dc conductivity with temperature indicating that dc conductivity first decreases and then increases showing two distinct region.

In such scenario, it is imperative to analyse the variation of this kind of impedance as well as the dc conductivity behaviour with temperature. For this we have analysed the temperature effect on dielectric properties of the materials as shown in Figure 4.20 and 4.21. With increase in temperature, the polar molecules start to break apart and the dielectric constant as well as the dielectric loss decreases initially and with further increase in temperature, the molecular vibrations are more energetic causing an increase in dielectric behaviour. The thermal effect of dielectric loss can be

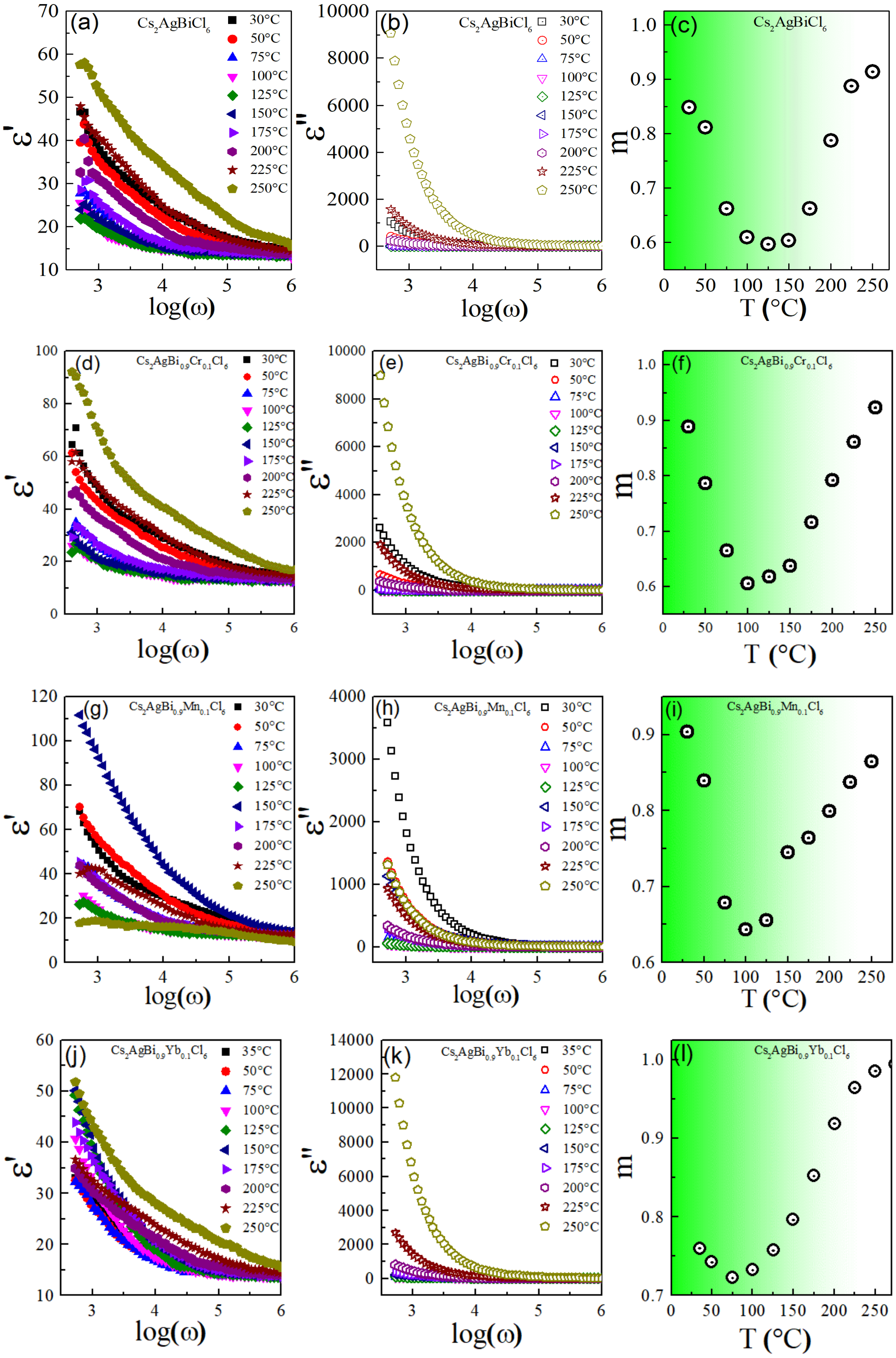

Figure 4.20: Frequency dependent (a) dielectric constant and (b) dielectric loss of Bi-based compounds at different temperatures. (c) Variation of the value of m with temperature calculated using Stevel's model.

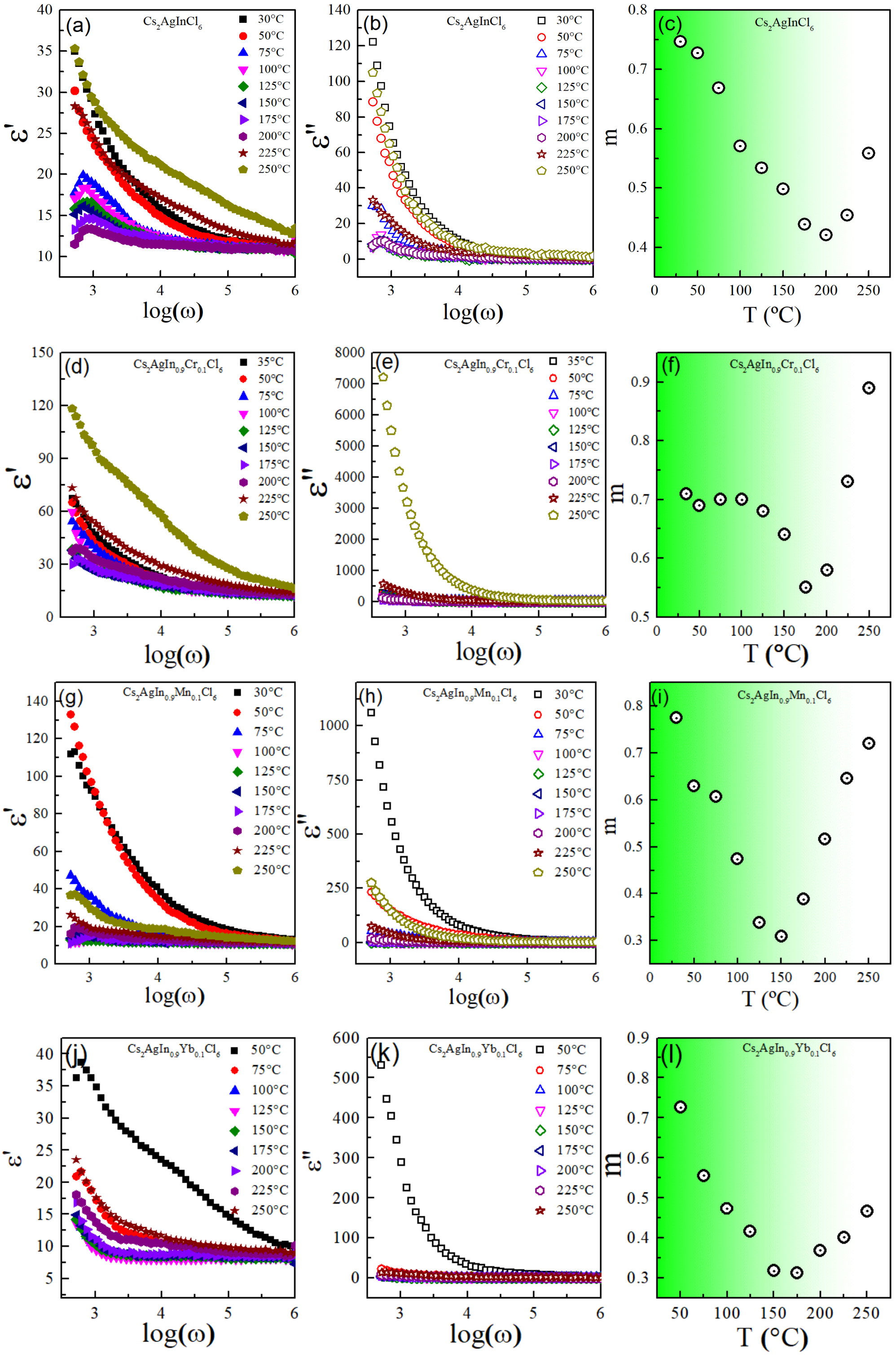

Figure 4.21: Frequency dependent (a) dielectric constant and (b) dielectric loss of In-based compounds at different temperatures. (c) Variation of the value of m with temperature calculated using Stevel's model.

explained by the Stevels' model [90], which defines the loss occur during the relaxation process to be the combined effect of conduction, dipole and vibrational loss and can be collectively expressed by the following equation;

$$\epsilon'' = A\omega^m (m < 0) \tag{4.3}$$

where, m=-4$K_B$T/$H_{max}$. $H_{max}$ represents the maximum barrier height between two traps. As presented in Figure 4.20 and 4.21, the value of m first decreases in region-I (below the transition temperature) indicating the maximum barrier height increases with increase in temperature, which results in increase in the total impedance of the material showing the PTCR type of behaviour. In region-II (above the transition temperature), the value of m increases causing the reduction of barrier height which facilitates the charge carrier conduction across the grain boundary and this results in an NTCR type of behaviour as found in the temperature dependence impedance curve.

Moreover, the relaxation mechanism in these compounds can be well understood by the in-depth analysis of complex electric modulus spectra. The complex modulus spectra is directly associated with the electrical permittivity by the following relation;

$$\begin{aligned} M^*(\omega) = \frac{1}{\epsilon^*(\omega)} = \frac{1}{\epsilon' - j\epsilon''} &= \frac{\epsilon'}{\epsilon'^2 + \epsilon''^2} + j\frac{\epsilon''}{\epsilon'^2 + \epsilon''^2} \\ &= M'(\omega) + jM''(\omega) \end{aligned} \tag{4.4}$$

where, $M'(\omega)$ and $M''(\omega)$ represents the real and imaginary part of electric modulus respectively plotted in Figure 4.22 and 4.23 as a function of frequency starting from room temperature to 250 °C. Initially the value of $M'(\omega)$ is very small at low frequency for all temperatures following by the gradual increase in modulus with increase in frequency forming a plateau-like behaviour at high frequency. While the imaginary part of modulus ($M''(\omega)$) shows distinct peaks for all temperatures corresponding to the relaxation frequency of the material. Interestingly, both the modulus curve show red shift upto the transition temperature followed by the blue shift at high temperature indicating the transition of charge carrier hopping.

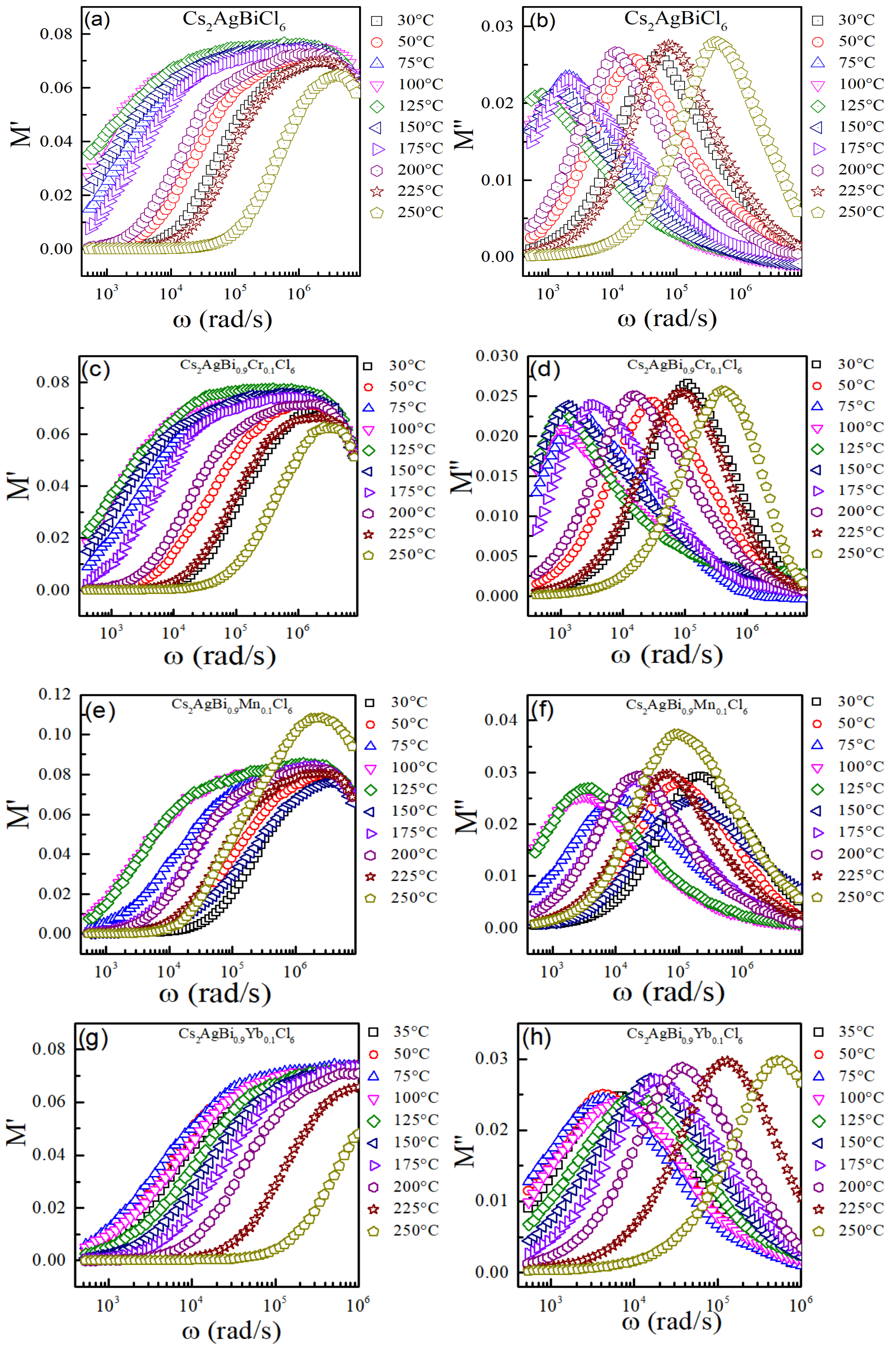

Figure 4.22: Frequency dependence of electrical modulus spectra of Bi-based compounds: (a) M'($\omega$) and (b) M"($\omega$) at different temperatures.

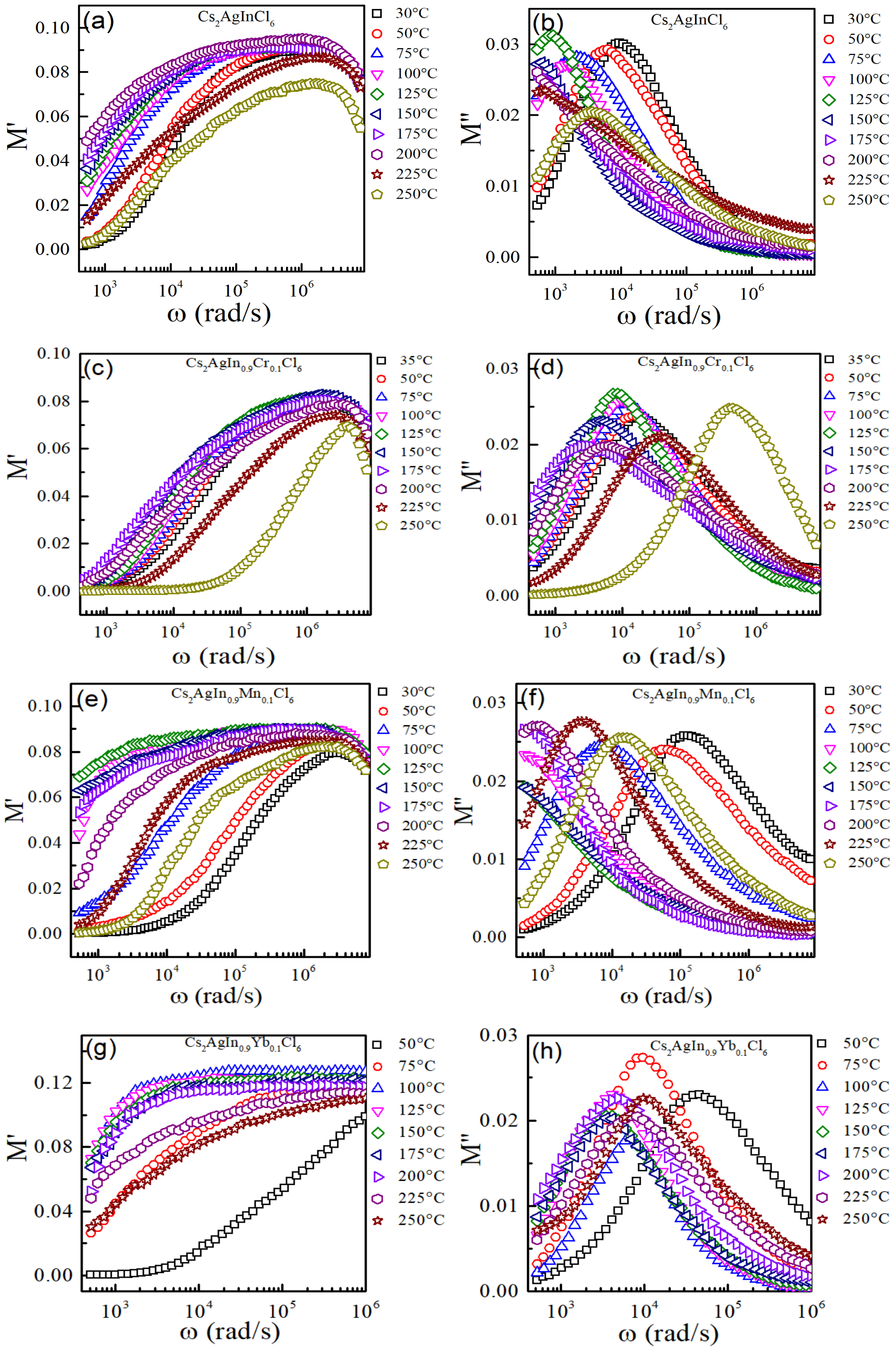

Figure 4.23: Frequency dependence of electrical modulus spectra of In-based compounds: (a) M'($\omega$) and (b) M"($\omega$) at different temperatures.

The low frequency region in $M''(\omega)$ spectra which is below the relaxation frequency explains the hopping of charge through a long range distance, whereas the region above the relaxation frequency represents the hopping of charge carriers through short range distance. Further, the asymmetric nature of the relaxation peaks is a direct indication of non-localized or non-Debye type relaxation mechanism in these systems, where the relaxation process is mediated by ionic or electronic conduction. Further, the temperature induced transition observed in the impedance, conductivity and dielectric properties also found in all the studied compositions. However, the transition temperature is purely material dependent and decreases with Cr, Mn and Yb substitution, which is favourable for various optoelectronic applications.

## 4.7 Raman analysis

Raman scattering, which observe microscopic molecular dynamics through the change in polarizability provides a complementary information on intra- and intermolecular vibrations. Raman spectra were obtained for all the studied compositions in the temperature range of 25 °C to 250 °C to check the thermal impact of vibrational motion on dielectric relaxation process and impedance characteristics. All the compounds show four Raman active modes considering the $\mathrm{Fm\bar{3}m}$ space group symmetry with the irreducible representation: $\Gamma = 2\mathrm{T}_{2g} + \mathrm{E}_g + \mathrm{A}_{1g}$. The temperature dependence anharmonicity is clearly seen in the peak shifting of Raman active modes. Figure 4.24-4.31 show the temperature dependent Raman spectra of all the studied compositions.

Since, the substitution of Cr, Mn and Yb is carried out at Bi or In site of $Cs_2AgBiCl_6$ and $Cs_2AgInCl_6$ respectively, it is necessary to focus on the Bi/In-Cl bond vibration with temperature. Among these Raman active modes, the $\mathrm{E}_g$ mode arises due to the asymmetric stretching of Bi/In-Cl bond, which shows a red shift throughout the temperature range with two different slopes in the two separate region as shown in Figure 4.24(b)-

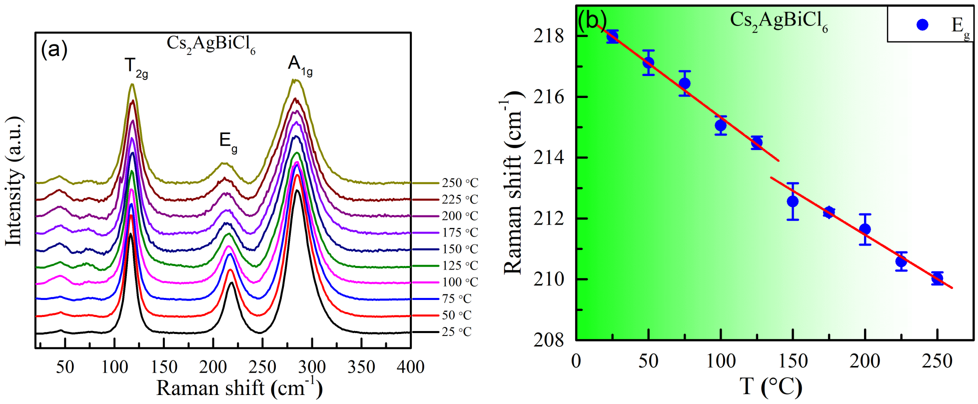

Figure 4.24: (a) Temperature dependent Raman spectra of Cs$_2$AgBiCl$_6$ compound and (b) Raman shift of E$_g$ mode with temperature.

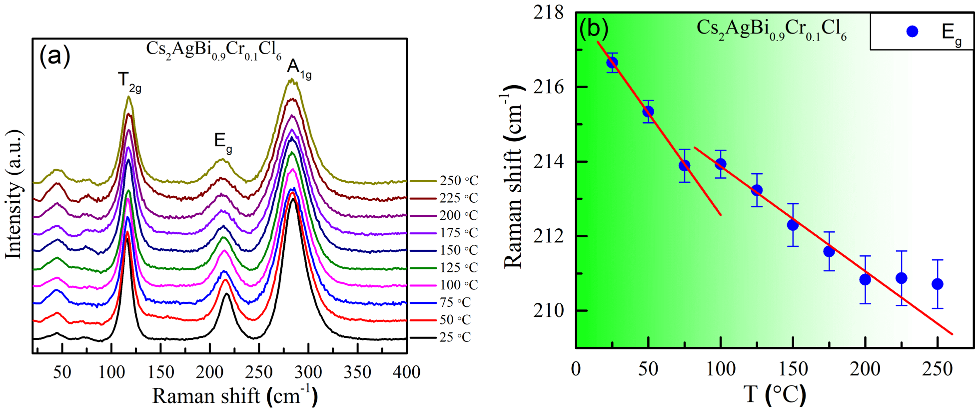

Figure 4.25: (a) Temperature dependent Raman spectra of Cr substituted Cs$_2$AgBiCl$_6$ compound and (b) Raman shift of E$_g$ mode with temperature.

4.31(b). Interestingly, the transition temperature found in the phonon mode shifting coincides with the transition temperature observed in the dielectric and impedance properties of these perovskites. The temperature dependent dielectric behaviour can be understood by the thermal motion of ions as well as the inter-atomic restoring force. The bond weakening with temperature leads to more degrees of freedom in rotational motion of ions which causes local structural deformation in the inorganic octahedral framework, consequently, the bond strength asymmetry results in more polarization that affects the dielectric properties of the materials. This clearly indicates the mutual dependency of charge relaxation and conduction with the local lattice distortion.

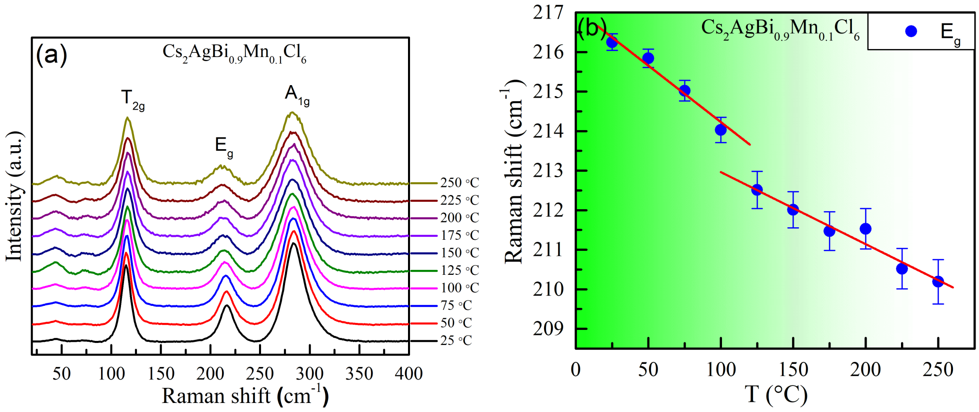

Figure 4.26: (a) Temperature dependent Raman spectra of Mn substituted $Cs_2AgBiCl_6$ compound and (b) Raman shift of $E_g$ mode with temperature.

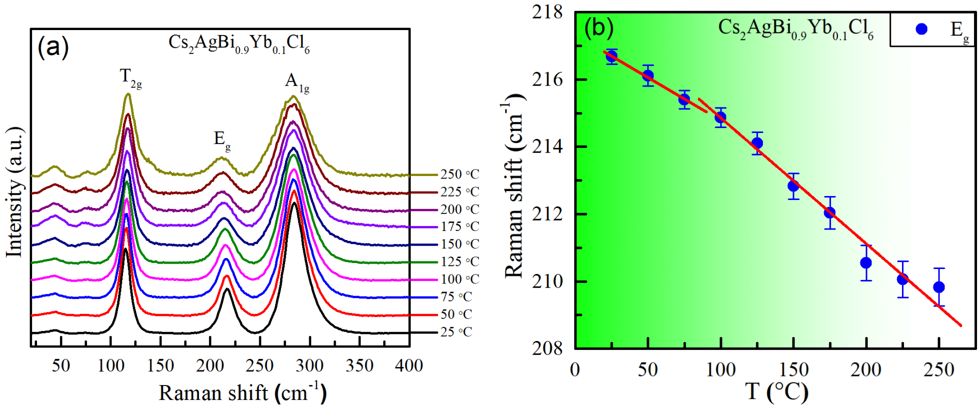

Figure 4.27: (a) Temperature dependent Raman spectra of Yb substituted $Cs_2AgBiCl_6$ compound and (b) Raman shift of $E_g$ mode with temperature.

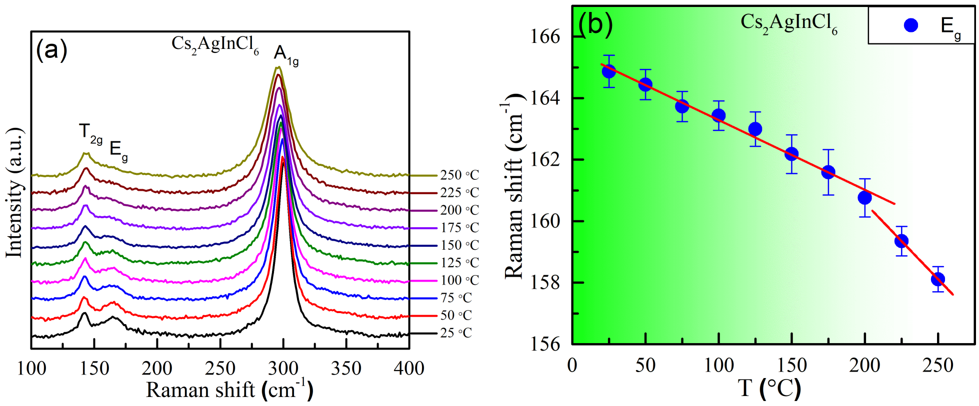

Figure 4.28: (a) Temperature dependent Raman spectra of $Cs_2AgInCl_6$ compound and (b) Raman shift of $E_g$ mode with temperature.

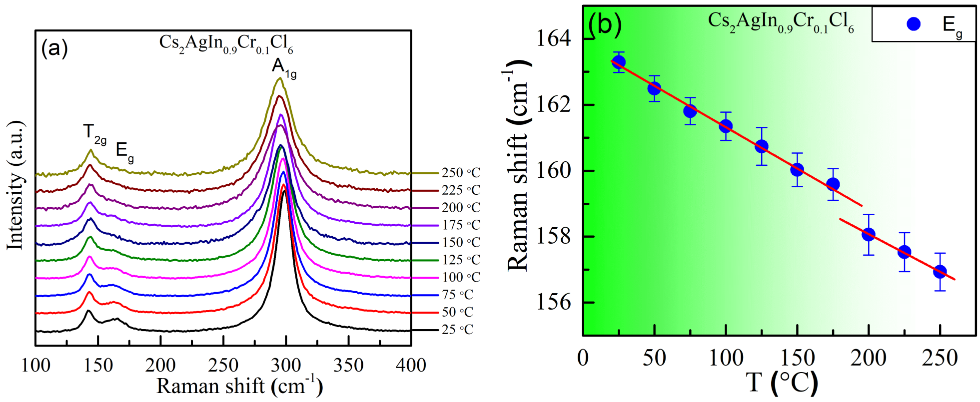

Figure 4.29: (a) Temperature dependent Raman spectra of Cr substituted $Cs_2AgInCl_6$ compound and (b) Raman shift of $E_g$ mode with temperature.

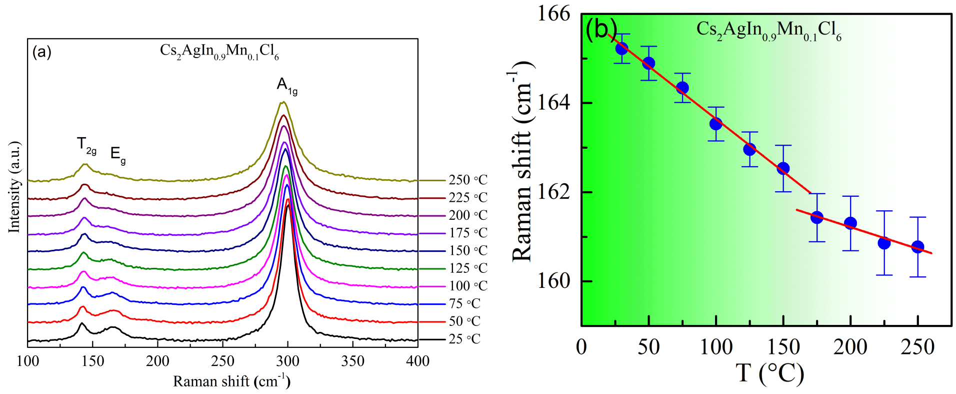

Figure 4.30: (a) Temperature dependent Raman spectra of Mn substituted $Cs_2AgInCl_6$ compound and (b) Raman shift of $E_g$ mode with temperature.

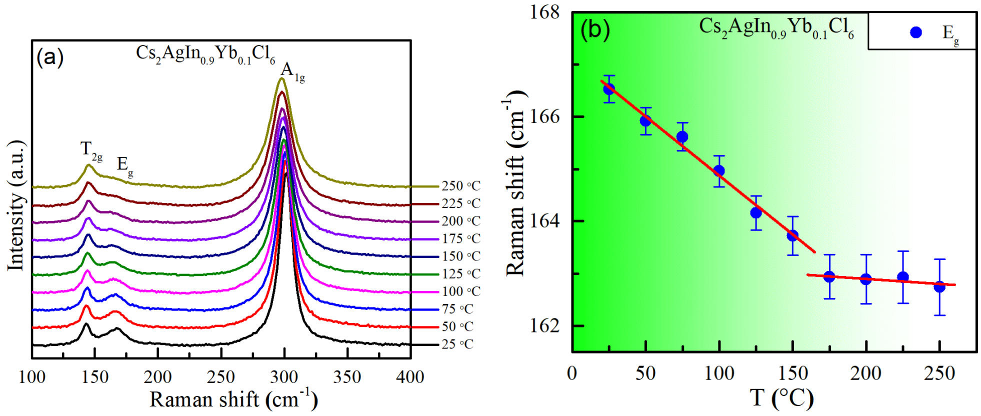

Figure 4.31: (a) Temperature dependent Raman spectra of Yb substituted $Cs_2AgInCl_6$ compound and (b) Raman shift of $E_g$ mode with temperature.

## 4.8 Photoresponse Application

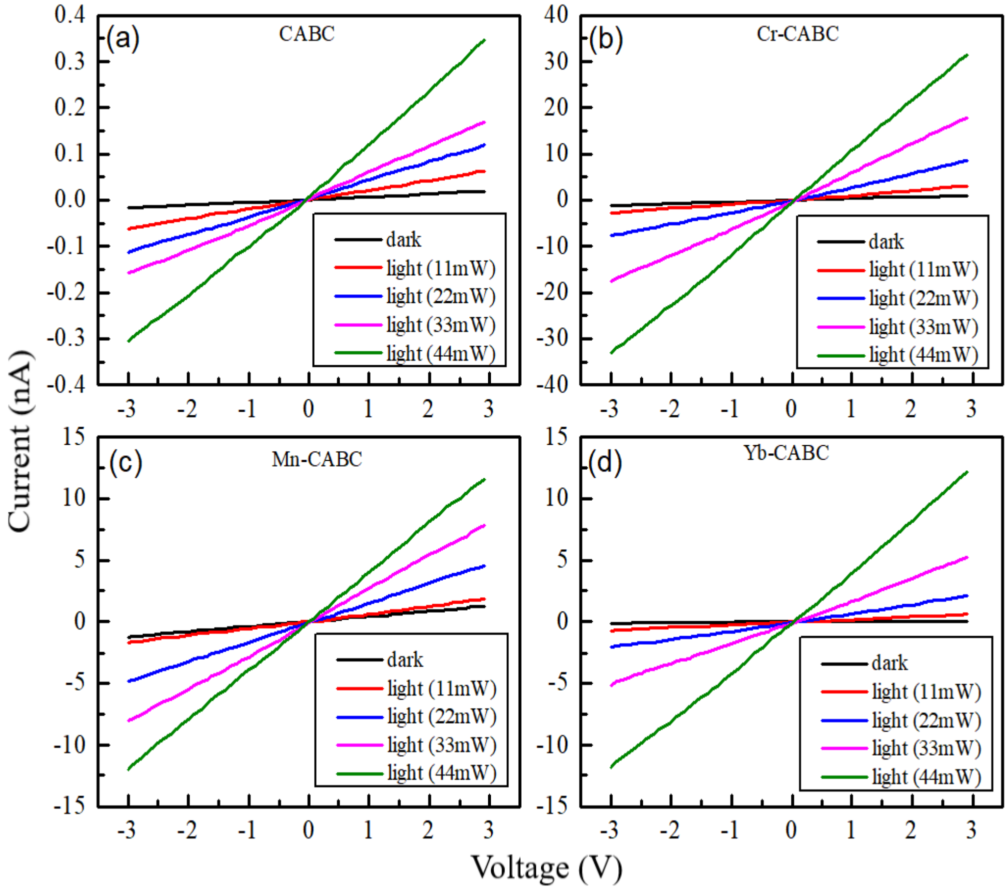

Figure 4.32: I-V characteristics of Bi-based HDPs. The data was recorded under dark and, varying light intensity conditions.

The room temperature I-V (current-voltage) characteristics of these compositions were recorded under varying light intensities. Figure 4.32 and 4.33 depict the photo-current behaviour of all the compositions, recorded under 450 nm illumination and with light intensity varying from dark to 44 mW/cm$^2$. The dark current (I$_d$) comparatively increases in substituted compounds, which is an advantage for the photodetector application. Increase in light intensity leads to generation of light-activated electron-hole pairs, which in turn leads to dramatic increase in the photo-current, at both forward and reverse biased conditions. The increase in photo-current as a function of incident light intensity can be described by a power law accord-

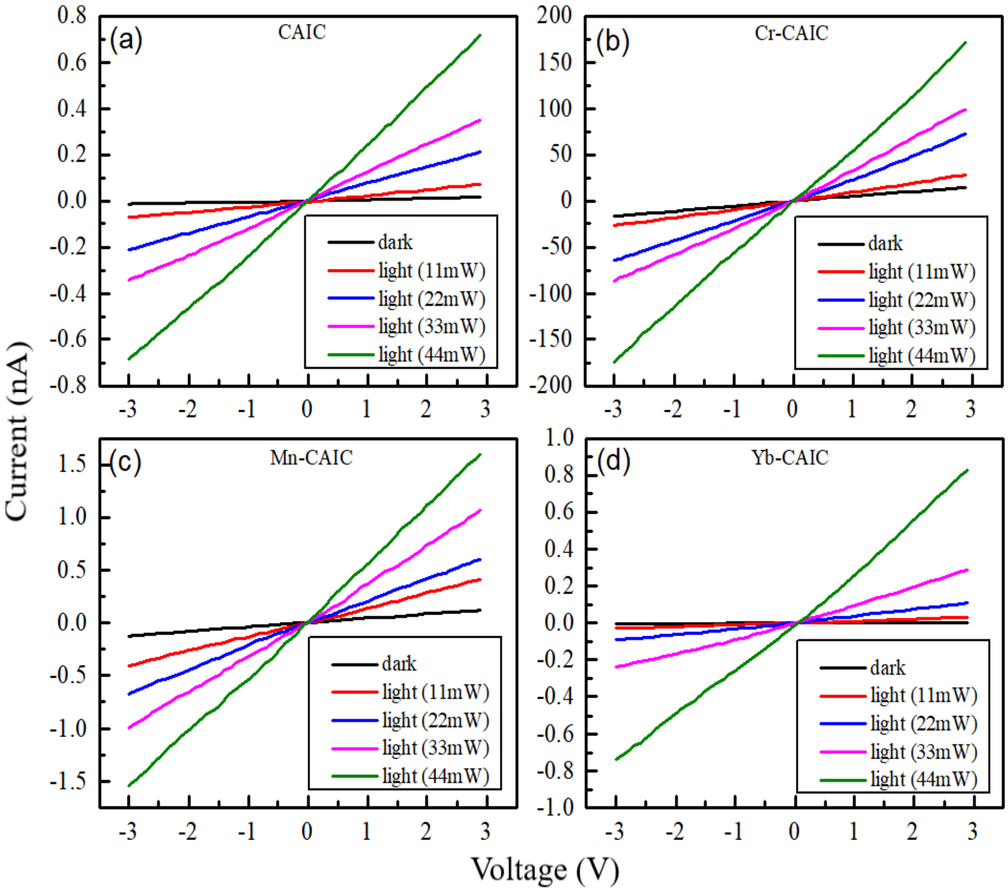

Figure 4.33: I-V characteristics of In-based HDPs. The data was recorded under dark and, varying light intensity conditions.

ing to the equation $I \propto P^{\gamma}$. The exponent $\gamma$ depends on the electron-hole generation, trapping and recombination process of charge carriers. For the most ideal case, the linear behaviour of photo-current with incident power ($\gamma = 1$) is solely because of the generation electron-hole pairs. However, in our case of studies, the superlinear power dependence ($\gamma > 1$) of photo-current is observed which is due to the photo-thermionic effect. The superlinear behaviour of photo-current with illumination power as depicted from Figure 4.34 and 4.35 indicates the higher optoelectronic efficiency in the substituted compositions, which favours in various optoelectronic applications.

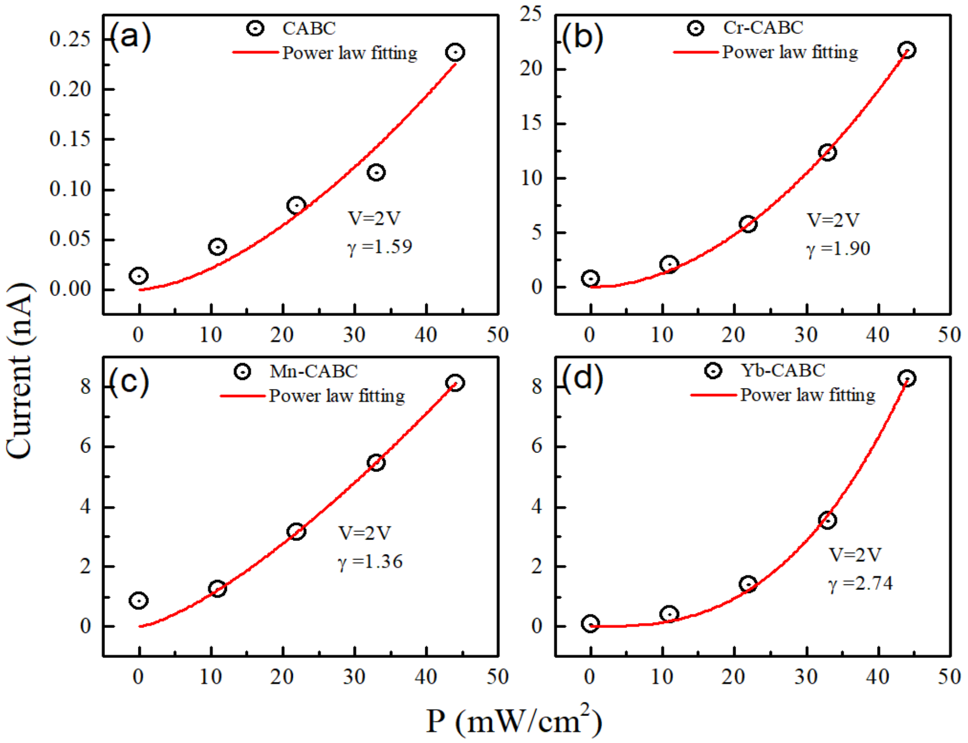

Figure 4.34: Power law dependence of the photocurrent for Bi-based HDPs.

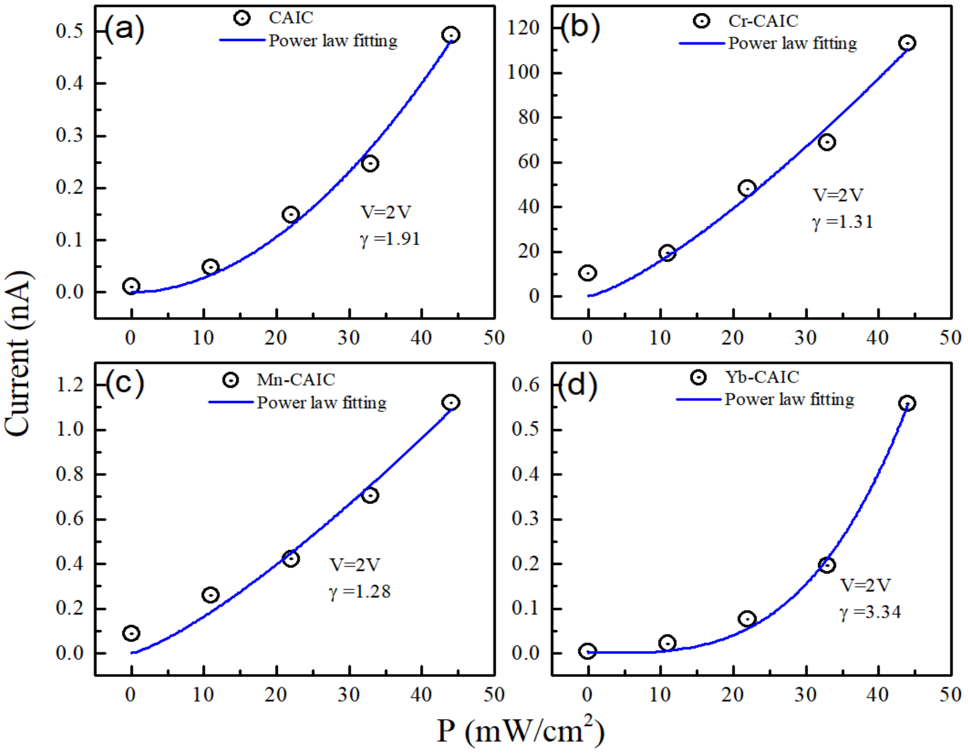

Figure 4.35: Power law dependence of the photocurrent for In-based HDPs.

## 4.9 Summary

A subsequent understanding of the optical properties and the charge conduction mechanism of these materials has developed probing the photoluminescence and complex impedance and dielectric study respectively. Introducing transition metal into the halide double perovskites significantly affect the electrical properties of the materials and increases the conductivity. The impedance measurements for all samples revealed a transition from PTCR to NTCR behavior. This transition correlated directly with the local environment of the dipoles as resulted from Raman spectra. It was found that the dielectric properties of the materials were significantly influenced by the rotational and vibrational motion of ions and this influence was evident in the temperature-dependent shifting of Raman active modes. Besides, our work sheds light on the photoresponse behaviour of these halide perovskites which shows the superlinear photocurrent and are hence suitable for photodetector application. Thus, dissecting the structural and electrical properties of these materials suggests their potential application in various optoelectronic fields.

# Chapter 5

# Thermochromism in single crystalline $Cs_2NaFeCl_6$ halide double perovskite

## 5.1 Overview

One fascinating phenomenon observed in certain compounds is the temperature-induced colour change, known as thermochromism. This property holds significant potential for applications in smart windows, temperature sensors, virtual thermometers, display devices, and more [91–93]. Recently, various halide perovskites such as $MAPbI_{3-x}Br_x$ [94], $Cs_3Sb_2I_9$ [95], $Cs_2AgBiBr_6$ [39], $Cs_2AgBiCl_6$ [96] and $(CH_3NH_3)_4PbI_6{\cdot}2H_2O$ [97] have exhibited thermochromic properties. 2D-layered perovskites, such as $Cs_3Bi_2Br_9$ and $MA_3Bi_2Br_9$, undergo more pronounced band gap shifts and thermal expansion than their 3D counterparts, $Cs_2AgBiCl_6$ and $Cs_2AgBiBr_6$. This behavior arises from the increased structural flexibility and additional space within the lattice. The changes in band gap and associated color variations result from a complex synergy between thermal expansion and electron-phonon interactions, highlighting the dynamic nature of these materials under varying thermal conditions. First-principles calculations reveal that local disorder and anharmonicity result in strongly coupled phonons, which indirectly contribute to the smooth evolution of the band gap. The alterations in band structure with temperature are primarily due to thermal expansion driven by anharmonicity in the crystal potential and electron-phonon coupling, which arise from Debye-Waller and self-energy corrections [98, 99]. The substantial coupling between electrons and phonons is expected to induce lattice distortions, perturbing the crystal potential experienced by the charge carriers. This perturbation results in polaronic effects, spectral line broadening, enhanced emission intensity, and influences the optoelectronic properties [100–102]. In halide perovskites, such effects are significantly influenced by the B-site cations within the lattice [103, 104]. A recently developed Fe-based halide double perovskite (HDP), $Cs_2NaFeCl_6$, exhibits remarkable and reversible thermochromism [105]. Compared to other thermochromic materials such as hybrid perovskites, $Cs_2NaFeCl_6$ stands out as one of the most stable double perovskites, promoting its potential for practical applications. However, the underlying mechanism of its dramatic colour change is not yet thoroughly understood. A deeper comprehension of the structure-property correlation and the dynamic mechanisms in this lead-free HDP will be crucial for advancing the design of next-generation optoelectronic devices [106].

## 5.2 Structural characterization

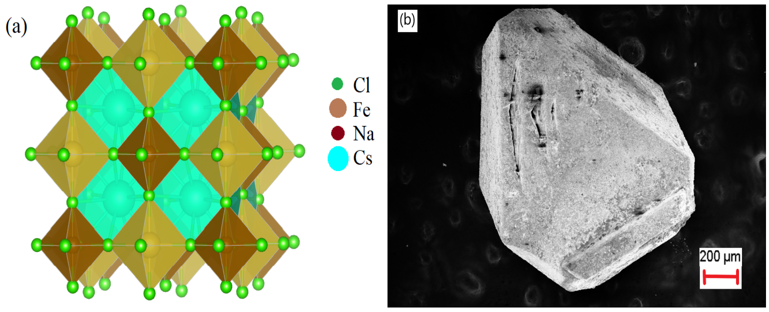

Figure 5.1: (a) FESEM image of synthesized $Cs_2NaFeCl_6$ single crystal, and (b) Crystal structure of $Cs_2NaFeCl_6$ compound showing the octahedral arrangement of $[NaCl_6]^{5-}$ and $[FeCl_6]^{3-}$ octahedra.

Single crystal X-ray diffraction (SCXRD) suggests the formation of phase pure $Cs_2NaFeCl_6$ halide double perovskite having Fm$\bar{3}$m space group symmetry with a lattice constant of 10.33 Å. The cubic structure consists of alternately arranged $[NaCl_6]^{5-}$ and $[FeCl_6]^{3-}$ octahedra and the monovalent Cs cations are embedded at the centre of the octahedral cavity, as shown in Figure 5.1(a). The detailed structural information extracted from the SCXRD measurement is provided in Table 5.1. The morphology of single crystal of the synthesized $Cs_2NaFeCl_6$ is shown in Figure 5.1(b) which exhibits a truncated octahedron geometry. The analysis of EDX data indicates the presence of nominal concentrations of Cs (19.38 at.%), Na (11.63 at.%), Fe (10.03 at.%) and Cl (58.96 at.%) in the compound, matches well with its chemical stoichiometry.

| Compound | $Cs_2NaFeCl_6$ |
|---|---|
| Formula weight | 557.36 g/mol |
| Temperature | 296.15 K |
| Crystal color | Orange |
| Crystal system | Cubic |
| Space group | Fm$\bar{3}$m |
| a=b=c (Å) | 10.34(1) |
| $\alpha$=$\beta$=$\gamma$ | 90° |
| Volume (Å$^3$) | 1106.0(2) |
| Z | 2 |
| Source | Mo-K ($\lambda$=0.71073 Å) |
| $\theta$ range for data collection | 3.41°-28.03° |
| Index range | -9<h<13, -12<k<12, -11<l<13 |
| Reflections collected | 1012 |
| Goodness of fit | 1.407 |
| R index | $R_1$=1.09%, $wR_2$=2.73% |

Table 5.1: Parameters obtained from single crystal X-ray diffraction data of $Cs_2NaFeCl_6$ compound.

Figure 5.2 depicts the optical micrographs of the single crystal showing the colour change upon temperature rise. The tiny bright-red coloured crystals exhibit significant colour evolution as a function of temperature, ranging from pale-yellow at ∼98 K to dark-brown at ∼473 K. Notably, this transition is completely reversible and consistent over several cycles of heating and cooling process.

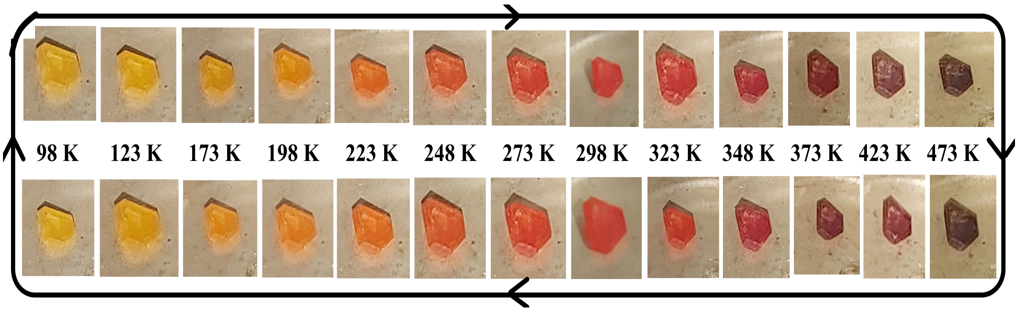

Figure 5.2: The reversible thermochromism shows by the single crystal with the variation of temperature from 98 K to 473 K.

## 5.3 Stability

To know the thermodynamic stability of the compound, thermogravimetry analysis (TGA) measurement was carried out showing a good thermal stability over a wide range of temperature up to 700K as shown in Figure 5.3.

Again, to check the stability of the compound over several thermal cycle, we recorded XRD spectra of the compound. Figure 5.4 represents such profiles recorded at room temperature after 25 and 50 thermal cycles. It is evident that the XRD patterns remain intact indicating the crystal structure remains unchanged. In addition, this double perovskite shows excellent stability over several cycles of heating and cooling as confirmed from the room temperature Raman spectra and UV-vis diffuse reflectance spectra as shown in Figure 5.5. There is no significant change in the peak position of various Raman modes at room temperature after repeated thermal cycles and the reflectance spectra also remains unaltered at each cycle suggesting its higher stability.

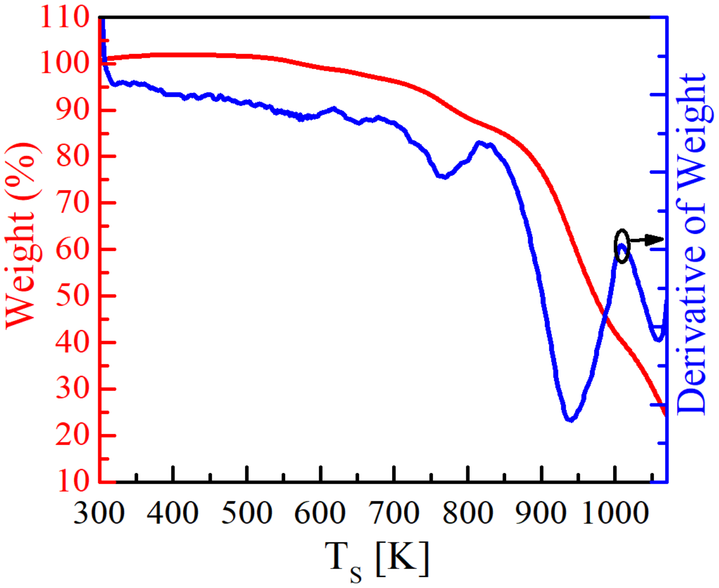

Figure 5.3: Thermogravimetry analysis (TGA) data of the HDP showing its thermal stability (the red line shows the weight(%) and blue line shows the derivative of weight with temperature).

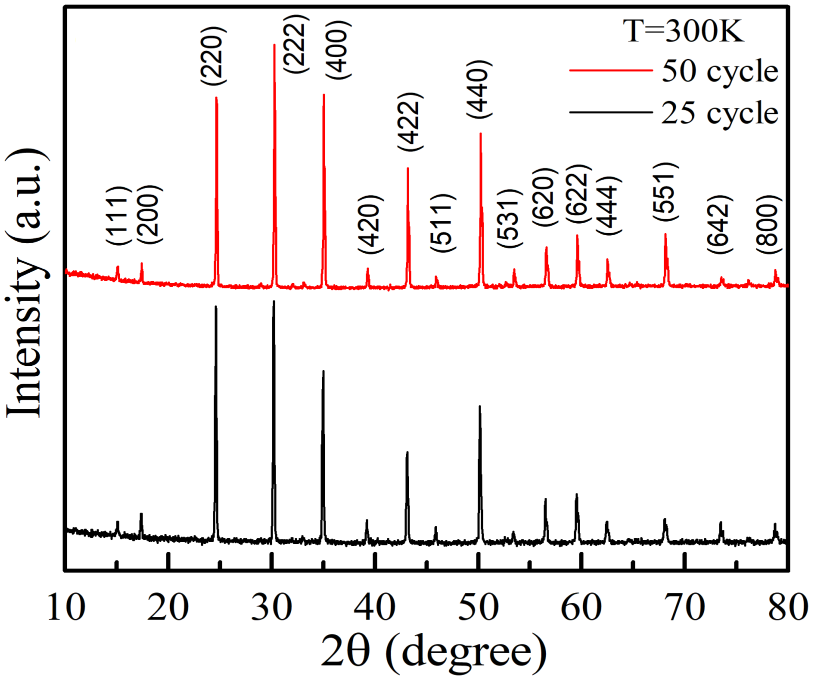

Figure 5.4: Room temperature X-ray diffraction profiles after several thermal cycles.

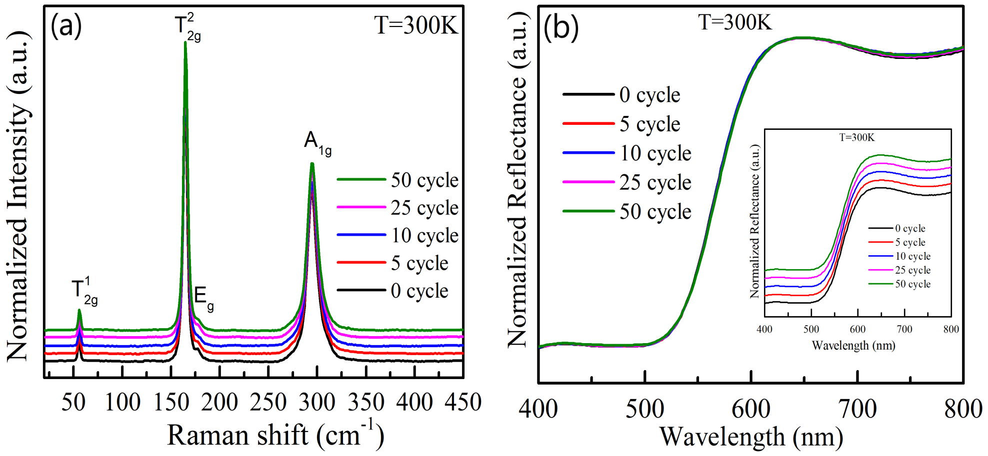

Figure 5.5: (a) Room temperature Raman spectra after several thermal cycles, and (b) room temperature UV-vis diffuse reflectance spectra with different thermal cycles (A clear distinguished images of reflectance spectra with different background is presented in the inset figure).

## 5.4 Temperature dependent XRD study

In general, the change in crystal potential with temperature may induce structural transition in a compound and also affect the electronic arrangement of the crystal. This leads to various optoelectronic properties showed by different halide perovskites. Therefore, to investigate the possibility of any crystallographic phase transition to be the reason for the observed thermochromism in $Cs_2NaFeCl_6$, we carried out temperature dependent X-ray diffraction. Figure 5.6 shows the XRD profiles of the finely powdered crystals, recorded at various temperatures ranging from 100 K to 350 K. Apart from the gradual shift in all the peak positions towards a lower value of $2\theta$ that occurs as a result of thermal expansion of the unit cell, the crystal symmetry remains unaltered in the entire temperature range. The possibility of crystallographic transition is thus ruled out. Profile fitting of the powder XRD data carried out through Rietveld refinement method yields the unit cell parameters and the temperature variation of unit cell parameters is given in Table 5.2. The unit cell dimensions change from 10.29 Å at 100 K to 10.35 Å at 350 K.

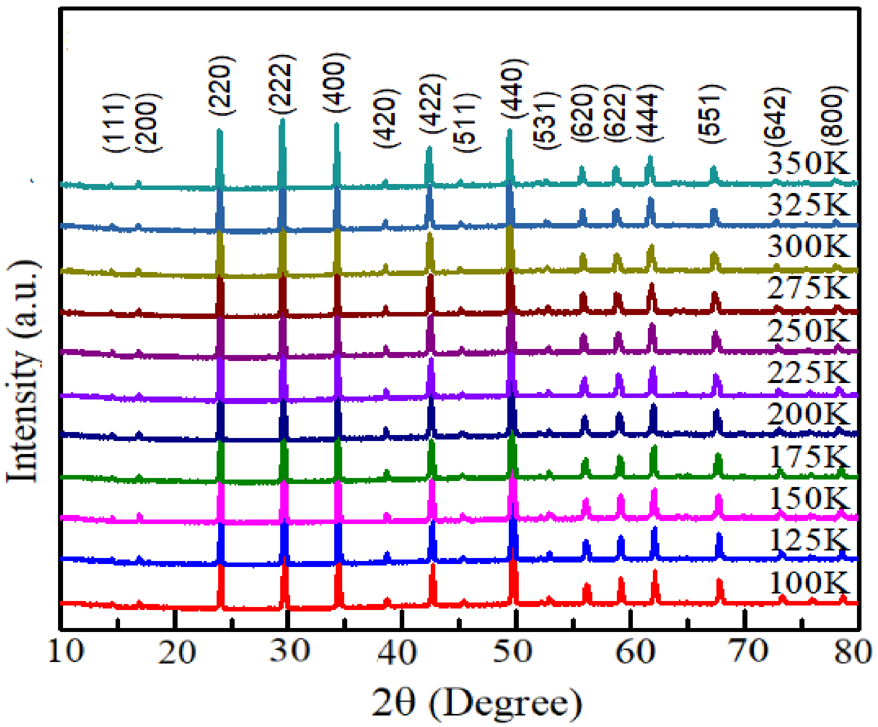

Figure 5.6: Temperature dependent XRD profiles of $Cs_2NaFeCl_6$ compound.

| Temperature (K) | Lattice constant (Å) | Volume (Å$^3$) | $\chi^2$ | $R_p$ | $R_{wp}$ | $R_{exp}$ |
|---|---|---|---|---|---|---|
| 100 | 10.291(5) | 1089.89(7) | 11.0 | 16.4 | 23.2 | 6.99 |
| 125 | 10.297(5) | 1091.95(7) | 11.1 | 16.3 | 23.2 | 6.99 |
| 150 | 10.303(6) | 1093.76(7) | 10.8 | 16.0 | 22.9 | 6.96 |
| 175 | 10.308(6) | 1095.43(7) | 10.4 | 15.6 | 22.4 | 6.94 |
| 200 | 10.316(4) | 1097.91(7) | 9.67 | 15.1 | 21.5 | 6.93 |
| 225 | 10.322(4) | 1099.80(7) | 9.58 | 14.7 | 21.4 | 6.90 |
| 250 | 10.328(4) | 1101.86(7) | 9.22 | 14.4 | 20.9 | 6.88 |
| 275 | 10.335(3) | 1103.97(7) | 8.57 | 13.8 | 20.1 | 6.86 |
| 300 | 10.340(3) | 1105.79(7) | 8.56 | 13.6 | 20.0 | 6.84 |
| 325 | 10.347(3) | 1107.99(6) | 8.13 | 13.2 | 19.5 | 6.83 |
| 350 | 10.352(3) | 1109.38(6) | 7.74 | 12.5 | 18.9 | 6.81 |

Table 5.2: Table shows the lattice parameter, cell volume and Rietveld refinement fitting parameters of the compound at different temperatures.

## 5.5 Temperature dependent Raman study

To gain more insight into the mechanism leading to thermochromic behaviour of $Cs_2NaFeCl_6$ crystals, we carried out the temperature dependent Raman spectroscopy measurement to probe its local lattice picture. Figure 5.7(a) represents the spectra recorded in the temperature range from 98 K to 448 K using an excitation wavelength of 633 nm. Considering the cubic $Fm\bar{3}m$ space group symmetry, $Cs_2NaFeCl_6$ exhibits four Raman active modes at room temperature, with an irreducible representation of $\Gamma = 2T_{2g} + E_g + A_{1g}$. The low-frequency $T_{2g}^1$ mode corresponds to the translational motion of Cs atoms. The $T_{2g}^2$ mode arises from the breathing vibrations of the $[NaCl_6]^{5-}$ octahedra, while the $E_g$ mode results from the asymmetric vibrations of the $[FeCl6]^{3-}$ octahedra embedded within the lattice. The longitudinal optical (LO) phonon mode ($A_{1g}$), is arising from the symmetric stretching of both Na-Cl and Fe-Cl bonds. Through a detailed Raman analysis, we can better understand how thermal vibrations influence the physical properties of $Cs_2NaFeCl_6$.

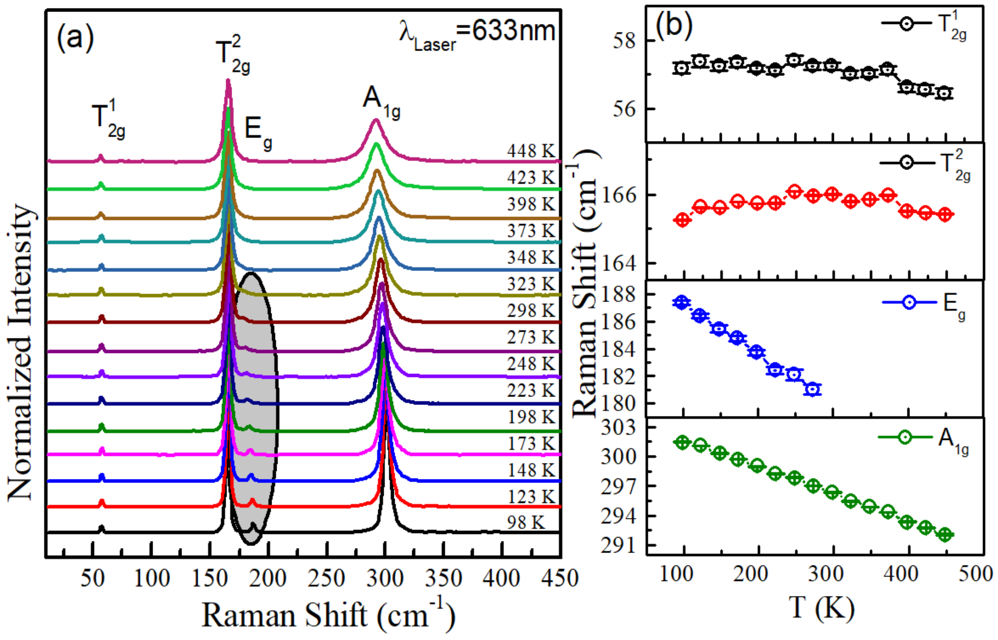

Figure 5.7: (a) Temperature dependence of Raman spectra of $Cs_2NaFeCl_6$ compound starting from 98K to 448K and (b) variation of peak position of all Raman active modes with temperature.

The direct effect of temperature on the single crystal is shown by the variation of Raman peak position of various phonon modes with increase in temperature as shown in Figure 5.7(b). The $T_{2g}^1$ mode showing no significant change in Raman shift indicates that the Coulomb interaction between Cs and Cl atoms remains stable across the temperature range. Similarly, the $T_{2g}^2$ mode displays no Raman shift, suggesting consistent isotropic breathing of $[NaCl_6]^{5-}$ octahedra within the lattice. Notably, the $E_g$ mode exhibits a red shift of approximately 6 $cm^{-1}$ with increase in temperature and merges with the ${T_{2g}}^2$ peak above room temperature. Moreover, a significant shift in the $A_{1g}$ mode is observed, with the peak shifting from 301.5 $cm^{-1}$ at 98 K to 291 $cm^{-1}$ at 448 K. Such anomalies, suggesting a sort of lattice deformation within the lattice influenced by temperature wherein the long range crystallographic symmetry is maintained, but locally the $[NaCl_6]^{5-}$ and $[FeCl_6]^{3-}$ octahedra may be distorted.

## 5.6 Temperature dependent XAFS study

A quantitative analysis of the local crystal structure of the compound can be investigated through an extensive study of X-ray Absorption Fine Structure spectroscopy (XAFS) measurement. Here, the variation of the absorption coefficient with respect to the energy of the incident X-ray photons tuned to the K-shell energy of the Fe atoms is recorded, at different temperatures. The data is extracted after subtracting the isolated atom background from the experimentally obtained absorption spectrum. The $\chi(k)$ spectra in the range of 2 to 12 Å$^{-1}$ were Fourier transformed to $R$-space and a plot of $\chi(R)$ as a function of radial distance from the absorbing atom is obtained, as shown in Figure 5.8(a). From its Fm$\bar{3}$m space group symmetry and the unit cell dimensions obtained from XRD analysis, the local structure around Fe atoms in $Cs_2NaFeCl_6$ can be viewed as having 6 Cl atoms as its nearest neighbours at a distance of a quarter of the lattice constant ($\sim$ 2.57 Å). The next shell around Fe comprises of Cs atoms at a distance of $\sim$ 4.46 Å. The third shell is comprising of Na atoms at half of

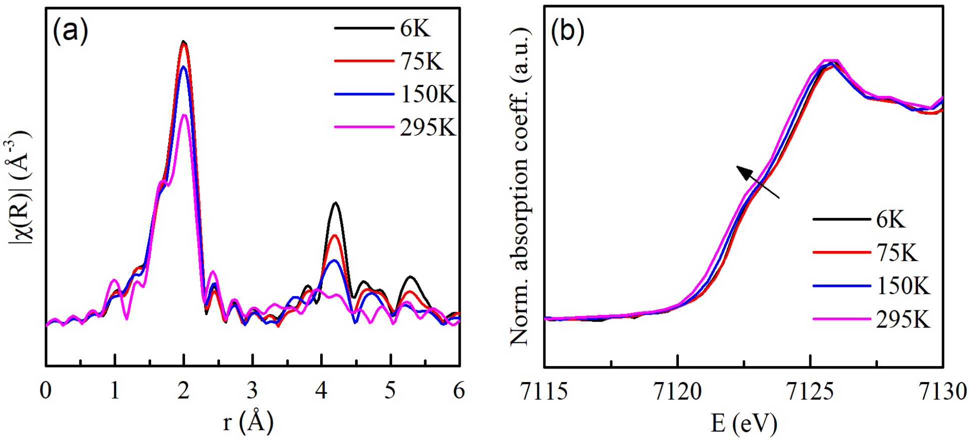

Figure 5.8: (a) $k^2$- weighted Fourier transform spectra of Fe-K edge recorded at different temperatures and (b) XANES spectra of Fe-K edge showing the shifting of absorption edge towards lower energy with increase in temperature.

the lattice constant ($\sim$ 5.13 Å), and an equally strong contribution originating from the Fe-Na-Cl multiple scattering path. We build our structural model with such parameters as the first guess and refine the XAFS spectra until a good fit between the model and data are achieved in the range of 1.0 to 5.0 Å in $R$-space and 2 to 12 Å$^{-1}$ in $k$-space. The final fits to the data are presented in Figure 5.9 and the extracted parameters are tabulated at Table 5.3. The notable aspect here is the Fe-Cl bond distance extracted from XAFS data are significantly short in comparison with that calculated from the lattice constant value expected from the XRD data, while the Fe-Cs and Fe-Na bond distances show a good match. Further, the change in temperature has no significant effect on the Fe-Cl bonding and it follows the natural thermal expansion. Interestingly, the Fe-Na-Cl scattering path distance is also different, and shows a value higher than the one expected from the XRD analysis.

The discrepancies in the bond distances between those observed from XAFS and calculated from XRD analysis are a clear indication that the local crystal structure within the unit cell of $Cs_2NaFeCl_6$ is distorted. Fig-

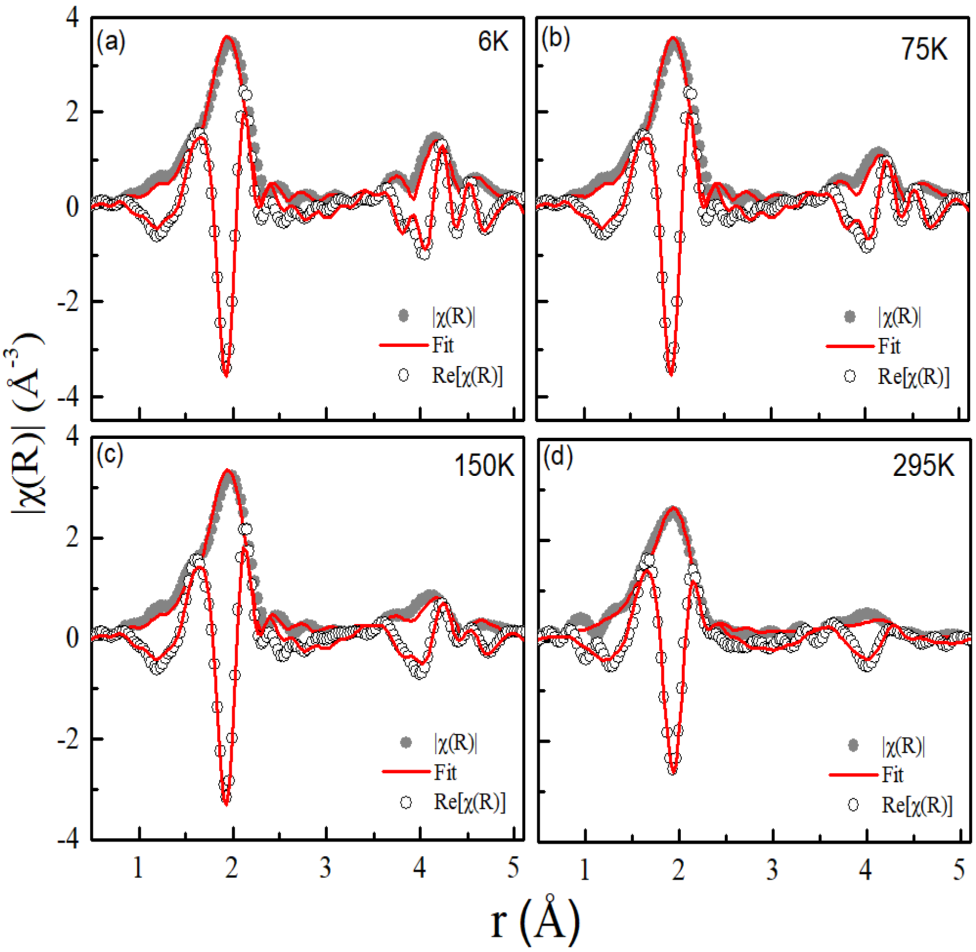

Figure 5.9: Magnitude and real component of Fourier transformed Fe-K edge EXAFS spectra with fitting at (a) 6 K, (b) 75 K, (c) 150 K and (d) 295 K.

ure 5.10 shows a schematic for a feasible distortion of the octahedra while maintaining the overall perovskite structure. The Fe-Cl-Na bond angle is ideally 180° and the total Fe-Cl-Na bond distance equates half the value of lattice constant ($a/2$). A shorter than the expected Fe-Cl distance, at the same time, as expected Fe-Na distance can be accommodated within the perovskite structure only if the Fe-Cl-Na bond angle deviates from 180°, giving rise to a buckling of Cl ions. In other words, the $[FeCl_6]^{3-}$ octahedra tilt to accommodate the quite rigid and ionic nature of its adjacent $[NaCl_6]^{5-}$ octahedra. The implication of such a local structural distortion around Fe atoms is also seen on its near-edge absorption spectrum. As presented in Figure 5.8(b), the leading edge of the Fe-K edge absorption

| Temperature | Distance | C.N. | R (Å) | $\sigma^2$ (Å$^2$) |
|---|---|---|---|---|
| 6K | Fe-Cl | 6 | 2.369 ± 0.004 | 0.00314 ± 0.0006 |
| | Fe-Cs | 8 | 4.439 ± 0.009 | 0.00417 ± 0.0010 |
| | Fe-Na | 6 | 5.135 ± 0.123 | 0.01401 ± 0.0230 |
| | Fe-(Na-Cl) | 12 | 5.185 ± 0.024 | 0.01136 ± 0.0040 |
| 75K | Fe-Cl | 6 | 2.371 ± 0.004 | 0.00319 ± 0.0005 |
| | Fe-Cs | 8 | 4.438 ± 0.013 | 0.00602 ± 0.0013 |
| | Fe-Na | 6 | 5.145 ± 0.116 | 0.01294 ± 0.0206 |
| | Fe-(Na-Cl) | 12 | 5.195 ± 0.025 | 0.01240 ± 0.0046 |
| 150K | Fe-Cl | 6 | 2.372 ± 0.005 | 0.00389 ± 0.0006 |
| | Fe-Cs | 8 | 4.451 ± 0.020 | 0.00889 ± 0.0024 |
| | Fe-Na | 6 | 5.151 ± 0.106 | 0.01227 ± 0.0186 |
| | Fe-(Na-Cl) | 12 | 5.205 ± 0.028 | 0.01488 ± 0.0054 |
| 295K | Fe-Cl | 6 | 2.381 ± 0.005 | 0.00638 ± 0.0008 |
| | Fe-Cs | 8 | 4.477 ± 0.024 | 0.01620 ± 0.0062 |
| | Fe-Na | 6 | 5.189 ± 0.086 | 0.01154 ± 0.0149 |
| | Fe-(Na-Cl) | 12 | 5.260 ± 0.118 | 0.02680 ± 0.0089 |

Table 5.3: Atomic distances, co-ordination number (C.N.) and thermal mean square variation extracted from EXAFS spectra of $Cs_2NaFeCl_6$ compound at different temperatures.

shows a systematic shift towards lower energy with increasing temperature. Such a shift in the negative direction implies that the valence state of Fe ions changes from the ideal $Fe^{+3}$ to a $Fe^{(+3)-\delta}$ value, as the temperature is increased. In other words, a localization of charge takes place on the Fe ions. This localization of charge on Fe atom increases its effective mass, which alternately decreases the atomic vibrational frequency (since, $\omega \propto \frac{1}{\sqrt{m}}$) as observed in the red shifting of $[FeCl_6]^{3-}$ octahedral Raman mode ($E_g$ mode).

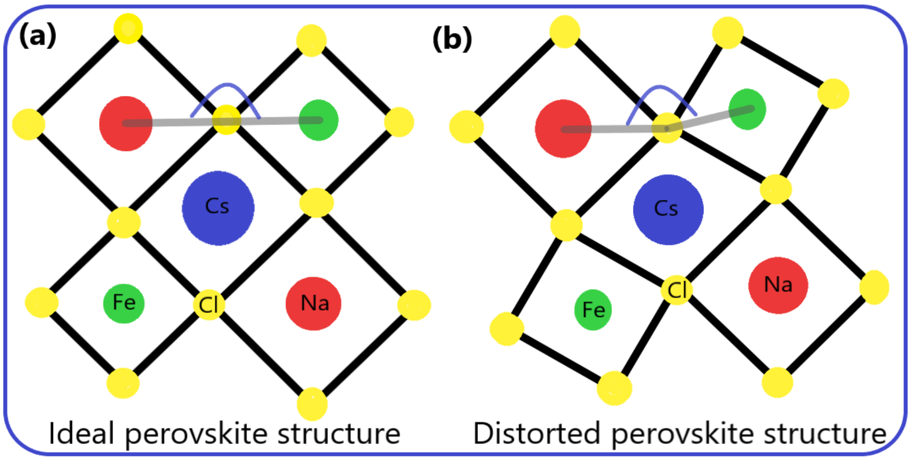

Figure 5.10: Schematic shows the in-plane view of the crystal structure of (a) an ideal perovskite and (b) distorted perovskite exhibiting octahedral distortion.

## 5.7 Temperature dependent band gap study

The change in the crystal potential, brought about by the local lattice distortion and the associated charge renormalization on Fe cations reflects in its optical properties. We now examine the temperature induced optical band gap ($E_g$) variation of $Cs_2NaFeCl_6$ starting from 150 K to 450 K. Here, we record the diffuse reflectance spectra (R) of $Cs_2NaFeCl_6$ at various temperatures of interest, and extract the absorption coefficient (F(R)) from R, using the Kubelka-Munk function, $F(R) = \frac{(1-R)^2}{2R}$. The reflectance spectra so obtained are shown in Figure 5.11(a). These spectra are continuous with no sign of any structural anomaly, and no extra features that could be associated with exciton or in-gap states. Using the Tauc plot, where $[F(R)h\nu]^2$ is plotted against the incident photon energy, $h\nu$, the band gap value is extracted by extrapolating the absorption edge to intercept the energy axis, as shown in the inset of Figure 5.11(a). Similar to any conventional semiconductor, $E_g$ of $Cs_2NaFeCl_6$ decreases systematically with rising temperature, as can be seen from Figure 5.11(b).

Further, we analyse the band edges at each temperature, in terms of Urbach energy ($E_u$). The optical absorption spectrum consists of an exponential tail near the fundamental absorption edge, also known as Urbach tail [71, 72], that often results as the combination of thermal disorder arising from the excitation of phonon modes and static disorder emerging from intrinsic structural imperfections [107]. Using the empirical equation, $\alpha = \alpha_0 exp(\frac{h\nu - E_g}{E_u})$, where $\alpha$ is the absorption coefficient and $\alpha_0$ is a constant, we extract the Urbach energy from the present optical spectroscopy plots. The value of $E_u$ extracted at different temperatures is plotted in Figure 5.11(b). The fact that sizable Urbach energy is observed at a given temperature, indicates the influence of electron-phonon coupling on the optical properties of $Cs_2NaFeCl_6$, explicitly driven by the local lattice deformation.

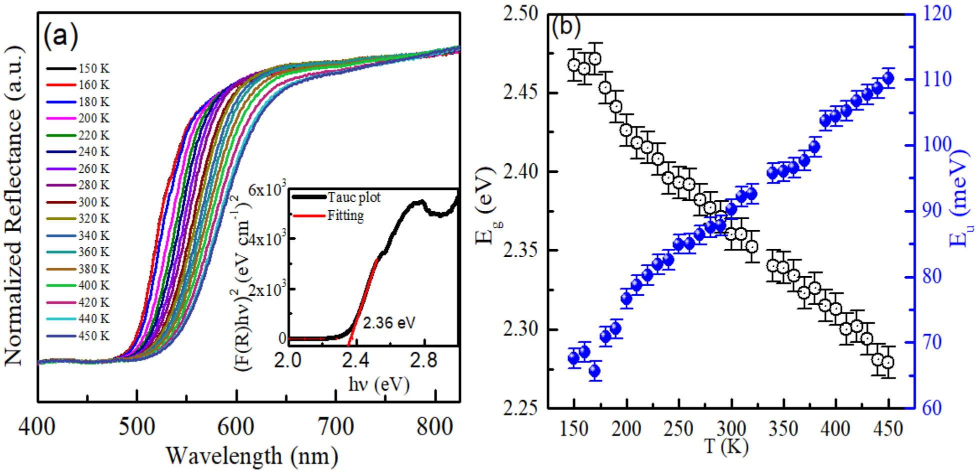

Figure 5.11: (a) Temperature dependent diffuse reflectance spectra of $Cs_2NaFeCl_6$ compound (The inset shows the Tauc plot of the compound at 300 K) and (b) variation of band gap and Urbach energy with temperature.

## 5.8 Summary

Various optoelectronic properties exhibited by halide double perovskites ($A_2B'B''X_6$) are highly influenced by the B"-site cations. Further, occupation of B"-site with ions of smaller radii enhances the structural stability of perovskites by shortening the bond length between halide and metal cation. The impact of B"-site cation has been proved vital for tailoring the thermal and electronic properties of halide perovskites. In $Cs_2NaFeCl_6$, the excellent thermochromic property is highly dependent on the bonding environment of Fe atoms. The octahedral distortion of $[FeCl_6]^{3-}$ not only affect the local lattice picture, but also modulates the electronic environment resulting in electron-phonon interaction. Both the optical band gap variation and strong electron-phonon coupling with temperature are responsible for the amazing colour change of $Cs_2NaFeCl_6$ crystals. Further, we have explicitly shown the charge localization on Fe atom causing octahedral distortion utilizing temperature dependent XRD, Raman and XAFS analysis. Moreover, our findings emphasize the significant potential for harnessing thermochromism in lead free halide perovskites.

.

# Chapter 6

# Conclusions and Future perspective

This chapter presents a concise overview of the thesis, which is primarily aimed at unraveling the structure-property correlation in halide double perovskites. The core focus is to delve into the underlying mechanisms that govern their unique photophysical behavior. Here, we will first emphasize the innovative findings and key discoveries made during this research, shedding new light on these materials. This will be followed by a brief description on potential future research avenues, highlighting areas where further investigation could lead to significant advancements in understanding and applications.

## 6.1 Conclusions

The major findings are summarized as follows:

We have successfully synthesized the phase pure HDPs using a facile solution based synthesis method and prepared compositions are:

1. $Cs_2Na_xAg_{1-x}BiCl_6$ (0<x<1)
2. $Cs_2AgBi_{0.9}M_{0.1}Cl_6$ and $Cs_2AgIn_{0.9}M_{0.1}Cl_6$ (M = Cr, Mn and Yb)
3. $Cs_2NaFeCl_6$

While the end-members of $Cs_2Na_xAg_{1-x}BiCl_6$ series do not show any photoluminescence property, the Na substituted mixed compositions exhibit enhanced PL. In our study, we show that the enhanced PL is due to the presence of self-trapped exciton states and the formation and stabilization of these trapped states are highly influenced by the strong electron-phonon coupling.

The enhancement in PL is also seen with the substitution of transition metal (Cr, Mn) and rare earth element (Yb) in $Cs_2AgBiCl_6$ and $Cs_2AgInCl_6$, however, their electrical properties are not well understood. In this study, we carry out a thorough investigation on their charge transport properties to show the enhancement in conductivity of these HDPs. Further, the photo-conductivity of these compounds show a superlinear power dependent behaviour due to the photo-thermionic effect.

We have synthesized the single crystals of $Cs_2NaFeCl_6$ that display reversible thermochromism in this HDP, over a wide range of temperatures. The octahedral distortion of Fe atom in $Cs_2NaFeCl_6$ modulates the electronic environment resulting in electron-phonon interaction. Both the optical band gap variation and strong electron-phonon coupling with temperature are responsible for the amazing colour change of these crystals.

## 6.2 Future Aspects

The $Cs_2Na_xAg_{1-x}BiCl_6$, and (Cr, Mn and Yb) substituted $Cs_2AgBiCl_6$ and $Cs_2AgInCl_6$ show good photoluminescence property and enhanced photoconductivity, which gives an opportunity to use these compounds in photovoltaic applications. The optical properties of these materials should be investigated in NIR region to check for the application like NIR photodetector and imaging. To enable this, attempt should be taken for device fabrication by deposition of thin film. Further, the testing, repeatability, durability, efficiency and optimization of the devices need to be verified for commercialization of these HDPs.

The single crystal of $Cs_2NaFeCl_6$ shows reversible thermochromism. It is necessary to study how these single crystals can be used in temperature sensors and display devices. Keeping in line with the demands of the commercial market, the thin film of this perovskite should be synthesized and optimization of the device is needed for better efficiency, durability and cost-effectiveness.

Moreover, the high structural stability and concealed physical properties of halide double perovskites continue to drive researchers toward deeper investigations of their fascinating optoelectronic behavior. The quest to unlock these hidden attributes not only motivates the study of their current properties but also paves the way for discovering novel perovskites through suitable compositional mapping. This approach will provide a comprehensive understanding of the processes governing the behavior of excited states and charge carriers in various perovskites, enabling advancements in the design and optimization of next-generation optoelectronic devices.

# Bibliography

[1] Poortmans J., and Arkhipov V., Thin Film Solar Cells, Fabrication, Characterization and Applications, Advanced Amorphous Silicon Solar Cell Technologies, 2006, **471**;

[2] O'Regan B., and Grätzel M., A low-cost, high-efficiency solar cell based on dye-sensitized colloidal $TiO_2$ films, Nature, 1991, **353** (6346), 737-740;

[3] Yang W. S., Park B. W., Jung E. H., Jeon N. J., Kim Young C., Lee D., Shin S. S., Seo J., Kim E. K., Noh J. H., and Seok S., Iodide management in formamidinium-lead-halide–based perovskite layers for efficient solar cells, Science, 2017, **356** (6345), 1376-1379;

[4] Suntivich J., Gasteiger H. A., Yabuuchi N., Nakanishi H., Goodenough J. B. and Shao-Horn Y., Design principles for oxygen-reduction activity on perovskite oxide catalysts for fuel cells and metal–air batteries, Nat. Chem., 2011, **3** (7), 546-550;

[5] Cohen R. E., Origin of ferroelectricity in perovskite oxides, Nature, 1992, **358** (6382), 136-138;

[6] Guo Y., Kakimoto K., and Ohsato H., Phase transitional behavior and piezoelectric properties of $(Na_{0.5}K_{0.5})NbO_3$–$LiNbO_3$ ceramics, Appl. Phys. Lett., 2004, **85** (18), 4121-4123;

[7] Béa H., Gajek M., Bibes M., and Barthélémy A., Spintronics with multiferroics, J. Phys. Condens. Matter., 2008, **43** (20), 434221;

[8] Saparov B., and Mitzi D. B., Organic–Inorganic Perovskites: Structural Versatility for Functional Materials Design, Chem. Rev., 2016, **116** (7), 4558-4596;

[9] Li C., Lu X., Ding W., Feng L., Gao Y., and Guo Z., Formability of $ABX_3$ (X = F, Cl, Br, I) halide perovskites, Acta Crystallographica Section B, 2008, **64** (6), 702-707;

[10] Kojima A., Teshima K., Shirai Y., and Miyasaka T., Organometal Halide Perovskites as Visible-Light Sensitizers for Photovoltaic Cells, J. Am. Chem. Soc., 2009, **131** (17), 6050-6051;

[11] NREL (2024), https://www.nrel.gov/pv/cell-efficiency.html;

[12] Zhang F., Yang B., Li Y., Deng W., and He R., Extra long electron–hole diffusion lengths in $CH_3NH_3PbI_{3-x}Cl_x$ perovskite single crystals, J. Mater. Chem. C, 2017, **5** (33), 8431-8435;

[13] De Roo J., Ibáñez M., Geiregat P., Nedelcu G., Maes J., Kovalenko M. V., and Hens Z., Highly Dynamic Ligand Binding and Light Absorption Coefficient of Cesium Lead Bromide Perovskite Nanocrystals, ACS Nano, 2016, **10** (2), 2071-2081;

[14] Braly I. L., deQuilettes D. W., Pazos-Outón L. M., Burke S., Ziffer M. E., Ginger D. S., and Hillhouse H. W., Hybrid perovskite films approaching the radiative limit with over 90% photoluminescence quantum efficiency, Nat. Photonics, 2018, **12** (6), 355-361;

[15] Panda D. P., Swain D., Chaudhary M., Mishra S., Bhutani G., De A. K., Waghmare U. V., and Sundaresan A., Electron–Phonon Coupling Mediated Self-Trapped-Exciton Emission and Internal Quantum Confinement in Highly Luminescent Zero-Dimensional $(\text{Guanidinium})_6Mn_3X_{12}$ (X = Cl and Br), Inorg. Chem., 2022, **61** (43), 17026-17036;

[16] Ganesan R., Vinodhini S. P., Balasubramani V., Parthipan G., Sridhar T. M., Arulmozhi R., and Muralidharan R., Tuning the band gap

of hybrid lead free defect perovskite nano crystals for solar cell applications, New J. Chem., 2019, **43** (38), 15258-15266;

[17] Jodlowski A. D., Roldán-Carmona C., Grancini G., Salado M., Ralaiarisoa M., Ahmad S., Koch N., Camacho L., de Miguel G., and Nazeeruddin M. K., Large guanidinium cation mixed with methylammonium in lead iodide perovskites for 19% efficient solar cells, Nat. Energy, 2017, **2** (12), 972-979;

[18] Kalita D., Nandi P., Sahu P., Schoekel A., van Embden J., Topwal D., and Manju U., Dynamic Structural Evolution and Dual Emission Behavior in Hybrid Organic Lead Bromide Perovskites, J. Phys. Chem. Lett., 2024, **15** (9), 2557-2565;

[19] Fang Y., Dong Q., Shao Y., Yuan Y., and Huang J., Highly narrowband perovskite single-crystal photodetectors enabled by surface-charge recombination, Nat. Photonics, 2015, **9** (10), 679-686;

[20] Lei L., Dong Q., Gundogdu K., and So F., Metal Halide Perovskites for Laser Applications, Adv. Funct. Mater., 2021, **31** (16), 2010144;

[21] He Y., and Galli G., Perovskites for Solar Thermoelectric Applications: A First Principle Study of $CH_3NH_3AI_3$ (A = Pb and Sn), Chem. Mater., 2014, **26** (18), 5394-5400;

[22] Boyd C. C., Cheacharoen R., Leijtens T., and McGehee M. D., Understanding Degradation Mechanisms and Improving Stability of Perovskite Photovoltaics, Chem. Rev., 2019, **119** (5), 3418-3451;

[23] Rong Y., Liu L., Mei A., Li X., and Han H., Beyond Efficiency: the Challenge of Stability in Mesoscopic Perovskite Solar Cells, Adv. Energy Mater., 2015, **5** (20), 1501066;

[24] Wang K. L., Wang R., Wang Z. K., Li M., Zhang Y., Ma H., Liao L., and Yang Y., Tailored Phase Transformation of $CsPbI_2Br$ Films by Copper(II) Bromide for High-Performance All-Inorganic Perovskite Solar Cells, Nano Lett., 2019, **19** (8), 5176-5184;

[25] Schileo G., and Grancini G., Lead or no lead? Availability, toxicity, sustainability and environmental impact of lead-free perovskite solar cells, J. Mater. Chem. C, 2021, **9** (1), 67-76;

[26] Krishnamoorthy T., Ding H., Yan C., Leong W. L., Baikie T., Zhang Z., Sherburne M., Li S., Asta M., Mathews N., and Mhaisalkar S. G., Lead-free germanium iodide perovskite materials for photovoltaic applications, J. Mater. Chem. A, 2015, **3** (47), 23829-23832;

[27] Song T. B., Yokoyama T., Stoumpos C. C., Logsdon J., Cao D. H., Wasielewski M. R., Aramaki S., and Kanatzidis M. G., Importance of Reducing Vapor Atmosphere in the Fabrication of Tin-Based Perovskite Solar Cells, J. Am. Chem. Soc., 2017, **139** (2), 836-842;

[28] Ju M. G., Chen M., Zhou Y., Garces H. F., Dai J., Ma L., Padture N. P., and Zeng X. C., Earth-Abundant Nontoxic Titanium(IV)-based Vacancy-Ordered Double Perovskite Halides with Tunable 1.0 to 1.8 eV Bandgaps for Photovoltaic Applications, ACS Energy Lett., 2018, **3** (2), 297-304;

[29] Park B. W., Philippe B., Zhang X., Rensmo H., Boschloo G., and Johansson E. M. J., Bismuth Based Hybrid Perovskites $A_3Bi_2I_9$ (A: Methylammonium or Cesium) for Solar Cell Application, Adv. Mater., 2015, **27** (43), 6806-6813;

[30] Ning W., and Gao F., Structural and Functional Diversity in Lead-Free Halide Perovskite Materials, Adv. Mater., 2019, **31** (22), 1900326;

[31] Cross C. W., and Hillebrand W. F., On minerals of the cryolite group recently found in Colorado, Am. J. Sci., 1883, **26** (154), 271-294;

[32] Wolf N. R., Connor B. A., Slavney A. H., and Karunadasa H. I., Doubling the Stakes: The Promise of Halide Double Perovskites, Angew. Chem. Int. Ed., 2021, **60** (30), 16264-16278;

[33] Giustino F., and Snaith H. J., Toward Lead-Free Perovskite Solar Cells, ACS Energy Lett., 2016, **1** (6), 1233-1240;

[34] McClure E. T., Ball M. R., Windl W., and Woodward P. M., $Cs_2AgBiX_6$ (X = Br, Cl): New Visible Light Absorbing, Lead-Free Halide Perovskite Semiconductors, Chem. Mater., 2016, **28** (5), 1348-1354;

[35] Slavney A. H., Hu T., Lindenberg A. M., and Karunadasa H. I., A Bismuth-Halide Double Perovskite with Long Carrier Recombination Lifetime for Photovoltaic Applications, J. Am. Chem. Soc., 2016, **138** (7), 2138-2141;

[36] Volonakis G., Haghighirad A., Milot R. L., Sio W. H., Filip M. R., Wenger B., Johnston M. B., Herz L. M., Snaith H. J., and Giustino F., $Cs_2InAgCl_6$: A New Lead-Free Halide Double Perovskite with Direct Band Gap, J. Phys. Chem. Lett., 2017, **8** (4), 772-778;

[37] Tran T. T., Panella J. R., Chamorro J. R., Morey J. R., and McQueen T. M., Designing indirect–direct bandgap transitions in double perovskites, Mater. Horiz., 2017, **4** (4), 688-693;

[38] Hu H., Homewood K., and Gao Y., Er-doped $Cs_2AgBiCl_6$ double perovskite large single crystal for optoelectronics, Opt. Mater., 2014, **151**, 115327;

[39] Ning W., Zhao X. G., Klarbring J., Bai S., Ji F., Wang F., Simak S. I., Tao Y., Ren X. M., Zhang L., Huang W., Abrikosov I. A., and Gao F., Thermochromic Lead-Free Halide Double Perovskites, Adv. Funct. Mater., 2019, **29** (10), 1807375;

[40] Wu C., Zhang Q., Liu Y., Luo W., Guo X., Huang Z., Ting H., Sun W., Zhong X., Wei S., Wang S., Chen Z., and Xiao L., The Dawn of Lead-Free Perovskite Solar Cell: Highly Stable Double Perovskite $Cs_2AgBiBr_6$ Film, Adv. Sci., 2018, **5** (3), 1700759;

[41] Arfin H., Rathod R., Shingote A. S., Priolkar K. R., Santra P. K., and Nag A., Short-Wave Infrared Emissions from $Te^{4+}$–$Ln^{3+}$ (Ln: Er, Yb)-Codoped $Cs_2NaInCl_6$ Double Perovskites, Chem. Mater., 2023, **35** (17), 7133-7143;

[42] Luo J., Li S., Wu H., Zhou Y., Li Y., Liu J., Li J., Li K., Yi F., Niu G., and Tang J., $Cs_2AgInCl_6$ Double Perovskite Single Crystals: Parity Forbidden Transitions and Their Application For Sensitive and Fast UV Photodetectors, ACS Photonics, 2018, **5** (2), 398-405;

[43] Pan W., Wu H., Luo J., Deng Z., Ge C., Chen C., Jiang X., Yin W. J., Niu G., Zhu L., Yin L., Zhou Y., Xie Q., Ke X., Sui M., and Tang J., $Cs_2AgBiBr_6$ single-crystal X-ray detectors with a low detection limit, Nat. Photonics, 2017, **11** (11), 726-732;

[44] Xin-Gang Z., Dongwen Y., Ji-Chang R., Yuanhui S., Zewen X., and Lijun Z., Rational Design of Halide Double Perovskites for Optoelectronic Applications, Joule, 2018, **2** (9), 1662-1673;

[45] Wang B., Li N., Yang L., Dall'Agnese C., Jena A. K., Sasaki S., Miyasaka T., Tamiaki H., and Wang X., Chlorophyll Derivative-Sensitized $TiO_2$ Electron Transport Layer for Record Efficiency of $Cs_2AgBiBr_6$ Double Perovskite Solar Cells, J. Am. Chem. Soc., 2021, **143** (5), 2207-2211;

[46] Aull Brian F., and Jenssen Hans P., Impact of ion-host interactions on the 5d-to-4f spectra of lanthanide rare-earth-metal ions. II. The Ce-doped elpasolites, Phys. Rev. B, 1986, **34** (10), 6647-6655;

[47] Da Fonseca R. J. M., Sosman L. P., Tavares A. Dias, and Bordallo H. N., Vibrational Analysis of the Elpasolites $Cs_2NaAlF_6$ and $Cs_2NaGaF_6$ Doped with $Cr^{3+}$ Ions by Fluorescence Spectroscopy, Journal of Fluorescence, 2000, **10** (4), 375-381;

[48] Creutz S. E., Crites E. N., De Siena M. C., and Gamelin D. R., Colloidal Nanocrystals of Lead-Free Double-Perovskite (Elpasolite) Semiconductors: Synthesis and Anion Exchange To Access New Materials, Nano Lett., 2018, **18** (2), 1118-1123;

[49] Xiao Z., Song Z., and Yan Y., From Lead Halide Perovskites to Lead-Free Metal Halide Perovskites and Perovskite Derivatives, Adv. Mater., 2019, **31** (47), 1803792;

[50] Hoye R. L. Z., Eyre L., Wei F., Brivio F., Sadhanala A., Sun S., Li W., Zhang K. H. L., MacManus-Driscoll J. L., Bristowe P. D., Friend R. H., Cheetham A. K., and Deschler F., Fundamental Carrier Lifetime Exceeding 1 $\mu$s in $Cs_2AgBiBr_6$ Double Perovskite, Adv. Mat. Inter., 2018, **5** (15), 1800464;

[51] Majher J. D., Gray M. B., Strom T. A., and Woodward P. M., $Cs_2NaBiCl_6$:$Mn^{2+}$—A New Orange-Red Halide Double Perovskite Phosphor, Chem. Mater., 2019, **31** (5), 1738-1744;

[52] Wei F., Deng Z., Sun S., Hartono N. T. P., Seng H. L., Buonassisi T., Bristowe P. D., and Cheetham A. K., Enhanced visible light absorption for lead-free double perovskite $Cs_2AgSbBr_6$, Chem. Commun., 2019, **55** (26), 3721-3724;

[53] Li Z., Kavanagh S. R., Napari M., Palgrave R. G., Abdi-Jalebi M., Andaji-Garmaroudi Z., Davies D. W., Laitinen M., Julin J., Isaacs M. A., Friend R. H., Scanlon D. O., Walsh A., and Hoye R. L. Z., Bandgap lowering in mixed alloys of $Cs_2Ag(Sb_xBi_{1-x})Br_6$ double perovskite thin films, J. Mater. Chem. A, 2020, **8** (41), 21780-21788;

[54] Zhou J., Rong X., Molokeev M. S., Zhang X., and Xia Z., Exploring the transposition effects on the electronic and optical properties of $Cs_2AgSbCl_6$ via a combined computational-experimental approach, J. Mater. Chem. A, 2018, **6** (5), 2346-2352;

[55] Meng W., Wang X., Xiao Z., Wang J., Mitzi D. B., and Yan Y., Parity-Forbidden Transitions and Their Impact on the Optical Absorption Properties of Lead-Free Metal Halide Perovskites and Double Perovskites, J. Phys. Chem. Lett., 2017, **8** (13), 2999-3007;

[56] Locardi F., Cirignano M., Baranov D., Dang Z., Prato M., Drago F., Ferretti M., Pinchetti V., Fanciulli M., Brovelli S., De Trizio L., and Manna L., Colloidal Synthesis of Double Perovskite $Cs_2AgInCl_6$ and Mn-Doped $Cs_2AgInCl_6$ Nanocrystals, J. Am. Chem. Soc., 2018, **140** (40), 12989-12995;

[57] Li S., Luo J., Liu J., and Tang J., Self-Trapped Excitons in AllInorganic Halide Perovskites: Fundamentals, Status, and Potential Applications., J. Phys. Chem. Lett., 2019, **10** (8), 1999-2007;

[58] Ji F., Wang F., Kobera L., Abbrent S., Brus J., Ning W., and Gao F., The atomic-level structure of bandgap engineered double perovskite alloys $Cs_2AgIn_{1-x}Fe_xCl_6$, Chem. Sci., 2021, **12** (5), 1730-1735;

[59] Yin H., Xian Y., Zhang Y., Chen W., Wen X., Rahman N. U., Long Y., Jia B., Fan J., and Li W., An Emerging Lead-Free Double-Perovskite $Cs_2AgFeCl_6$:In Single Crystal, Adv. Funct. Mater., 2020, **30** (43), 2002225;

[60] Rodríguez-Carvajal J., Recent advances in magnetic structure determination by neutron powder diffraction, Phys. B: Condens. Matter, 1993, **192** (1), 55-69;

[61] Conradson S. D., XAFS: A Technique to Probe Local Structure, Los Alamos Sci., 2000, **422**, 422-435;

[62] Ravel B., and Newville M., *ATHENA*, *ARTEMIS*, *HEPHAESTUS*: data analysis for X-ray absorption spectroscopy using *IFEFFIT*, Journal of Synchrotron Radiation, 2005, **12** (4), 537-541;

[63] Biskup T., Structure–Function Relationship of Organic Semiconductors: Detailed Insights From Time-Resolved EPR Spectroscopy, Front. Chem., 2019, **7**;

[64] Sahoo B. R., Devan R. S., and Bhobe P. A., Viability of $Cs_2AgBiCl_6$: $Cr^{3+}/Yb^{3+}$ and $Cs_2AgInCl_6$: $Cr^{3+}/Yb^{3+}$ as Efficient Photoluminescent Materials and Other Photophysical Applications, ACS Appl. Opt. Mater., 2024, **2** (4), 617-623;

[65] Zhou L., Xu Y., Chen B., Kuang D., and Su C., Synthesis and Photocatalytic Application of Stable Lead-Free $Cs_2AgBiBr_6$ Perovskite Nanocrystals, Small, 2018, **14** (11), 1703762;

[66] Kubicki D. J., Saski M., MacPherson S., Galkowski K., Lewinski J., Prochowicz D., Titman J. J., and Stranks S. D., Halide Mixing and Phase Segregation in $Cs_2AgBiX_6$ (X = Cl, Br, and I) Double Perovskites from Cesium-133 Solid-State NMR and Optical Spectroscopy, Chem. Mater., 2020, **32** (19), 8129-8138;

[67] Manna D., Kangsabanik J., Das T. K., Das D., Alam A., and Yella A., Lattice Dynamics and Electron–Phonon Coupling in Lead-Free $Cs_2AgIn_{1-x}Bi_xCl_6$ Double Perovskite Nanocrystals, J. Phys. Chem. Lett., 2020, **11** (6), 2113-2120;

[68] Han D., Ogura M., Held A., and Ebert H., Unique Behavior of Halide Double Perovskites with Mixed Halogens, ACS Appl. Mater. Interfaces, 2020, **12** (33), 37100-37107;

[69] Péan E. V., Dimitrov S., De Castro C. S., and Davies M. L., Interpreting time-resolved photoluminescence of perovskite materials, Phys. Chem. Chem. Phys., 2020, **22** (48), 28345-28358;

[70] Huso J., Che H., Thapa D., Canul A., McCluskey M. D., and Bergman L., Phonon dynamics and Urbach energy studies of MgZnO alloys, J. Appl. Phys., 2015, **117** (12), 125702;

[71] Greeff C. W., and Glyde H. R., Anomalous Urbach tail in GaAs, Phys. Rev. B, 1995, **51** (3), 1778-1783;

[72] Urbach F., The Long-Wavelength Edge of Photographic Sensitivity and of the Electronic Absorption of Solids, Phys. Rev., 1953, **92** (5), 1324;

[73] Zeiske S., Sandberg O. J., Zarrabi N., Wolff C. M., Raoufi M., Peña-Camargo F., Gutierrez-Partida E., Meredith P., Stolterfoht M., and Armin A., Static Disorder in Lead Halide Perovskites, J. Phys. Chem. Lett., 2022, **13** (31), 7280-7285;

[74] Yadav V., and Mohanty T., Tuning the electron–phonon interaction via exploring the interrelation between Urbach energy and fano-type

asymmetric raman line shape in GO-hBN nanocomposites, Nanotechnology, 2023, **34** (49), 495204;

[75] Fano U., Effects of Configuration Interaction on Intensities and Phase Shifts, Phys. Rev., 1961, **124** (6), 1866-1878;

[76] Hasdeo E. H., Nugraha A. R. T., Dresselhaus M. S., and Saito R., Breit-Wigner-Fano line shapes in Raman spectra of graphene, Phys. Rev. B, 2014, **90** (24), 245140;

[77] Zhang L., Fang Y., Sui L., Yan J., Wang K., Yuan K., Mao W. L., and Zou B., Tuning Emission and Electron–Phonon Coupling in Lead-Free Halide Double Perovskite $Cs_2AgBiCl_6$ under Pressure, ACS Energy Lett., 2019, **4** (12), 2975-2982;

[78] Saitoh A., Komatsu T., and Karasawa T., Exciton–phonon interaction and conversion of excitons from free to self-trapped states in layered metal iodide crystals under hydrostatic pressure, J. Lumin., 2000, **87**, 633-635;

[79] Manna D., Das T. K., and Yella A., Tunable and Stable White Light Emission in $Bi^{3+}$-Alloyed $Cs_2AgInCl_6$ Double Perovskite Nanocrystals, Chem. Mater., 2019, **31** (24), 10063-10070;

[80] Liu Y., Jing Y., Zhao J., Liu Q., and Xia Z., Design Optimization of Lead-Free Perovskite $Cs_2AgInCl_6$:Bi Nanocrystals with 11.4% Photoluminescence Quantum Yield, Chem. Mater., 2019, **31** (9), 3333-3339;

[81] Rao Z., Li Q., Li Z., Zhou L., Zhao X., and Gong X., Ultra-High-Sensitive Temperature Sensing Based on $Er^{3+}$ and $Yb^{3+}$ Co-Doped Lead-Free Double Perovskite Microcrystals, J. Phys. Chem. Lett., 2022, **13** (16), 3623-3630;

[82] Jeevaraj M., Sivaganesh D., Saravanakumar S., Asath B. S., Sudhahar S., and Krishna K. M., Broadband near infrared emission in $Cr^{3+}$: $Cs_2AgBiCl_6$ double perovskite halides, Opt. Mater., 2023, **143**, 114294;

[83] Jeevaraj M., Sudhahar S., Nallamuthu N., Devendran P., Saravanakumar S., Sivaganesh D., and Kumar M. Krishna, Solution processed $Mn^{2+}$ doped $Cs_2AgInCl_6$ lead free double perovskite as a potential light emitting material, Phys. B: Condens. Matter., 2023, **653**, 414679;

[84] Zhao F., Song Z., Zhao J., and Liu Q., Double perovskite $Cs_2AgInCl_6$:$Cr^{3+}$: broadband and near-infrared luminescent materials, Inorg. Chem. Front., 2019, **6** (12), 3621-3628;

[85] Tanabe Y., and Sugano S., On the Absorption Spectra of Complex Ions II, J. Phys. Soc. Jpn., 1954, **9** (5), 766-779;

[86] Lidorenko N. S., Zil'bervarg V. E., and Nagaev E. L., Dielectric constants of solid eletrolytes and transition to superionic state, Sov Phys JETP, 1980, **51** (1), 89-93;

[87] Koops C.G., On the dispersion of resistivity and dielectric constant of some semiconductors at audiofrequencies, Phys. Rev., 1951, **83** (1), 121-124;

[88] Zheng X., Wang S., Wang J., Hua W., Zhang J., and Liu L., Long-Range and Short-Range Transport Dynamics of Li Ions in $LiMn_2O_4$, J. Phys. Chem. C, 2020, **124** (46), 25254-25261;

[89] Funke K., and Hoppe R., Jump-relaxation model yields Kohlrausch-Williams-Watts behaviour, Solid State Ion., 1990, **40**, 200-204;

[90] Stevels J. M., The Electrical Properties of Glass, Springer, 1957, **350**;

[91] Shen S., Wu T., Xue J., Li H., Chen Q., Cheng H., Wu L., and Qian J., A smart material built upon the photo-thermochromic effect and its use for managing indoor temperature, Chem. Commun., 2021, **57** (69), 8628-8631;

[92] De Bastiani M., Saidaminov M. I., Dursun I., Sinatra L., Peng W., Buttner U., Mohammed O. F., and Bakr O. M., Thermochromic Perovskite Inks for Reversible Smart Window Applications, Chem. Mater., 2017, **29** (8), 3367-3370;

[93] Lin J., Lai M., Dou L., Kley C. S., Chen H., Peng F., Sun J., Lu D., Hawks S. A., Xie C., Cui F., Alivisatos A. P., Limmer D. T., and Yang P., Thermochromic halide perovskite solar cells, Nat. Mater., 2018, **17** (3), 261-267;

[94] Zhang Y., Tso C. Y., Iñigo J. S., Liu S., Miyazaki H., Christopher Y. H. C., and Yu K. M., Perovskite thermochromic smart window: Advanced optical properties and low transition temperature, Appl. Energy, 2019, **254**, 113690;

[95] Singh A., and Satapathi S., Reversible Thermochromism in All-Inorganic Lead-Free $Cs_3Sb_2I_9$ Perovskite Single Crystals, Adv. Optical Mater., 2021, **9** (22), 2101062;

[96] Tailor N. K., Kruszyńska J., Prochowicz D., Yadav P., and Satapathi S., Thermochromism in Bismuth Halide Perovskites with Cation and Anion Transmutation, Adv. Opt. Mater., 2024, **12** (4), 2301583;

[97] Halder A., Choudhury D., Ghosh S., Subbiah A. S., and Sarkar S. K, Exploring Thermochromic Behavior of Hydrated Hybrid Perovskites in Solar Cells, J. Phys. Chem. Lett., 2015, **6** (16), 3180-3184;

[98] Fan H. Y., Temperature Dependence of the Energy Gap in Semiconductors, Phys. Rev., 1951, **82** (6), 900-905;

[99] Gopalan S., Lautenschlager P., and Cardona M., Temperature dependence of the shifts and broadenings of the critical points in GaAs, Phys. Rev. B, 1987, **35** (11), 5577-5584;

[100] Luo J., Wang X., Li S., Liu J., Guo Y., Niu G., Yao L., Fu Y., Gao L., Dong Q., Zhao C., Leng M., Ma F., Liang W., Wang L., Jin S., Han J., Zhang L., Etheridge J., Wang J., Yan Y., Sargent E. H., and Tang J., Efficient and stable emission of warm-white light from lead-free halide double perovskites, Nature, 2018, **563** (7732), 541-545;

[101] Yaffe O., Guo Y., Tan L. Z., Egger D. A., Hull T., Stoumpos C. C., Zheng F., Heinz T. F., Kronik L., Kanatzidis M. G., Owen J. S., Rappe

A. M., Pimenta M. A., and Brus L. E., Local Polar Fluctuations in Lead Halide Perovskite Crystals, Phys. Rev. Lett., 2017, **118** (13), 136001;

[102] Yamada Y., and Kanemitsu Y., Electron-phonon interactions in halide perovskites, NPG Asia Materials, 2022, **14** (1), 48;

[103] Yuan W., Niu G., Xian Y., Wu H., Wang H., Yin H., Liu P., Li W., and Fan J., In Situ Regulating the Order–Disorder Phase Transition in $Cs_2AgBiBr_6$ Single Crystal toward the Application in an X-Ray Detector, Adv. Funct. Mater., 2019, **29** (20), 1900234;

[104] Steele J. A., Puech P., Keshavarz M., Yang R., Banerjee S., Debroye E., Kim C. W., Yuan H., Heo N. H., Vanacken J., Walsh A., Hofkens J., and Roeffaers M. B. J., Giant Electron–Phonon Coupling and Deep Conduction Band Resonance in Metal Halide Double Perovskite, ACS Nano, 2018, **12** (8), 8081-8090;

[105] Zhang B., Klarbring J., Ji F., Simak S. I., Abrikosov I. A., Gao F., Rudko G. Y., Chen W. M., and Buyanova I. A., Lattice Dynamics and Electron–Phonon Coupling in Double Perovskite $Cs_2NaFeCl_6$, J. Phys. Chem. C, 2023, **127** (4), 1908-1916;

[106] Yang J., Zhang P., and Wei S. H., Band Structure Engineering of $Cs_2AgBiBr_6$ Perovskite through Order–Disordered Transition: A First-Principle Study, J. Phys. Chem. Lett., 2018, **9** (1), 31-35;

[107] Cody G. D., Tiedje T., Abeles B., Brooks B., and Goldstein Y., Disorder and the Optical-Absorption Edge of Hydrogenated Amorphous Silicon, Phys. Rev. Lett., 1981, **47** (20), 1480-1483;